



LAWRENCE
LIVERMORE
NATIONAL
LABORATORY

UCRL-TR-206885

Welding Stainless Steels and Refractory Metals Using Diode-Pumped Continuous Wave Nd:YAG Lasers

T. A. Palmer, J. W. Elmer, R. Pong, M. D. Gauthier

September 30, 2004

Disclaimer

This document was prepared as an account of work sponsored by an agency of the United States Government. Neither the United States Government nor the University of California nor any of their employees, makes any warranty, express or implied, or assumes any legal liability or responsibility for the accuracy, completeness, or usefulness of any information, apparatus, product, or process disclosed, or represents that its use would not infringe privately owned rights. Reference herein to any specific commercial product, process, or service by trade name, trademark, manufacturer, or otherwise, does not necessarily constitute or imply its endorsement, recommendation, or favoring by the United States Government or the University of California. The views and opinions of authors expressed herein do not necessarily state or reflect those of the United States Government or the University of California, and shall not be used for advertising or product endorsement purposes.

This work was performed under the auspices of the U.S. Department of Energy by University of California, Lawrence Livermore National Laboratory under Contract W-7405-Eng-48.

Table of Contents

Abstract	ii
Acknowledgement	iii
Introduction	1
Experimental	1
Results	8
Refractory Metals	8
Tantalum	8
Vanadium	11
Refractory Metal Welding Overview	24
Stainless Steels	25
304L Austenitic Stainless Steel	25
Power Variation Studies	25
Travel Speed Variation Studies	25
Effects of Energy Input per Unit Length of Weld	32
21-6-9 Austenitic Stainless Steel	37
Power Variation Studies	37
Travel Speed Variation Studies	44
Effects of Energy Input per Unit Length of Weld	44
304L Austenitic Stainless Steel vs. 21-6-9 Austenitic Stainless Steel	51
Comparison with Previous Studies	57
304L Stainless Steel	57
21-6-9 Austenitic Stainless Steel	62
Stainless Steel Welding Overview	70
General Findings and Concluding Remarks	72
References	74
Distribution	75

Welding Stainless Steels and Refractory Metals Using Diode-Pumped Continuous Wave Nd:YAG Lasers

T.A. Palmer, J.W. Elmer, R. Pong, and M.D. Gauthier

Lawrence Livermore National Laboratory
Livermore, CA 94550

Abstract

This report provides an overview of a series of developmental welding studies performed on a 2.2 kW Rofin Sinar DY-022 Diode Pumped Continuous Wave (CW) Nd:YAG welder at Lawrence Livermore National Laboratory (LLNL). Several materials systems, ranging from refractory metals, such as commercially pure tantalum and vanadium, to austenitic stainless steels, including both 304L and 21-6-9 grades, are examined. Power input and travel speed are systematically varied during the welding of each materials system, and the width, depth, and cross sectional area of the resulting weld fusion zones are measured. These individual studies are undertaken in order to characterize the response of the welder to changes in these welding parameters for a range of materials and to determine the maximum depth of penetration of which this welder is capable in each materials system. The maximum weld depths, which are on the order of 5.4 mm, are observed in the 21-6-9 austenitic stainless steel at the maximum laser power setting (2200 W) and a slow travel speed (6.4 mm/sec). The next highest weld depth is observed in the 304L stainless steel, followed by that observed in the vanadium and, finally, in the tantalum. Porosity, which is attributed to the collapse of the keyhole during welding, is also observed in the welds produced in tantalum, vanadium, and 304L stainless steel. Only the 21-6-9 austenitic stainless steel welds displayed little or no porosity over the range of welding parameters. Comparisons with similar laser welding systems are also made for several of these same materials systems. When compared with the welds produced by these other systems, the LLNL system typically produces welds of an equivalent or slightly higher depth.

Introduction

A Rofin Sinar DY-022 diode pumped Continuous Wave (CW) Nd:YAG laser welding system has recently been installed at Lawrence Livermore National Laboratory. This modern laser technology is being investigated as a replacement for technologies, including electron beam and pulsed Nd:YAG laser welding, currently in use within the Department of Energy (DOE) complex. This report details a series of initial tests performed on this welding system in an attempt to characterize its capabilities for a two classes of materials.

In order to initially characterize the capabilities of the laser, a series of autogenous laser welds are made on flat plate samples machined from two refractory metals and two grades of austenitic stainless steels. The parametric studies performed on these materials are designed to measure the response of the laser welder to changes in input power and travel speed and to determine the maximum weld depth of which this system is capable in these materials. Each weld is characterized by measuring the width, depth, and melted area in cross section samples removed from the middle of each weld. The results of this study will be used as a baseline for developing laser welding parameters and procedures for a range of applications using this and similar laser welding systems. A better understanding of the mechanisms leading to the formation of defects, in particular, those related to keyhole formation and stability in high power laser welds, will be pursued.

Experimental

A series of parametric studies have been performed on welds made on two classes of materials. The first class of materials is composed of commercially pure vanadium and tantalum, which are both refractory metals. An independent chemical analysis has been performed on the vanadium used to make the weld coupons. Based on this analysis, the vanadium samples contain only the following additional elements: 0.034 wt.% Si, 0.0052 wt.% C, 0.0004 wt.% H, 0.0170 wt.% N, and 0.0100 wt.% O. A similar chemical analysis is not available for the tantalum weld samples. The industry accepted chemical composition¹ for unalloyed tantalum is as follows, with all values being the maximum allowable: 0.010 wt.% C, 0.015 wt.% O, 0.010 wt.% N, 0.0015 wt.% H, 0.10 wt.% Nb, 0.010 wt.% Fe, 0.010 wt.% Ti, 0.050 wt.% W, 0.020 wt.% Mo, 0.005 wt.% Si, and 0.010 wt.% Ni.

In addition, welds are also made on two common grades of austenitic stainless steels, 304L and 21-6-9. Independent chemical analyses have also been performed on these materials, and the results for the 304L and 21-6-9 austenitic stainless steels are listed in Tables 1 and 2, respectively. The typical composition listed in each table details the industry accepted ranges for the different alloying elements in these austenitic stainless steels. On the other hand, a more tightly controlled composition, particularly with respect to the silicon, nitrogen, phosphorous, sulfur, and oxygen contents, is required for the 21-6-9 grade stainless steel for applications in which this laser will be typically used. This composition is detailed in the desired composition column in Table 2. All of the samples used in the LLNL studies for each stainless steel have been taken from the same heat. Therefore, there are no compositional differences between samples of the same grade of stainless steel to affect the results because all of the samples originate from the same heat of that material. On the other hand, the 304L and 21-6-9 stainless

¹ ASTM Standard B364-96 (2002), "Standard Specification for Tantalum and Tantalum Alloy Ingots"

steel weld samples used in the LANL studies are taken from different heats, as noted in the tables.

Table 1. Summary of chemical compositions in 304L stainless steel samples. All values are in wt.%.

	<u>LLNL and Rofin Sinar Weld Samples</u>	<u>LANL Weld Samples</u>	<u>Typical Composition²</u>
Fe	Balance	Balance	Balance
Cr	18.20	18.3	18.0-20.0
Ni	8.16	8.7	8.0-12.0
Mn	1.71	1.9	2.0 Max
Mo	0.47	0.256	----
Co	0.14	0.094	----
Cu	0.35	0.277	----
Si	0.44	0.478	0.75 Max
C	0.020	0.0218	0.03 Max
N	0.082	0.076	0.10 Max
P	0.03	0.020	0.045 Max
S	0.0004	----	0.030 Max

Table 2. Summary of alloying element compositions in 21-6-9 alloys used here. All values are in wt.%.

	<u>LLNL Weld Samples</u>	<u>LANL Weld Samples</u>	<u>Typical Composition³</u>	<u>Desired Composition⁴</u>
Carbon	0.02	0.0342	0.08 Max	0.02-0.04
Chromium	19.96	18.9	19.0-21.5	19.0-21.5
Nickel	7.02	7.4	5.5-7.5	5.5-7.5
Manganese	9.14	8.8	8.0-10.0	8.0-10.0
Silicon	0.05	0.47	1.0 Max	0.3-0.7
Nitrogen	0.23	0.26	0.15-0.40	0.20-0.30
Phosphorous	0.014	<0.01	0.06 Max	0.020 Max
Sulfur	<0.005	----	0.03 Max	0.02 Max
Oxygen	<0.001	<0.005	----	0.007 Max
Aluminum	0.04	0.014	----	----
Iron	Balance	Balance	Balance	Balance

The welds described in this report are made using a Rofin Sinar DY-022 diode pumped continuous wave Nd:YAG laser, located in the Laser Development Laboratory in B231, Rm 1623. The system has two major components: the welding power supply and the work station. Photographs of these two components are shown in Figures 1(a) and 1(b). All welding is done in

² ASTM Standard A240, "Standard Specification for Chromium and Chromium-Nickel Stainless Steel Plate, Sheet, and Strip for Pressure Vessels and for General Applications"

³ Alloy Digest, Filing Code SS-327, May 1976, Revised August 1990.

⁴ Electroslag Remelted WR Grade 21-6-9.

the work station, which holds the 3 axis computer numerical control (CNC) motion equipment and all of the fixed laser optics. The maximum power output of the laser power supply is 2200 W, which is delivered to the CNC Class 1 Laser Workstation using a 30 m long, 300 μm or 400 μm diameter fiber optic cable, which can be easily switched if desired. After the beam exits the fiber, it is collimated using a 160 mm diameter optic, passes through the optics assembly, and is focused onto the weld sample using a 160 mm diameter lens.



(a)



(b)

Figure 1(a&b). Photographs of (a) Rofin Sinar DY-022 power supply and control pendant and (b) CNC Class 1 Laser Workstation.

The welds made on the LLNL system are compared with ones produced under nominally the same welding conditions on comparable systems, located at Los Alamos National Laboratory (LANL) and the Rofin Sinar Development Labs in Detroit, MI. These systems are also diode pumped CW lasers manufactured by Rofin Sinar. A summary of the general characteristics of the three laser systems is given in Table 3. The major differences between these lasers are in the peak output power and the characteristics of the fixed optics. These differences are the most pronounced in the LLNL and LANL systems, with the result being different calculated beam sizes.

Table 3. Comparison of laser welding systems used in this study.

	<u>Model Number</u>	<u>Peak Output Power (W)</u>	<u>Fiber Diameter (μm)</u>	<u>Collimating Lens Focal Length (mm)</u>	<u>Final Focusing Lens Focal Length (mm)</u>	<u>Calculated Beam Size (μm)</u>
LLNL*	DY-022	2200	300	160	160	~300
Rofin-Sinar*	DY-044	4400	300	160	160	~300
LANL	DY-033	3300	400	120	160	~530

* Welds made on these two systems utilize the same optics.

The actual power output of the LLNL laser system at the exit of the optics assembly was measured using a water-cooled Coherent power meter over a range of machine power settings. Differences between the machine settings (beam power as it exits the power supply) and the

actual power reaching the part to be welded result from losses as the laser beam passes through the system optics. Figure 2 shows a comparison between the measured power levels exiting the laser optics over the range of machine settings with both a 300 μm and 400 μm diameter fiber optic delivery cable. In general, there is little difference in the laser power measurements from both fiber diameters and both display a loss in power ranging from approximately 20 to 25% of the machine setting. The relationships between the machine power settings and the measured power for the 300 μm and 400 μm fiber diameters, respectively, are given in the following relationships:

$$\text{Power (300}\mu\text{m)} = 0.7337 * \text{Machine Setting} + 24.67 \quad (1)$$

$$\text{Power (400}\mu\text{m)} = 0.7507 * \text{Machine Setting} + 22.87 \quad (2)$$

These relationships are similar, indicating that the choice of these fiber diameters does not have an undue impact on the laser losses in the LLNL system. These measured power levels are used throughout the remainder of the paper when discussing the power output of the LLNL laser. On the other hand, the machine power setting, even though it is not a completely accurate representation of the power impinging on the weld samples, is used when comparing the results from the various systems.

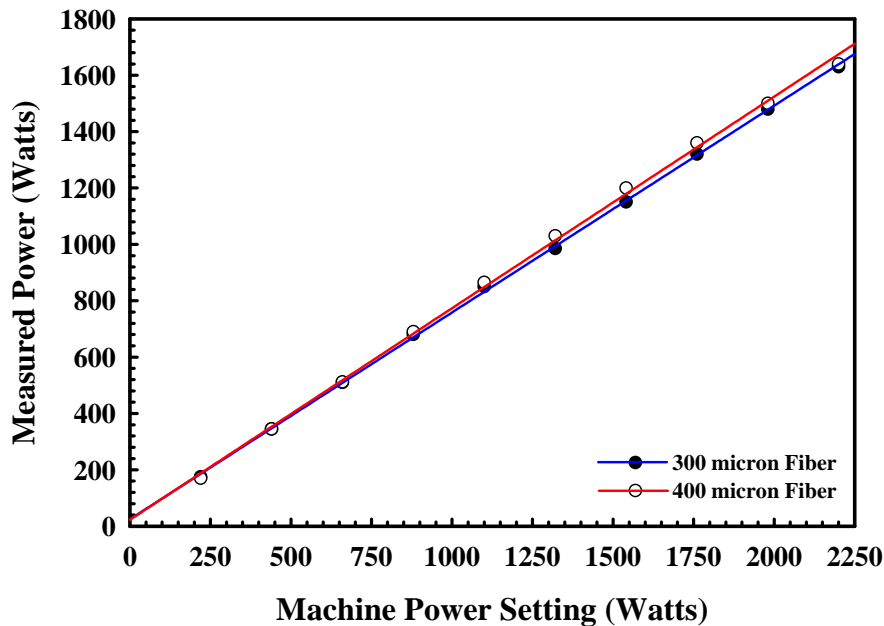


Figure 2. Plot showing comparison between the measured power using a Coherent Watt Meter and the machine power setting for the 300 μm and 400 μm fibers.

Autogenous bead-on-plate laser welds are made on samples measuring nominally 152 mm in length and 25 mm in width. The tantalum samples are 6.0 mm thick, the vanadium samples are 3.2 mm thick, the 304L stainless steel samples are 9.5 mm thick, and the 21-6-9 austenitic stainless steel samples are 12.7 mm thick. Three welds, approximately 43.2 mm in length, are made on each sample. Flat plates are used for each set of weld samples, except the tantalum samples, which have a step joint weld geometry. A schematic diagram showing this joint geometry is shown in Figure 3.

In each series of welds, the effects of changes in the input power and the travel speed on the resulting weld pool shape and size are examined. For the tantalum samples, welds are made at only the maximum laser power setting (2200 W) with travel speeds ranging from 0.85 mm/s to 12.7 mm/s. In the welding studies on the other three materials, the effects of variations in machine power settings from 250 W to 2200 W on the resulting weld pool size and shape are examined at constant travel speeds. These machine power settings cover the range of power settings of which the laser is capable. The effects of changes in travel speed on the resulting weld pool size and shape are also investigated. These travel speeds generally vary from 6.4 mm/sec to 25.4 mm/sec at a constant machine power setting (2200 W). This power setting is the maximum setting of which the machine is capable and allows the maximum depth of penetration to be determined.

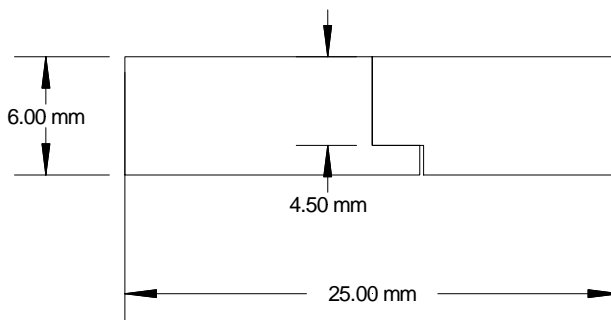


Figure 3. Cross section of the weld coupon showing the step joint configuration. The laser impinges on the top surface of the coupon, and a small gap is left on the bottom to insure no gap along the weld seam.

All welds reported here are made with the laser focus set on the surface of the welding sample. In this sharp focus condition, the theoretical beam diameter is 300 μm . Argon gas is used to shield the welding area and to displace the laser plasma plume during welding. A 4 mm diameter nozzle, placed approximately 25 mm from the laser beam impingement area, with a gas pressure of 80 psi, is used to deliver this shielding gas. During the welding of the tantalum and vanadium samples, back reflection of the beam into the optics assembly is a concern. In order to mitigate this problem, the laser beam was angled 5° towards the leading side of the weld. During welding of the stainless steel samples, this back reflection is not a concern because of the superior coupling between the Nd:YAG laser wavelength light and the stainless steel surface. Therefore, the laser optics assembly is set at an angle normal to the sample surface for the welding of the stainless steel samples.

After welding, a sample is removed from a location near the middle of each weld. This sample is mounted in cross section, polished, and etched to reveal both the microstructure and the resulting weld cross section shape and size. The etchant used to reveal the weld microstructure and fusion zone cross section varies with each material. The tantalum samples have been etched in an aqueous solution consisting of 30 grams of ammonium bifluoride, 20 ml water, and 50 ml nitric acid. For the vanadium samples, an etchant composed of 20 mL ethylene glycol, 10 mL HNO_3 , and 10 mL HF is used to reveal the weldment microstructure and the fusion zone boundary. Because these welds are made on a nominally pure material, it can be difficult to discern the difference between fusion zone and HAZ microstructures. Therefore, care is taken in the metallographic preparation of each sample to ensure that a discernible boundary is

present. In the case of the stainless steels, the fusion zone boundaries are easily discernible, and a typical electrolytic oxalic acid etch is used to reveal the weld pool cross section.

The weld cross sections produced in this study display similar shapes, regardless of the material being welded. These similarities allow a consistent set of measurements to be made on each weld and for these measurements to be compared. A representative cross section in a vanadium weld is shown in Figure 4. Measurements are made on each weld cross section include: (A) the width at the top surface, (B) depth below the surface of the plate, (C) width of the keyhole, and (D) height of weld reinforcement. Another measurement, (E) weld underbead height, is made only on the full penetration welds in vanadium. In addition to these measurements, the total melted area of each weld cross section is determined. All measurements are made from a digital image of each weld cross section using commercially available image analysis software (Adobe Photoshop 7.0 and Media Cybernetics Image Pro Plus V. 4.1).

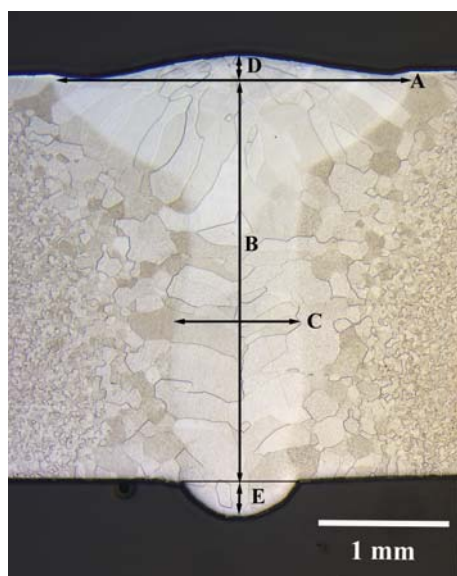


Figure 4. Sample weld cross-section macro showing locations where weld measurements are made. A Weld Width; B Weld Depth; C Keyhole Width; D Weld Reinforcement Height; E Underbead Height. The weld shown in the figure is made in commercially pure vanadium.

The general shape of the weld cross sections provides an indication of the prominent welding mode at each power setting. In laser welding, the conduction and keyhole modes are the two prominent welding modes. Conduction mode laser welding is typical at lower powers, where the heat transfer conditions between the laser beam and the sample surface result in a semi-hemispherical shaped weld pool. A typical conduction mode laser weld in 304L stainless steel is shown in Figure 5. At higher powers, the power densities become high enough, usually on the order of 10^6 W/cm² or higher, to produce strong evaporation on the weld pool surface. As a result, this energetic evaporation produces a recoil pressure, which is sufficient to produce a deep, narrow depression in the molten material, referred to as a keyhole, which is filled with a partially ionized plume of vapor and ambient gas.⁵ Figure 4 displays a typical keyhole mode

⁵ J.Y. Lee, S.H. Ko, D.F. Farson, and C.D. Yoo, "Mechanism of Keyhole Formation and Stability in Stationary Laser Welding," *J. Phys. D: Appl Phys.* **35** (2002) 1570-1576.

laser weld. With the presence of a keyhole, the weld pool cross sections take on a shape, characterized by a semi-hemispherical top and a finger-like protrusion into the material being welded.

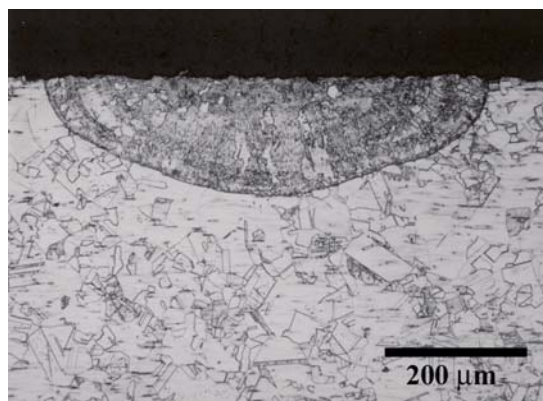


Figure 5. Micrograph showing a conduction mode laser weld made at a machine power setting of 250 W and a travel speed of 19.1 mm/sec in 304L stainless steel.

In high power continuous wave laser welds, the keyhole welding mode is relied upon in order to achieve the desired penetration. Porosity is typically observed and is associated with the stability of the keyhole.⁶ The keyhole is constantly fluctuating and relies on a complex interaction of many factors, including evaporation recoil pressure, hydrodynamic pressures created by the melt and the laser plume, hydrostatic pressure, and surface tension, in order to remain stable. Small fluctuations or variations in the keyhole can result in the formation of small perturbations on the keyhole walls or its complete collapse. These instabilities thus result in the ejection of metal vapor and entrapped shielding gas from the keyhole column, leaving behind a non-continuous trail of pores along the longitudinal orientation of the weld, as shown in Figure 6. This figure shows the microstructure present in a plane sectioned along the centerline of a tantalum laser weld made at an input power of 1900 W and a travel speed of 2.54 mm/sec. A line of porosity is observed near the root of the weld.

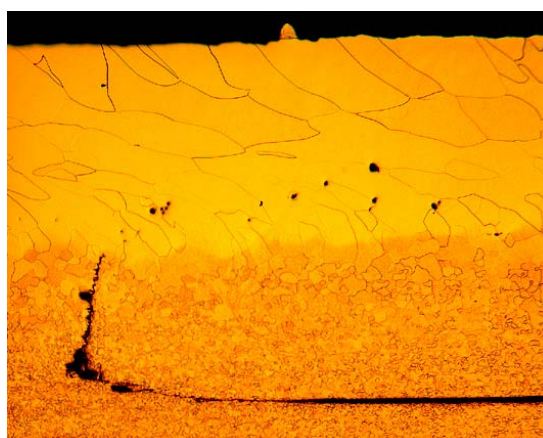


Figure 6. Longitudinal section through the centerline of laser weld made at an input power of 1900 W and a travel speed of 2.54 mm/sec in tantalum.

⁶ A. Matsunawa, "Problems and Solutions in Deep Penetration Laser Welding," *Science and Technology of Welding and Joining*, **6(6)** (2001) 351-354.

Results

Refractory Metals

Tantalum

A total of six welds have been made at the maximum machine power setting and travel speeds ranging from 0.85 mm/sec to 12.7 mm/sec. All other variables have been held constant. Micrographs of the weld cross sections are shown in Figures 7(a-f). Each weld displays a shape typical of the keyhole welding mode. Substantial grain growth occurred in the heat affected zone (HAZ) of the welds, particularly at the lower travel speeds. Such grain growth in the HAZ and large fusion zone grains are typical of welds in high purity tantalum. Evidence of weld porosity appears in several of the welds, especially at the lower travel speeds. The surface of the welds showed only small amounts of undercutting at the higher speeds, but increased significantly as the weld speed decreased. No cracking was observed in any of the welds.

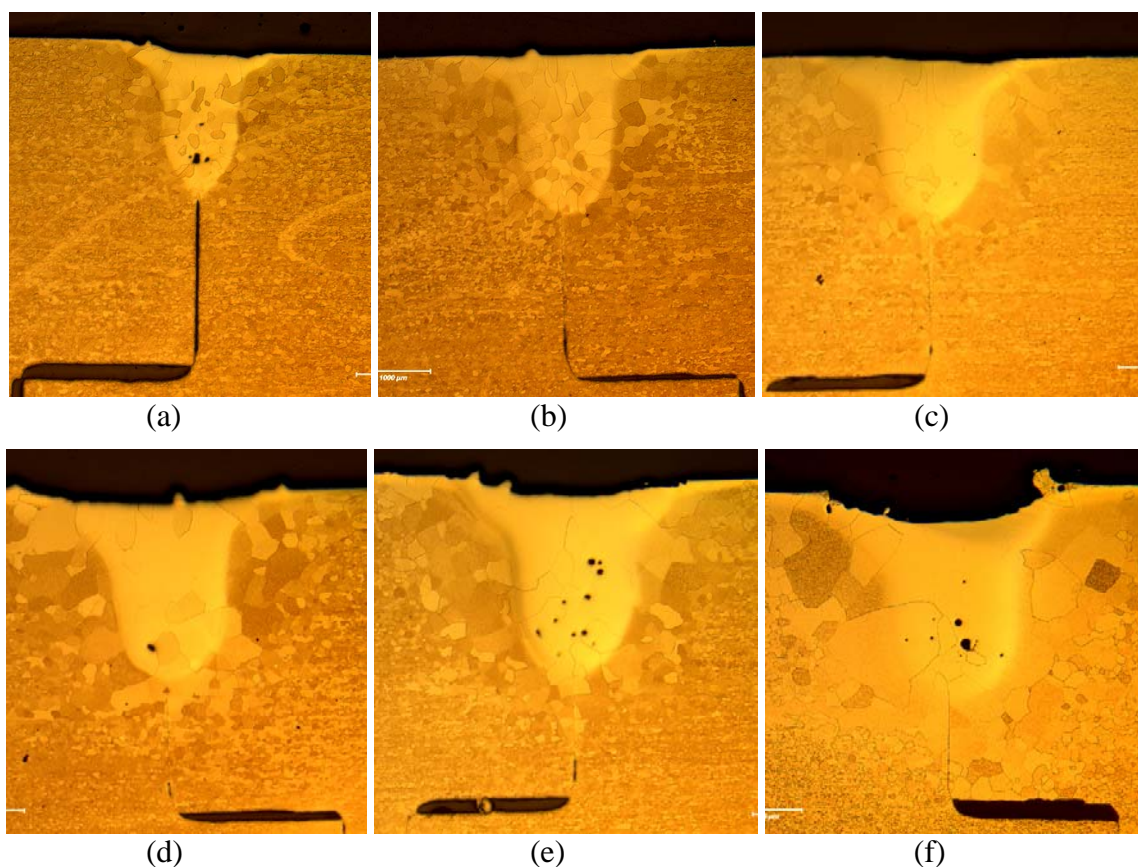


Figure 7. Metallographic cross sections of the six welds made in commercially pure tantalum at a delivered power of 1.9kW on the surface of the tantalum coupons. a) 12.7 mm/s, b) 6.4 mm/s, c) 3.8 mm/s, d) 2.54 mm/s, e) 1.70 mm/s, f) 0.85 mm/s. The distance to the step in each figure is 4.50 mm.

The laser welding parameters and the measured depths and widths of each weld are summarized in Table 4. Along with measurements of the weld width and depth, the energy input and aspect ratio for each weld are included. The value for the energy input is based on a relationship between the measured power input to the sample and the weld travel speed. The use

of this parameter, defined as the input power divided by the travel speed, is a more general description of the energy imparted on the workpiece than simply the machine power setting. The aspect ratio is defined as the depth-to-width ratio of the welds. This value provides a measure of the general shape of the weld fusion zone not available with simple width and depth measurements alone. The measured weld depths gradually increase with decreasing travel speed until a maximum penetration of 2.9 mm is achieved with the slowest weld travel speed. The measured weld widths, which are larger than the weld depths, also increase with decreasing travel speed, albeit at a faster rate. As a result, the measured depth-to-width ratios decrease from 0.91 to 0.66 with the decreasing weld speed.

Another weld study has also been performed using tantalum weld samples on the CW Nd:YAG laser located at LANL⁷. In this study, the effects of changes in laser power from 500 W to 2000 W at a constant weld travel speed (12.7 mm/sec) on the resulting weld pool size and shape are examined. The results of this study are summarized in Table 5. Even though the fiber diameter, optics, and incident laser angle for the LANL welding system are different than those used with the LLNL system, the weld penetration, approximately 2 mm, is similar at the 0.15kJ/mm level at in both cases.

Table 4. Summary of laser welds made in tantalum at LLNL at an input power of 1630 W.

<u>Travel Speed(mm/s)</u>	<u>Energy/Length (kJ/mm)</u>	<u>Weld Depth (mm)</u>	<u>Weld Width (mm)</u>	<u>Aspect Ratio</u>
12.7	0.13	2.0	2.2	0.91
6.40	0.26	2.2	2.6	0.85
3.81	0.43	2.3	3.1	0.74
2.54	0.63	2.5	3.7	0.68
1.70	1.00	2.7	3.5	0.77
0.85	1.89	2.9	4.4	0.66

Table 5. Summary of laser welds made in tantalum at LANL at a travel speed of 12.7 mm/sec and an incident angle of 10° with a helium shielding gas.

<u>Machine Power Setting (W)</u>	<u>Energy/Length (kJ/mm)</u>	<u>Weld Depth (mm)</u>	<u>Weld Width (mm)</u>	<u>Aspect Ratio</u>
500	0.039	0.100	0.336	0.298
1000	0.079	0.471	0.471	1.000
1500	0.118	1.576	1.612	0.978
1750	0.138	1.776	1.777	0.999
2000	0.157	2.200	2.436	0.903

The measured weld dimensions from both studies are plotted in Figures 8(a)-8(c) as a

⁷ T. A. Palmer et al. "Characterization of Stainless Steel and Refractory Metal Welds Made Using a Diode-Pumped, Continuous Wave Nd:YAG Laser," Lawrence Livermore National Laboratory, UCRL-ID-146005, 39 pages, November, 2001.

function of the energy input per unit length. In these plots, the open triangle symbols represent the results from the LANL welding system, and the solid circles represent the results from the LLNL welding system. A maximum weld depth of 2.9 mm is shown. However, the practical limit is actually only approximately 2.3 mm, because of the defects present in the welds at the slow travel speeds. By using the energy input per unit length, results from the two studies can be directly compared. Figure 8(a) compares the weld depths for the two studies, and reveals notably different trends for each. The results from the LANL welder are measured at different power levels and a single travel speed (12.7 mm/s) and display a nearly linear trend over the range of energy inputs. The results from the LLNL welder are measured at different travel speeds and a constant power setting and display much less of an increase in penetration as the energy input is increased. In fact, the weld depth only increases 50% with a 15x increase in energy input. The marginal increase in penetration with energy input is common in slow speed laser welds, and results from the interaction time of the heat source with the base metal. Since the heat has more time to diffuse away from the liquid weld pool at lower travel speeds, wider welds relative to their depths are produced. This behavior is apparent in both the weld width measurements, presented in Figure 8(b), and the aspect ratio of the welds, presented in Figure 8(c). In this latter figure, the depth-to-width ratio of the welds decreases with travel speed.

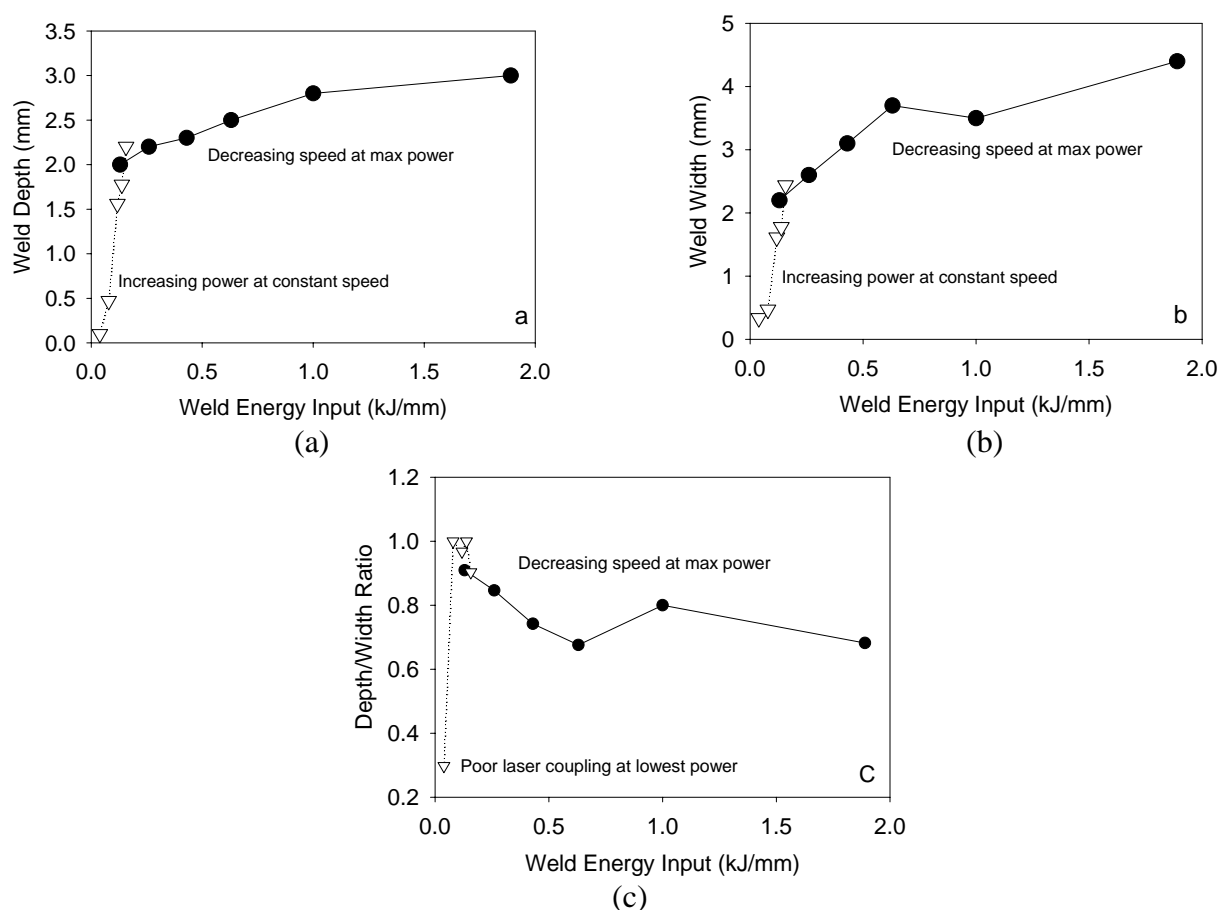


Figure 8(a-c). Plots showing the (a) weld depth, b) weld width, and c) weld aspect ratio, plotted versus energy input for the welds made in tantalum. The open triangles give results of the laser power study at a constant weld speed of 12.7 mm/s, while the open circles give results of the weld speed study at the max laser power of 2.2 kW.

Vanadium

The effects of variations in both the input power and travel speed on the cross section size and shape of vanadium welds are examined. In these experiments, machine power settings range from 250 W to 2200 W at travel speeds of 12.7 mm/sec, 19.1 mm/sec, and 25.4 mm/sec. Micrographs showing the weld cross sections for machine power settings between 500 W and 2000 W are shown in Figures 9 through 11 at travel speeds of 12.7 mm/sec, 19.1 mm/sec, and 25.4 mm/sec, respectively. In general, the weld cross sections shown in these figures display a shape characteristic of a keyhole welding mode, and the welds contain varying degrees of porosity. All of the welds, with the exception of the one performed at a machine power setting of 2000 W and a travel speed of 12.7 mm/sec (Figure 11(d)), are also partial penetration welds.

A summary of the weld pool cross section measurements for each of the travel speeds is shown in Table 6. Full penetration welds are observed at the two highest power inputs (1494 W and 1630 W) at the lowest travel speed (12.7 mm/sec). In each of these welds, an additional weld underbead appears on the back side of the weld sample. Plots comparing the primary weld measurements (width, depth, aspect ratio, and melted area) with the input power for each travel speed are shown in Figures 12(a-d). With increasing power, the weld width and depth increase. Of the three travel speeds, the highest widths and depths are observed at the lowest travel speed (12.7 mm/sec). On the other hand, there appears to be little difference in the measured widths and depths for welds made at the two higher travel speeds (19.1 and 25.4 mm/sec). These measurements can then be combined into the aspect ratio, which is plotted as a function of input power in Figure 12(c). In this case, the differences between the three travel speeds are minimized, and the aspect ratios for each travel speed show a general increase as the power input is increased to a value of approximately 1250 W. Above this level, the aspect ratios show no further increases and maintain a constant level. Similar trends are observed when the melted areas of the weld cross section are plotted as a function of the input power in Figure 12(d).

Two other measurements of interest are made on each weld pool cross section. These measurements of the keyhole width and the reinforcement height provide measures of the general properties of the keyhole and of the amount of weld porosity in partial penetration welds, respectively. Plots of the keyhole width and reinforcement height are shown in Figures 13(a&b), respectively, as a function of the power input. The keyhole width values, shown in Figure 13(a), display a general increase with increasing power input, albeit with more scatter in the data. The reinforcement height values also increase with increasing power input, but no distinct trend arises for the individual travel speeds. This increasing trend appears to follow the same general trend observed in the micrographs, where porosity appears in the keyhole mode welds made at higher powers.

In addition to plotting the weld pool measurements as a function of the input power, the trends in these measurements can be examined as a function of the energy input per unit length. These values are listed in Table 6. The weld width, depth, aspect ratio, and total melted area are plotted as a function of the energy input per unit length in Figures 14(a-d). Trends showing increasing weld dimensions with increasing energy input are observed in these figures. On the other hand, the more rapid travel speeds appear to produce both wider and deeper weld pools than the lower travel speeds for a given energy input. This trend is the opposite of that observed in Figures 12(a-d) when the weld dimensions are plotted as a function of the input power. Such a reversal is related to the higher input power required at the higher travel speeds in order to

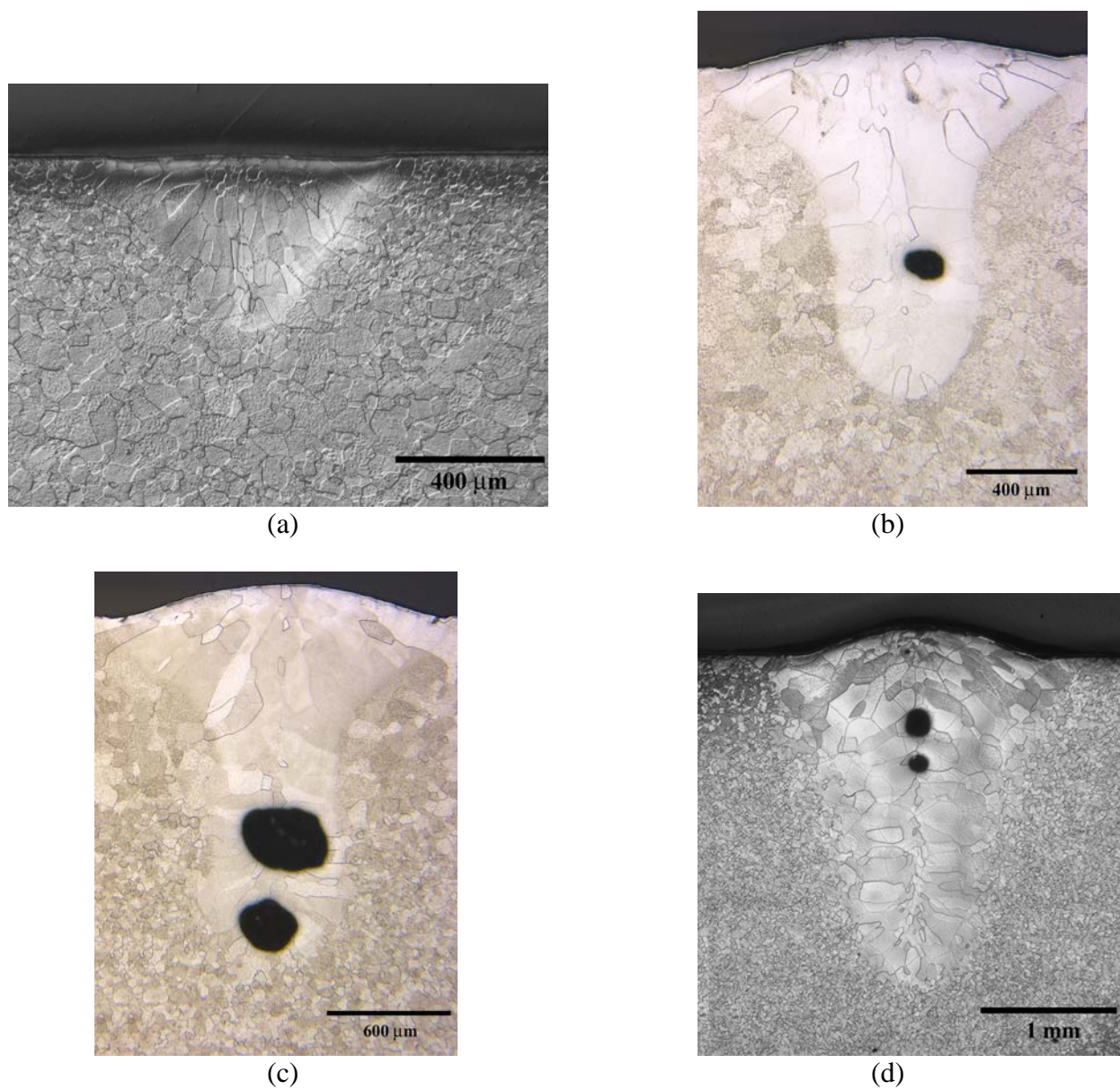


Figure 9(a-d). Micrographs of weld cross sections for machine power settings of (a) 500 W, (b) 1000 W, (c) 1500 W, and (d) 2000 W for a travel speed of 25.4 mm/sec in commercially pure vanadium. Note the variations of magnification in the micrographs.

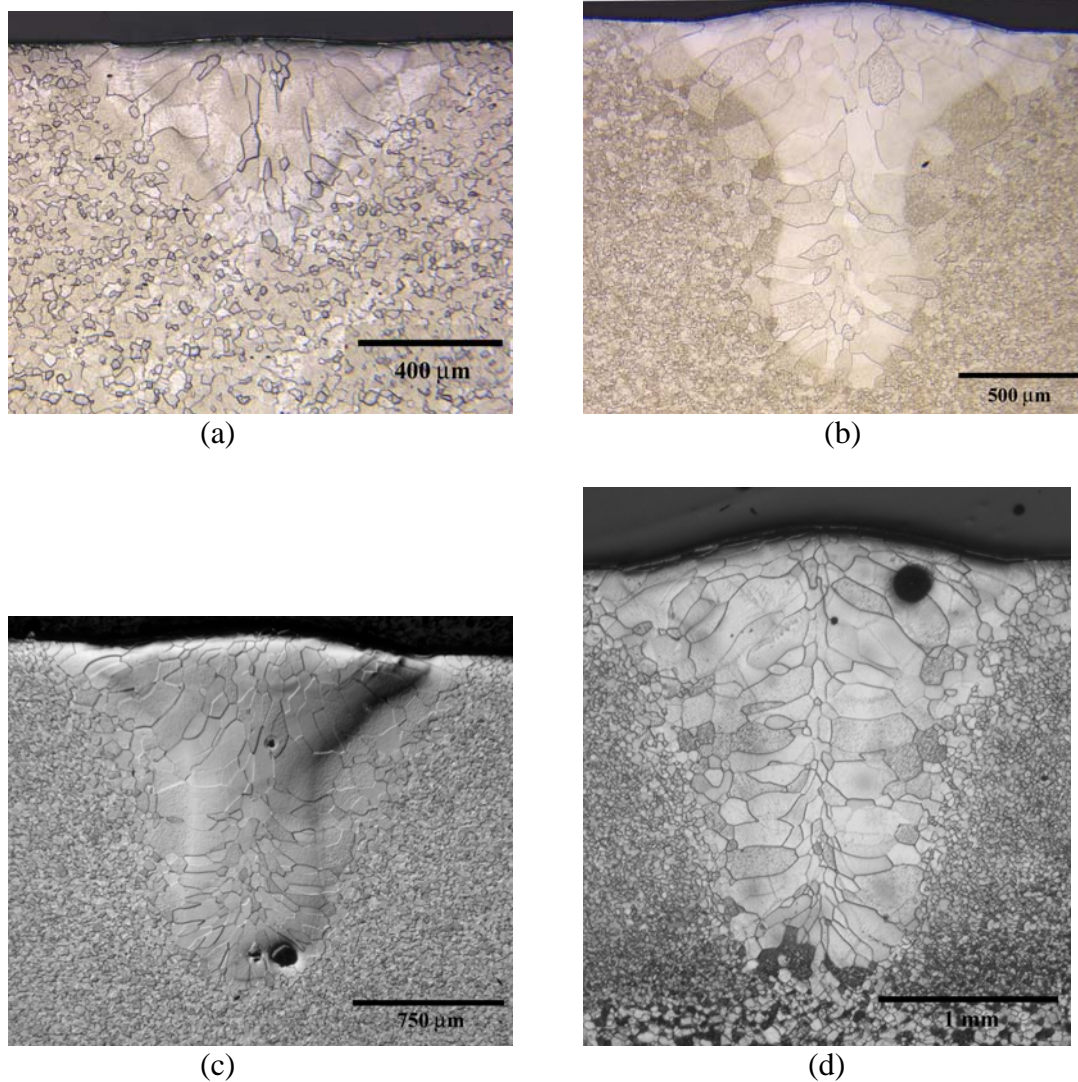
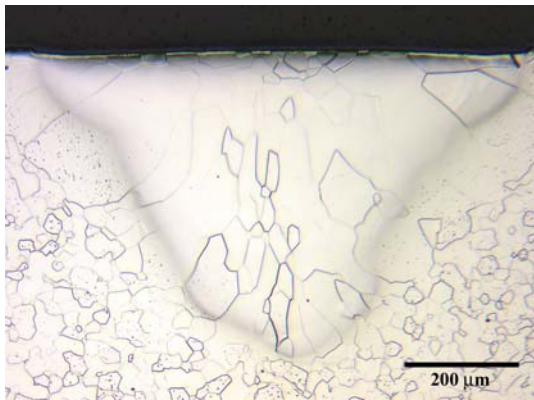
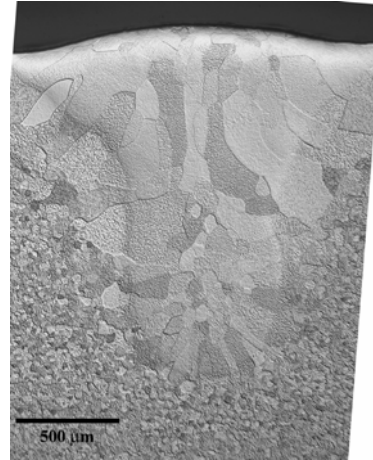


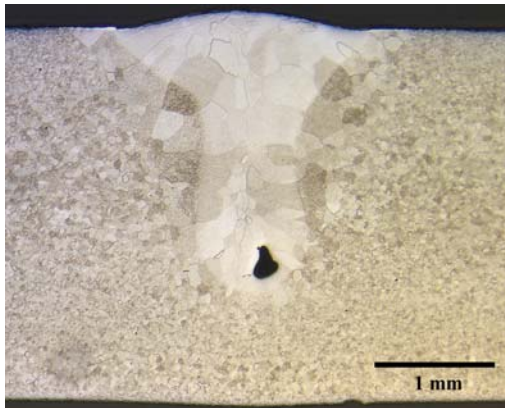
Figure 10(a-d). Micrographs of weld cross sections for machine power settings of (a) 500 W, (b) 1000 W, (c) 1500 W, and (d) 2000 W for a travel speed of 19.1 mm/sec in commercially pure vanadium. Note the variations of magnification in the micrographs.



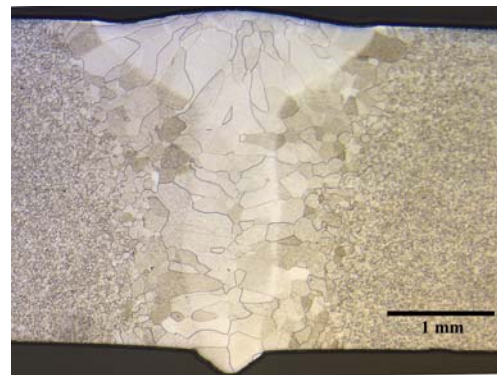
(a)



(b)



(c)



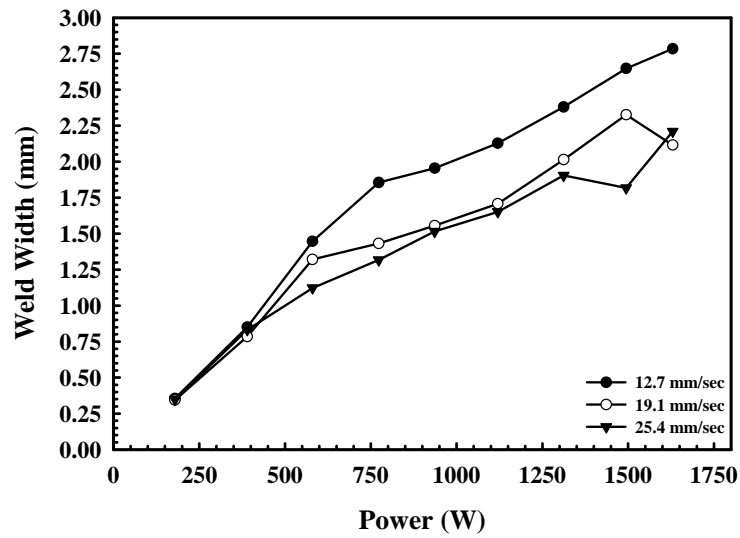
(d)

Figure 11(a-d). Micrographs of weld cross sections for machine power settings of (a) 500 W, (b) 1000 W, (c) 1500 W, and (d) 2000 W for a travel speed of 12.7 mm/sec in commercially pure vanadium. Note the variations of magnification in the micrographs.

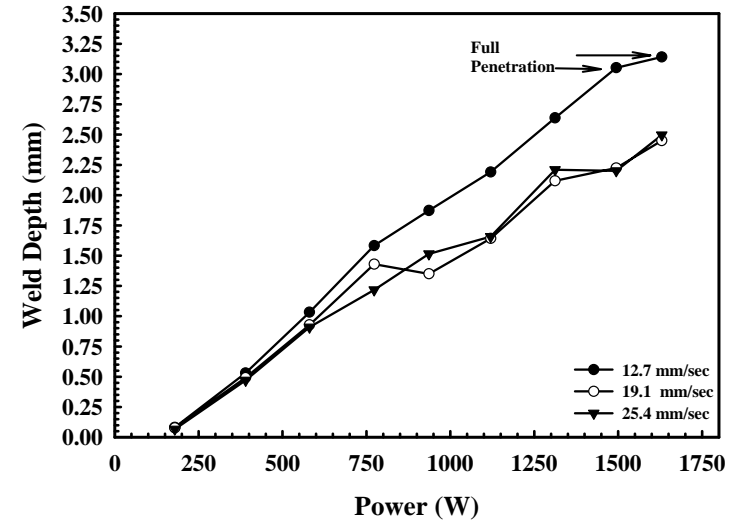
Table 6. Summary of measurements made on vanadium weld samples.

<u>Power</u> <u>(Watts)</u>	<u>Energy Input</u> <u>(J/mm)</u>	<u>Weld Width</u> <u>(mm)</u>	<u>Weld Depth</u> <u>(mm)</u>	<u>Aspect Ratio</u> <u>(Depth/Width)</u>	<u>Keyhole Width</u> <u>(mm)</u>	<u>Reinforcement</u> <u>Height (mm)</u>	<u>Melted Area</u> <u>(mm²)</u>
<i>Travel Speed = 25.4 mm/sec</i>							
179	7.1	0.35	0.07	0.19	----	----	0.02
390	15.4	0.74	0.14	0.19	----	----	0.13
580	22.8	1.12	0.91	0.81	0.45	0.05	0.55
773	30.4	1.32	1.22	0.92	0.51	0.09	0.89
936	36.9	1.52	1.51	1.00	0.55	0.12	1.24
1120	44.1	1.65	1.66	1.00	0.62	0.15	1.49
1312	51.7	2.21	2.50	1.13	0.74	0.17	2.71
1494	58.8	1.90	2.18	1.15	0.63	0.17	2.08
1630	64.2	2.13	2.28	1.07	0.92	0.22	2.31
<i>Travel Speed = 19.1mm/sec</i>							
179	9.4	0.34	0.08	0.23	----	----	0.02
390	20.5	0.78	0.49	0.63	0.33	0.03	0.24
580	30.4	1.32	0.93	0.70	0.51	0.06	0.73
773	50.6	1.43	1.43	1.00	0.55	0.09	1.09
936	49.1	1.56	1.35	0.87	0.38	0.09	1.15
1120	58.8	1.65	1.55	0.94	0.64	0.12	1.36
1312	68.9	1.65	1.64	0.99	0.56	0.11	1.47
1494	78.4	2.12	2.24	1.06	0.71	0.20	2.47
1630	85.6	2.12	2.45	1.16	0.76	0.18	2.69
<i>Travel Speed = 12.7mm/sec</i>							
179	14.1	0.35	0.08	0.23	----	----	0.02
390	30.7	0.85	0.53	0.62	0.35	----	0.27
580	45.7	1.45	1.03	0.71	0.55	0.07	0.83
773	60.9	1.86	1.58	0.85	0.88	0.13	1.55
936	73.7	1.95	1.87	0.96	0.68	0.13	1.75
1120	88.2	2.13	2.19	1.03	0.92	0.15	2.50
1312	103.3	2.38	2.64	1.11	0.84	0.16	3.04
1494*	117.6	2.65	3.05	1.15	0.87	0.13	3.72
1630*	128.3	2.78	3.14	1.13	1.01	0.13	4.24

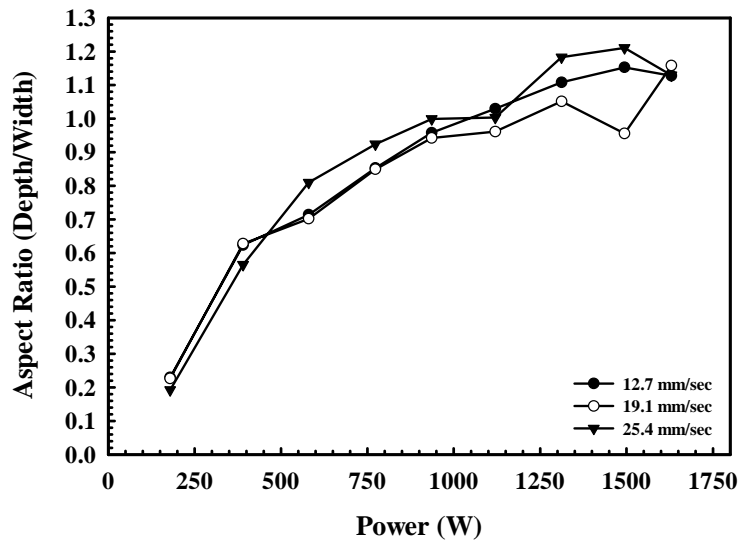
* Full Penetration Welds



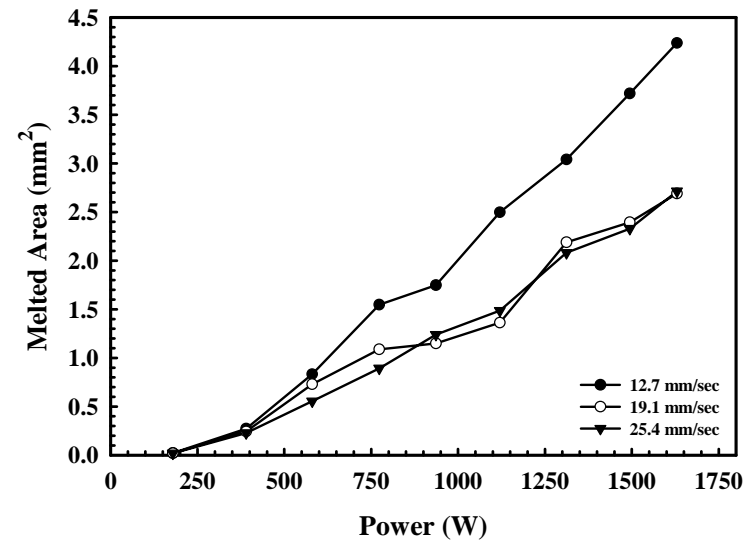
(a)



(b)



(c)



(d)

Figure 12(a-d). Plots showing variations in the (a) weld width, (b) weld depth, (c) aspect ratio (depth/width), and (d) melted area with changes in the machine output power or travel speeds of 25.4 mm/sec, 19.1 mm/sec and 12.7 mm/sec for welds made in commercially pure vanadium.

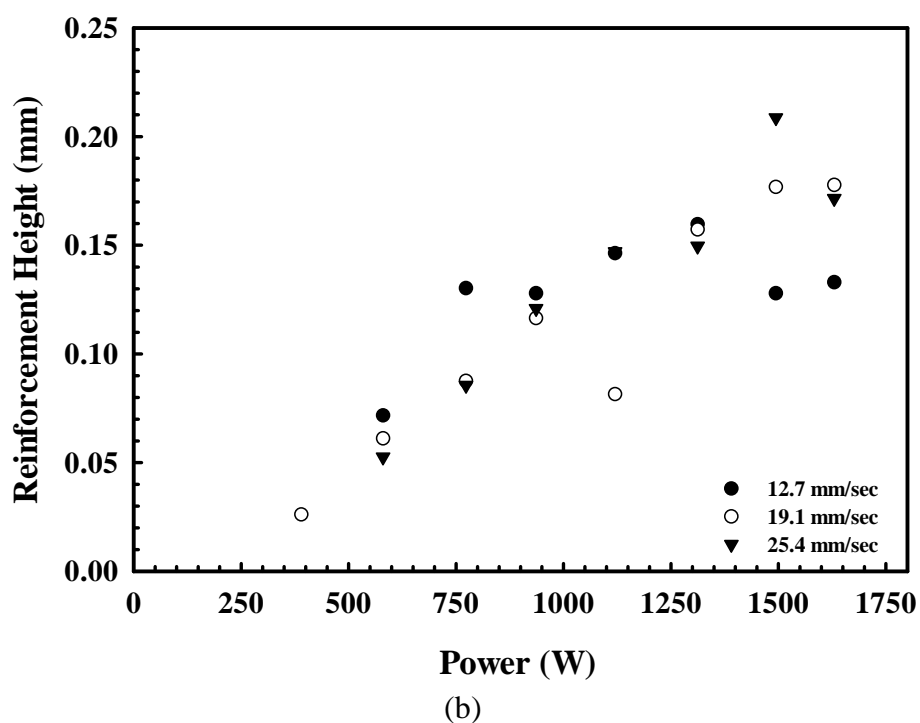
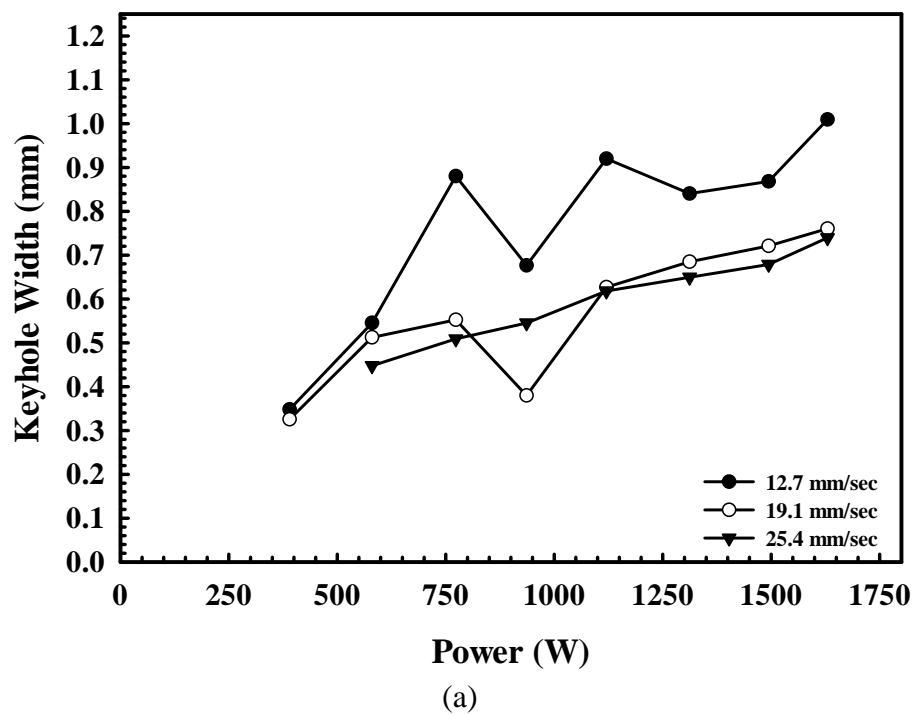
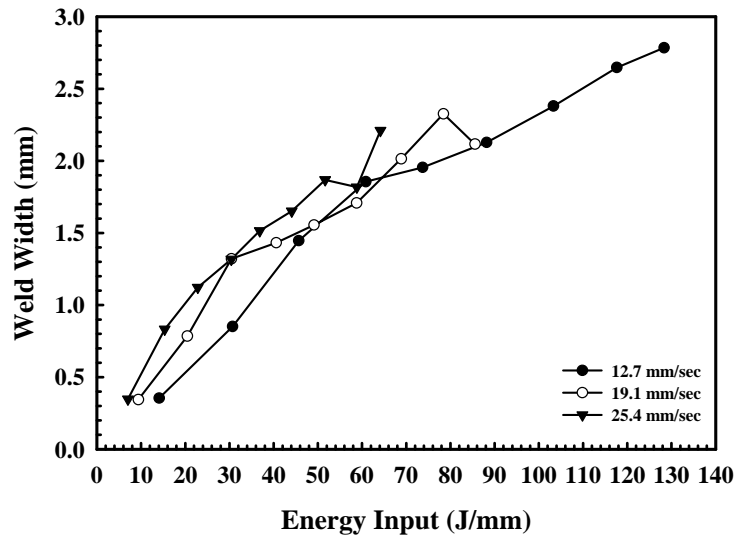
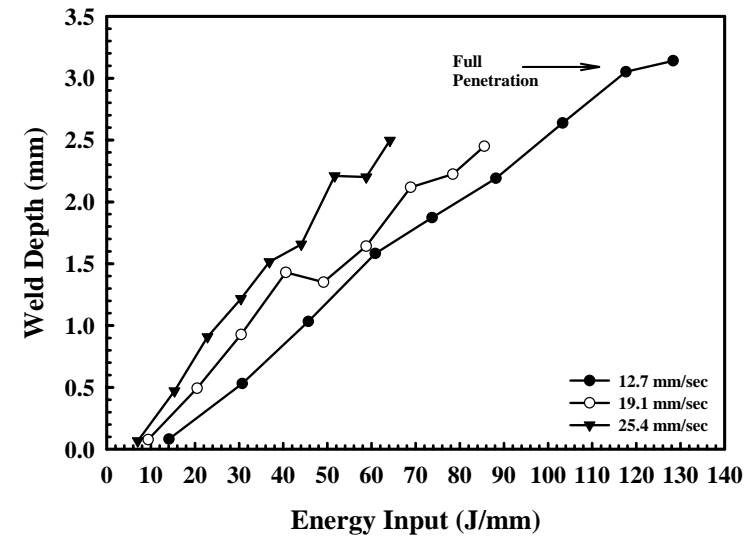


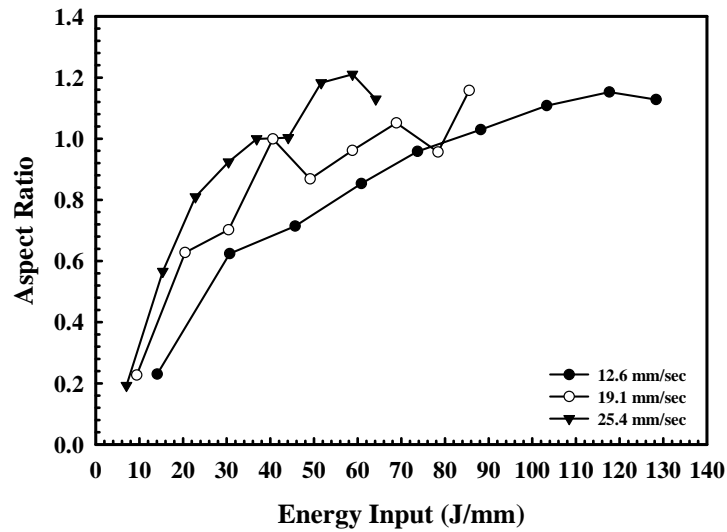
Figure 13(a&b). Plots showing variations in the (a) keyhole width and (b) overfill height with changes in the machine output power setting for travel speeds at 25.4 mm/sec, 19.1 mm/sec and 12.7 mm/sec for welds made in commercially pure vanadium.



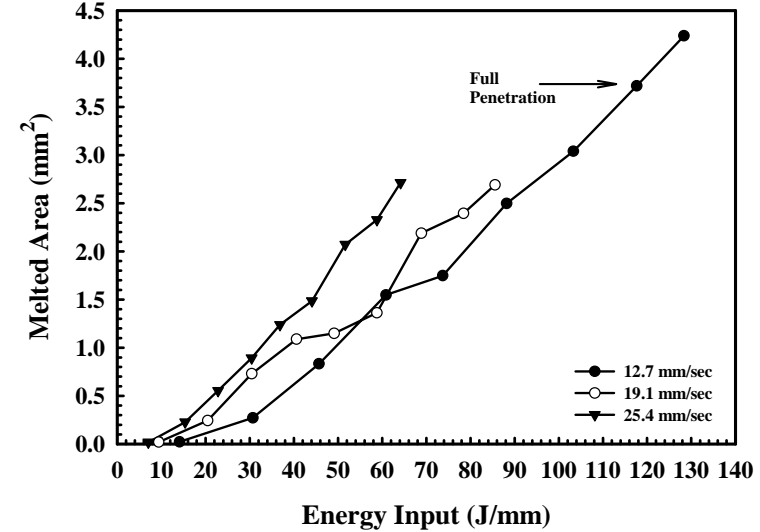
(a)



(b)



(c)



(d)

Figure 14(a-d). Plots showing variations in the (a) weld width, (b) weld depth, (c) aspect ratio (depth/width), and (d) melted area with changes in the energy input at travel speeds of 25.4 mm/sec, 19.1 mm/sec and 12.7 mm/sec for welds made in commercially pure vanadium.

reach an equivalent energy input per unit length. For example, in order for an energy input per unit length of 50 J/mm to be attained at travel speeds of 25.4 and 12.7 mm/sec, power inputs of 1270 W and 635 W, respectively, are required.

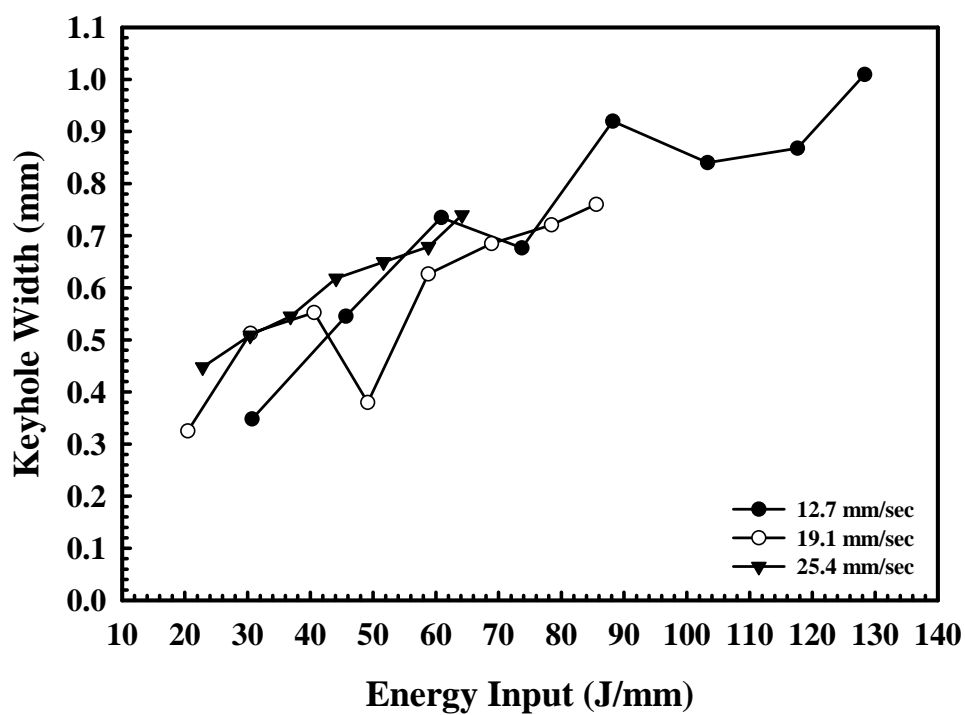
In Figures 15(a&b), the effects of changes in the energy input per unit length on the keyhole width and reinforcement height, respectively, are shown. Both parameters show increasing trends with increases in the energy input. The same trends noted in Figures 14(a-d), in which the higher travel speed produces larger weld dimensions at equivalent energy inputs, are also present here, especially with the reinforcement height measurements shown in Figure 15(b). The trend is not as evident in the keyhole width measurements, shown in Figure 15(a), where the measurements from the three travel speeds fall within a close proximity of each other at comparable energy inputs.

Comparisons are also made between the results obtained from the LLNL laser system and those from the LANL system. A summary of the measurements made on the weld cross sections produced by the LANL system is shown in Table 7. Even though the systems are comparable and the welds are made on material taken from a common source, there are differences between the two sets of experiments which are worth noting. First, the LANL welding experiments have been performed with both helium and argon shielding gases, whereas only argon has been used in the LLNL experiments. There is also a difference in the laser offset angle used in the two experiments. The LLNL results are based on an offset angle of 5°, while the LANL results are based on an offset angle of 10° towards the leading edge of the weld pool. Therefore, the effects of not only changes in power input on the resulting weld pool cross section dimensions can be compared, but also the basic effects of shielding gases and offset angle can be analyzed.

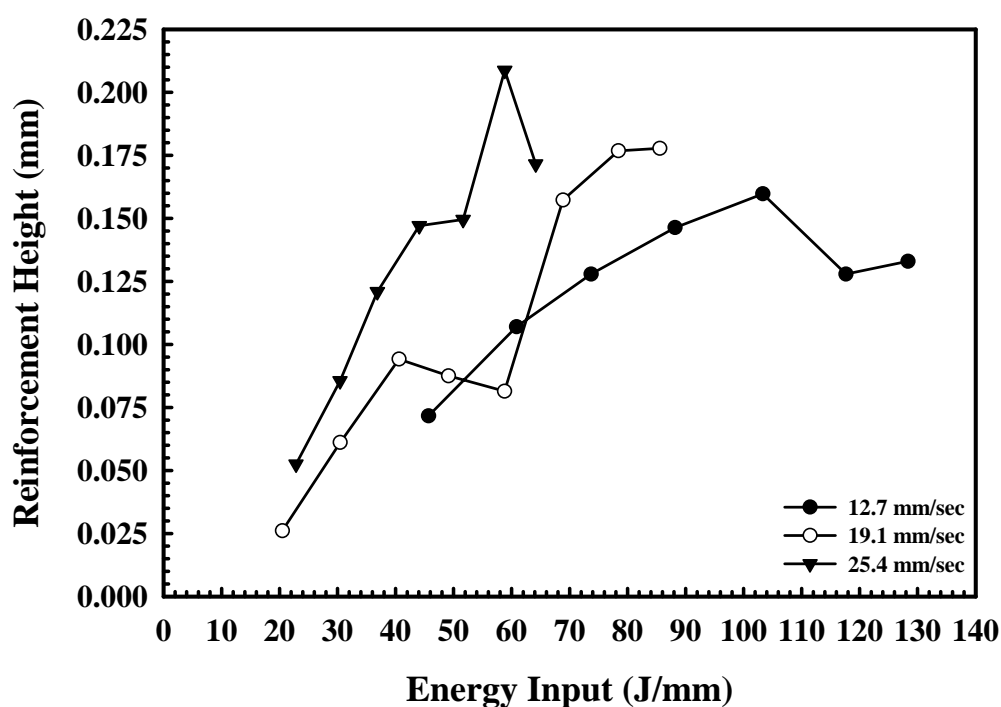
Figures 16(a-d) show comparisons between the measured weld depth, width, aspect ratio, and total melted area, respectively, for measurements made on both systems at a travel speed of 19.1 mm/sec. These values are plotted in each figure as a function of the machine power setting, which is used because comparable measurements of the input power at the sample surface have not been performed on the LANL system. Without these measurements, the power loss from the laser optics between the laser power supply and the sample surface can not be determined, making the machine power setting the only common value with which to compare the results from the different systems.

The results from the two comparable laser welding systems follow the same general trends. Overall, the results from the LLNL system compare most favorably with the LANL results using helium as a shielding gas at machine power settings up to approximately 1000 W. Additional comparisons between these two welding systems have also been performed on measurements of the keyhole width and weld reinforcement height in Figures 17(a&b), respectively. In these plots, the variations between the LANL and LLNL results are similar to those observed with other weld pool measurements. In terms of the keyhole width, the LANL system produces welds with much wider keyholes than the LLNL system. This increased keyhole width can be attributed, in part, to the wider laser beam spot size characteristic of the LANL system.

A comparison between the LANL results using an argon shielding gas and the LLNL results reveals a different relationship. Whereas the weld widths are comparable, as shown in Figure 17(a), the LANL results using argon as a shielding gas tend to display the lowest weld depths, aspect ratios, and total melted areas. Overall, the use of helium as a shielding gas with the LANL laser produces a larger weld, particularly in terms of the melted area. This effect is most



(a)

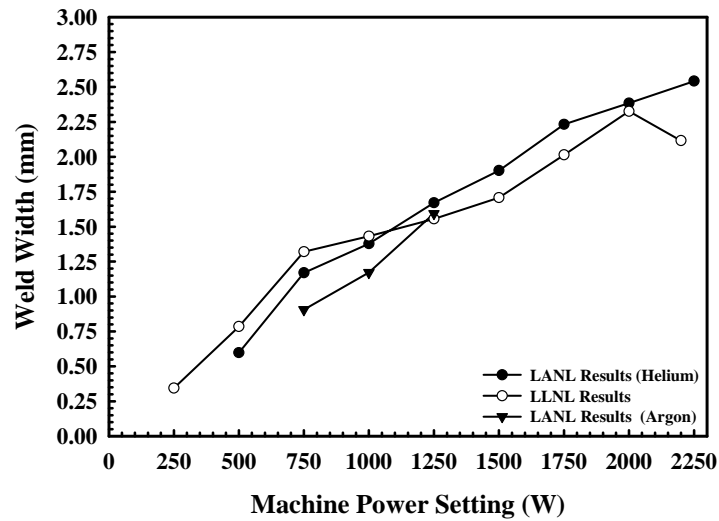


(b)

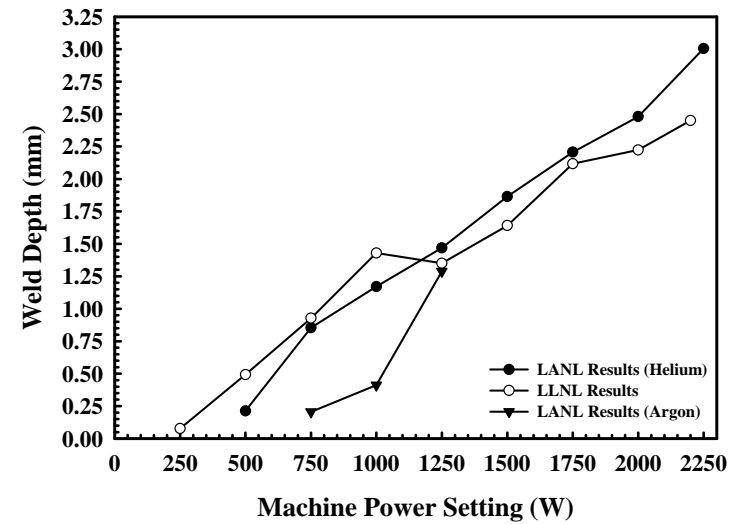
Figure 15(a&b). Plots showing variations in the (a) keyhole width and (b) overfill height with changes in the energy input per unit length at travel speeds at 25.4 mm/sec, 19.1 mm/sec and 12.7 mm/sec for welds made in commercially pure vanadium.

Table 7. Summary of measurements made on vanadium weld samples under similar experimental conditions using the LANL Laser Welder and a travel speed of 19.7 mm/sec.

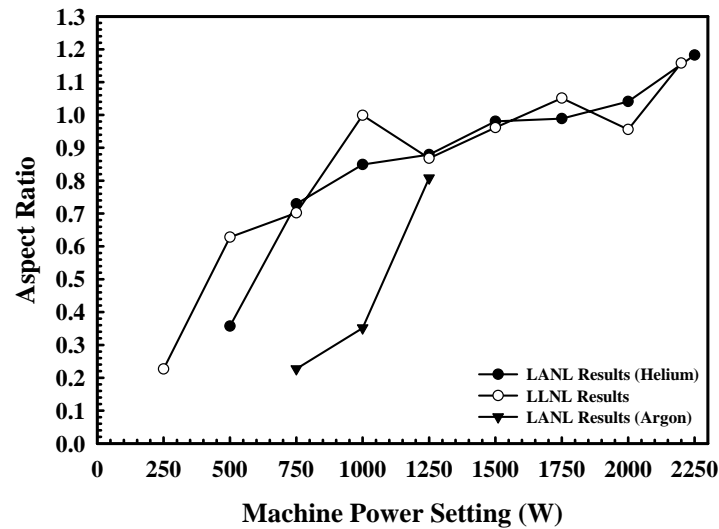
<u>Machine Power (Watts)</u>	<u>Shielding Gas</u>	<u>Weld Width (mm)</u>	<u>Weld Depth (mm)</u>	<u>Aspect Ratio (Depth/Width)</u>	<u>Keyhole Width (mm)</u>	<u>Reinforcement Height (mm)</u>	<u>Melted Area (mm²)</u>
250	Helium	----	----	----	----	----	----
500	Helium	0.598	0.213	0.357	----	----	0.095
750	Helium	1.170	0.853	0.729	----	----	0.681
1000	Helium	1.378	1.170	0.849	0.7925	0.0792	1.002
1250	Helium	1.671	1.469	0.808	1.1765	0.0977	1.669
1500	Helium	1.902	1.865	0.981	1.2070	0.1097	2.295
1750	Helium	2.232	2.207	0.989	1.3777	0.1341	3.162
2000	Helium	2.384	2.481	1.041	1.6947	0.1402	4.181
2250	Helium	2.542	3.005	1.182	1.5302	0.1646	5.149
750	Argon	0.906	0.206	0.227	----	0.1341	0.123
1000	Argon	1.171	0.412	0.352	----	0.1402	0.356
1250	Argon	1.594	1.288	0.808	1.2706	0.1646	1.567



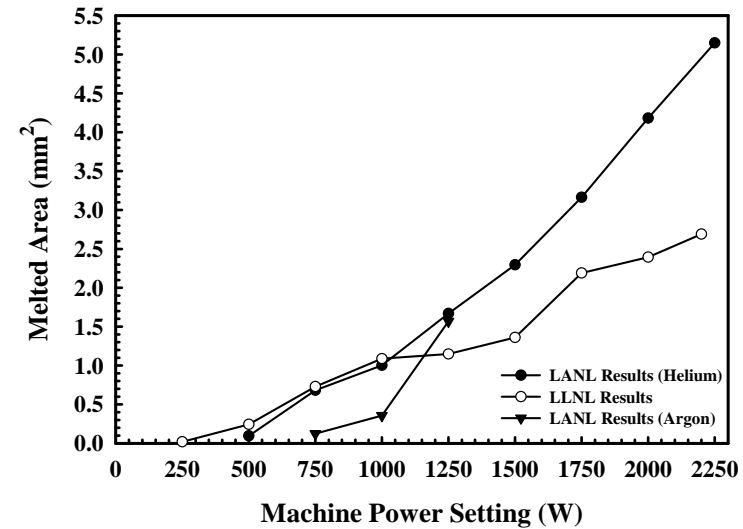
(a)



(b)

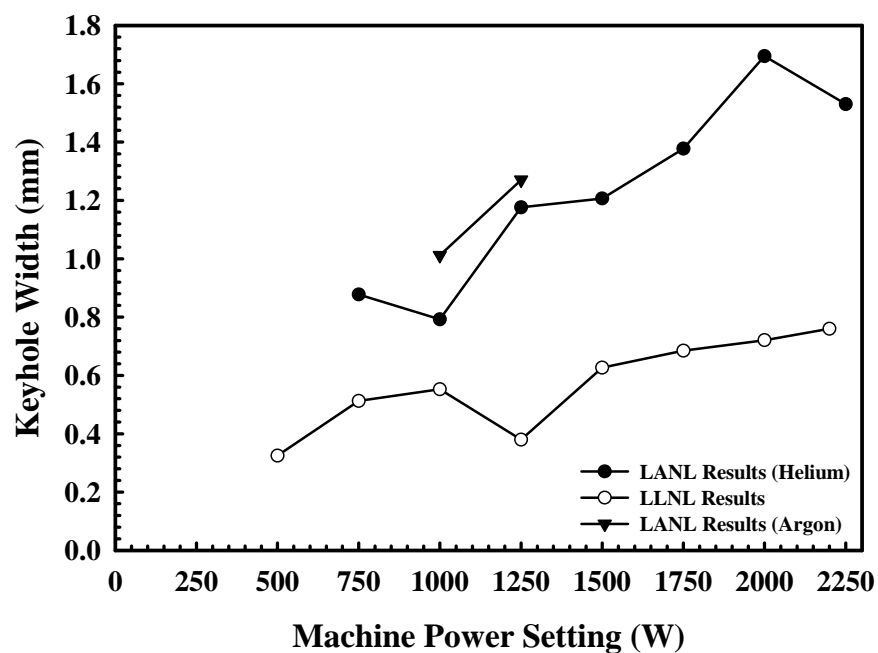


(c)

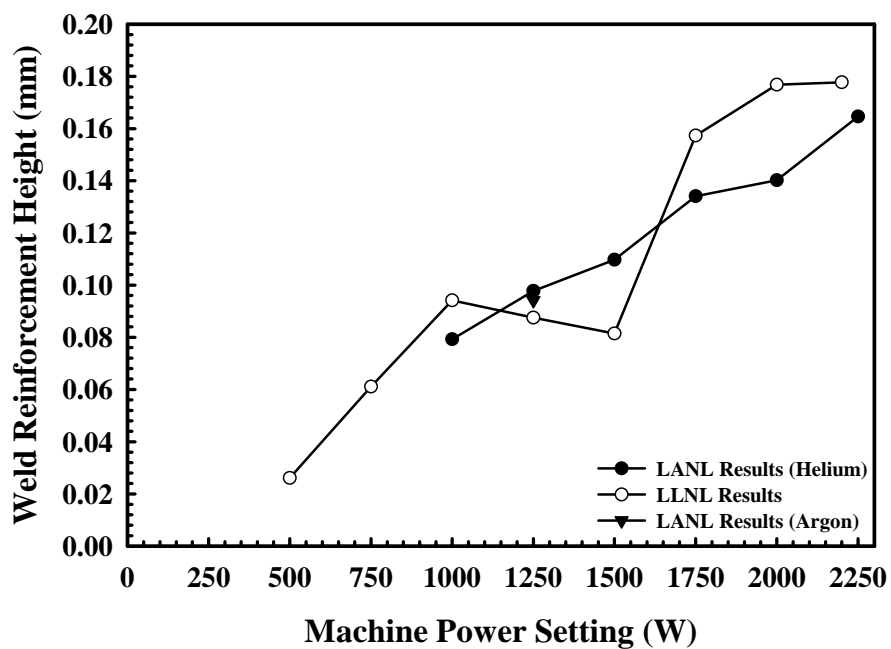


(d)

Figure 16(a-d). Comparison between (a) weld width, (b) depth, (c) aspect ratio, and (d) melted area with changes in weld power at a travel speed of 19.1 mm/sec for welds made on commercially pure vanadium using the LLNL and LANL welders.



(a)



(b)

Figure 17(a&b). Comparisons between the (a) keyhole width and (b) overfill height with changes in weld power at a travel speed of 19.1 mm/sec for welds made in commercially pure vanadium using the LLNL and LANL welders.

pronounced at higher power settings. Further investigation of the effects of the choice in shielding gases on the weld pool size and shape is required in order to determine if this effect can be transferred to the LLNL system.

Refractory Metal Welding Overview

Based on the results presented above, there are several conclusions which can be made regarding the welding of refractory metals with diode pumped CW Nd:YAG lasers. In each case, keyhole welding modes are obtained over the range of machine power settings above 500 W. The conversion from conduction mode to keyhole mode welding occurs at higher power levels with more rapid travel speeds in vanadium. By taking advantage of the keyhole welding mode and slow weld speeds, weld depths up to 2.9 mm in tantalum and 3.2 mm in vanadium are possible. However, the practical limit for weld penetration in tantalum is only approximately 2.3 mm, due to weld defects that occurred at lower travel speeds. These defects appear in the form of weld porosity, which is believed to originate from the collapse of the keyhole during welding. Neither the tantalum nor the vanadium welds produced here display any evidence of solidification cracking or other similar defects.

Even though slower travel speeds are shown to increase the weld depth, the appearance of porosity worsens, thus compromising the integrity of the weld. Slow travel speeds are also not desirable because of the increased heat input to the part being welded and the enhanced potential for weld distortion. It is therefore desirable to achieve deeper penetrations by maintaining a fairly rapid travel speed and increasing the input power. Based on the power variation studies performed in vanadium, it is possible to achieve greater weld depths with higher powers, which can be achieved in higher power lasers. Such systems with power levels of 4.4 kW are currently available. As the technology further matures, this power level will surely increase.

Stainless Steels

304L Austenitic Stainless Steel

Power Variation Studies

A series of welds in 304L austenitic stainless steel samples have been made with machine power settings range from 250 W to 2200 W at travel speeds of 12.7 mm/sec and 19.1 mm/sec. Micrographs showing the weld cross sections for four of these machine power settings between 500 and 2000 W at travel speeds of 19.1 mm/sec and 12.7 mm/sec are shown in Figures 18 and 19, respectively. There are two characteristics common to the micrographs in each of these figures. The first characteristic involves the general shape of the weld cross sections, which are indicative of a keyhole welding mode. The second characteristic involves the presence of porosity in the weld cross section. Both minor and gross porosity are present in these cross sections. Since each cross section represents only a single location along the length of each weld, porosity is therefore assumed to be present in all the welds.

A summary of the weld measurements made on each weld is given in Table 8. In addition to these measurements, the weld aspect ratio, which is defined as the depth to width ratio, is also listed. Plots comparing each of these measurements with the power impinging on the sample surface are shown in Figures 20(a-d) for each travel speed. With increasing power, both the weld width and depth increase, albeit at different rates. For the two travel speeds investigated, the speed has a minimal effect on the weld depth. On the other hand, a decrease in the travel speed produces a significantly wider weld, as is shown in Figure 20(a).

The effects of changes in the input power on the weld aspect (depth/width) ratio are shown in Figure 20(c). With increasing power, the aspect ratio increases, indicating that the weld cross section is becoming deeper and narrower and is taking on a more typical keyhole shape. At the higher travel speed (19.1 mm/sec), the aspect ratio increases with increasing machine power settings, resulting in a deep and narrow weld at a power setting of 2200 W. On the other hand, the measured aspect ratios at the slower travel speed (12.7 mm/sec) maintain a constant value or even decrease at power levels above approximately 900 W and fall well below those values measured at the faster travel speed. Measurements of the melted area of each weld cross section are plotted in Figure 20(d) as a function of the measured input power. In this plot, the cross sectional area measured at each travel speed increases in a generally linear manner with increasing power. Measurements of the keyhole width and reinforcement height have also been made on each weld cross section. The effects of changes in power on these measurements are shown in Figures 21(a&b). Whereas the keyhole width displays a definite increasing trend with increasing power, the trend in the reinforcement height is not as clear, although, it does show an increase with increasing power for both travel speeds.

Travel Speed Variation Studies

In order to better define the effects of travel speed on the resulting weld characteristics, a series of welds have been made at the maximum power level of the LLNL laser at travel speeds between 6.4 and 16.9 mm/sec. These welds provide the best indication of the maximum depth of which this laser system is capable in 304L austenitic stainless steels. Micrographs of weld cross sections taken at travel speeds of 16.9, 10.6, 8.5 and 4.2 mm/sec are shown in Figures 22(a-d), respectively. Each cross section displays a shape consistent with a keyhole mode of welding and significant porosity. In addition, with the decrease in travel speed in each micrograph, changes

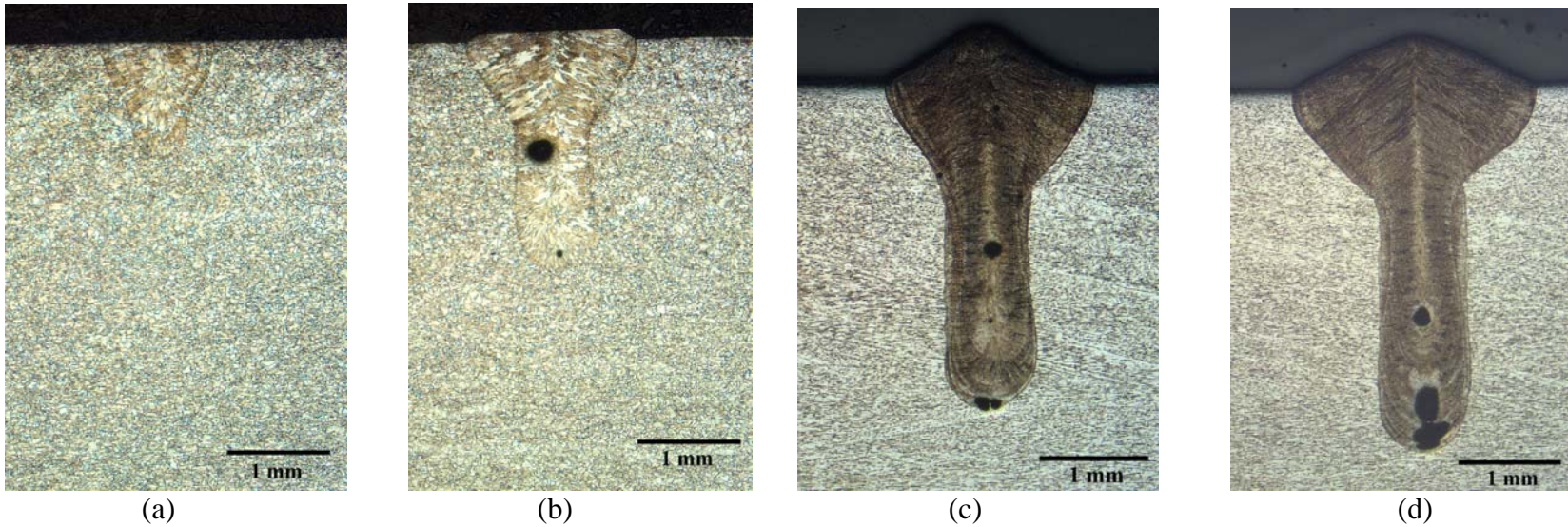


Figure 18(a-d). Micrographs of weld cross sections made in 304L stainless steel samples at machine power settings of (a) 500 W, (b) 1000 W, (c) 1500 W, and (d) 2000 W at a travel speed of 19.1 mm/sec. These welds have been made on the LLNL laser system.

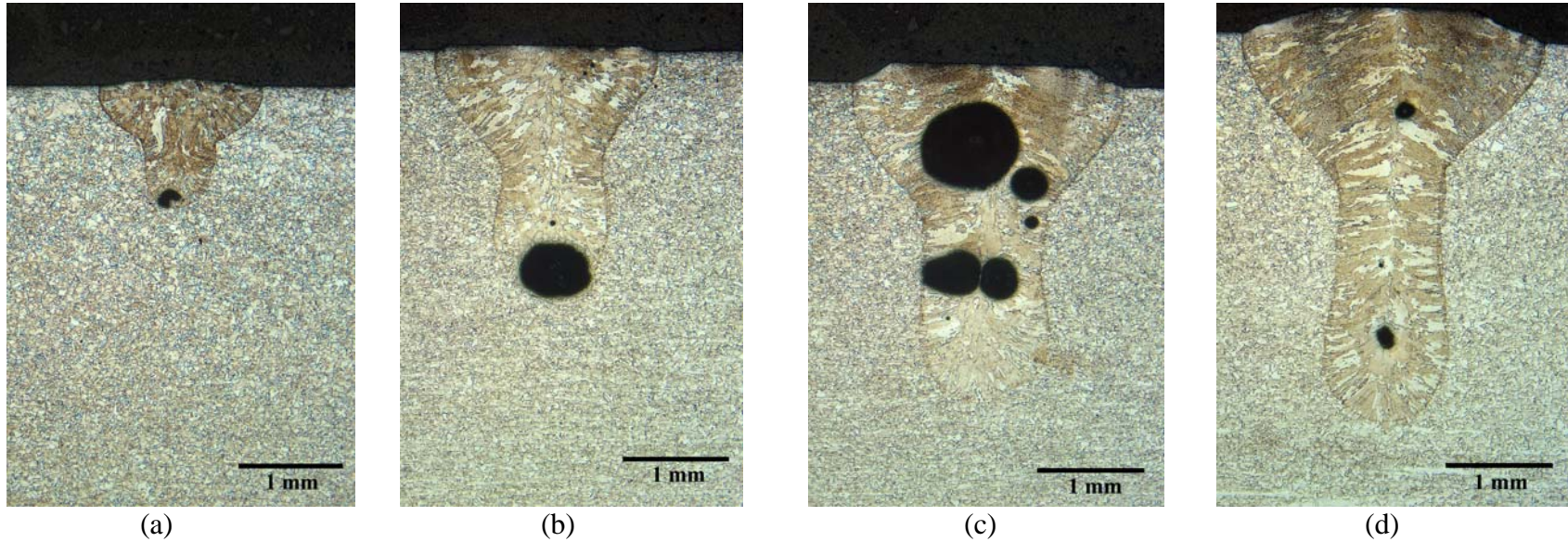


Figure 19(a-d). Micrographs of weld cross sections for welds made in 304L stainless steel at machine power settings of (a) 500 W, (b) 1000 W, (c) 1500 W, and (d) 2000 W at a travel speed of 12.7 mm/sec. These welds have been made on the LLNL laser system.

Table 8. Summary of weld measurements taken during power variation studies in 304L stainless steel samples using the LLNL welder.

<u>Power*</u> <u>(Watts)</u>	<u>Energy</u> <u>Input</u> <u>(J/mm)</u>	<u>Weld</u> <u>Width</u> <u>(mm)</u>	<u>Weld Depth</u> <u>(mm)</u>	<u>Aspect Ratio</u> <u>(Depth/Width)</u>	<u>Keyhole</u> <u>Width</u> <u>(mm)</u>	<u>Weld</u> <u>Reinforcement</u> <u>Height (mm)</u>	<u>Melted</u> <u>Area</u> <u>(mm²)</u>
<i>Travel Speed = 19.1 mm/sec</i>							
179	9.4	0.53	0.17	0.33	N/A	0	0.07
390	20.5	1.11	1.10	0.99	0.54	0	0.76
580	30.4	1.30	1.65	1.27	0.63	0.05	1.40
773	50.6	1.66	2.22	1.34	0.78	0.12	1.92
936	49.1	1.79	2.50	1.40	0.85	0.17	2.77
1120	58.8	1.79	2.79	1.56	0.76	0.49	2.96
1312	68.9	1.93	3.21	1.67	0.77	0.53	3.77
1494	78.4	2.22	3.32	1.50	0.79	0.49	4.23
1630	85.6	2.19	3.33	1.52	0.34	0.74	4.15
<i>Travel Speed = 12.7 mm/sec</i>							
179	14.1	0.62	0.16	0.27	N/A	0	0.09
390	30.7	1.57	1.17	0.74	0.65	0.08	1.18
580	45.7	1.98	1.69	0.85	0.89	0	2.03
773	60.9	2.10	2.33	1.11	1.08	0.06	2.92
936	73.7	2.10	2.59	1.23	1.10	0.15	4.10
1120	88.2	2.53	2.93	1.16	1.20	0.20	4.49
1312	103.3	2.99	3.23	1.08	1.30	0.07	5.01
1494	117.6	2.87	3.63	1.27	1.15	0.30	5.45
1630	128.3	3.30	3.65	1.11	1.43	0.47	6.95

*Actual power delivered to the part.

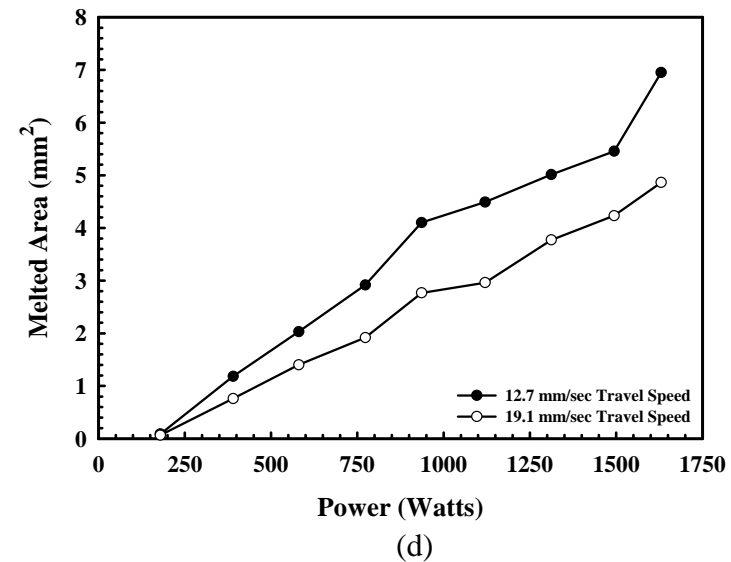
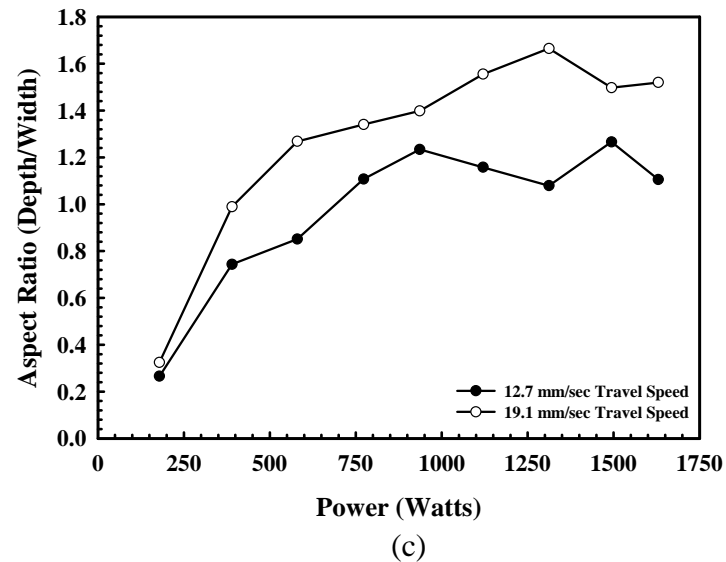
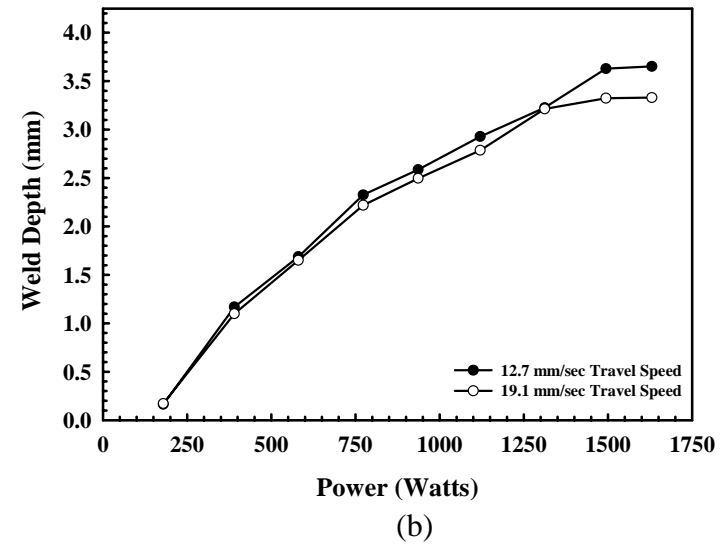
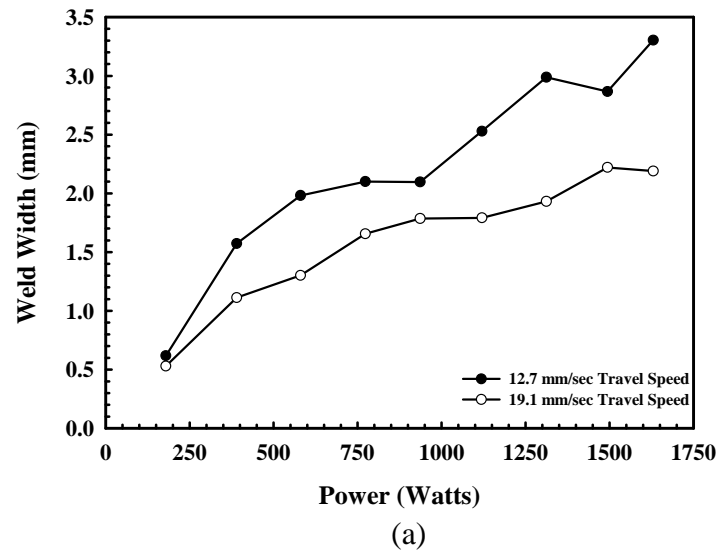


Figure 20(a-d). Plots showing variations in the (a) weld width, (b) weld depth, (c) aspect ratio (depth/width), and (d) melted area with changes in the machine output power setting for travel speeds of 19.1 mm/sec and 12.7 mm/sec in 304L stainless steel welds using the LLNL welder.

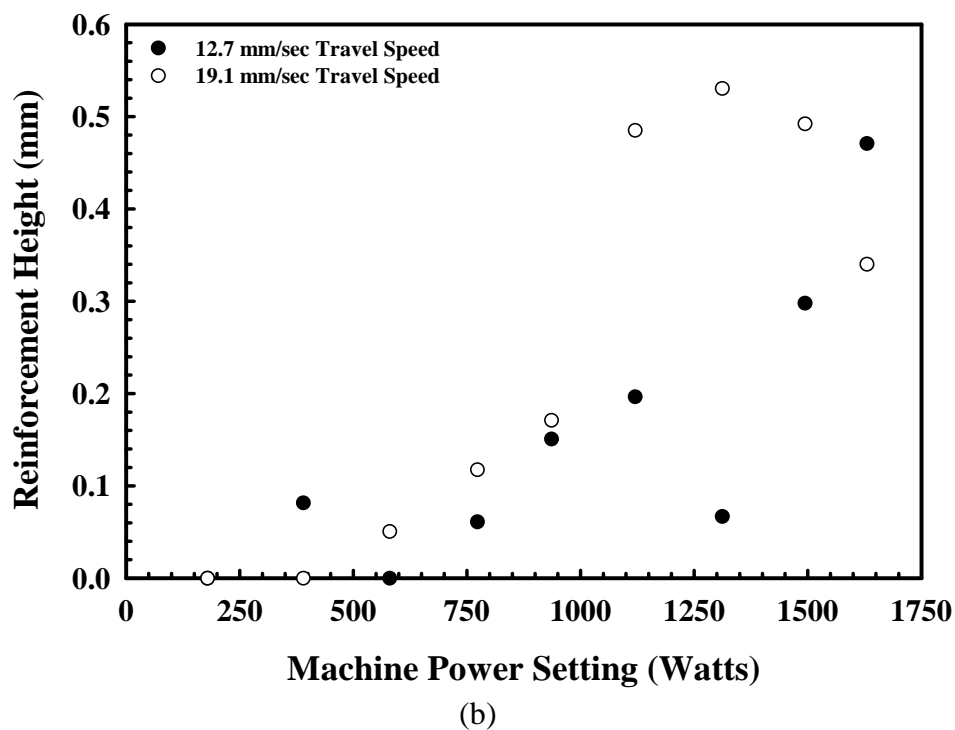
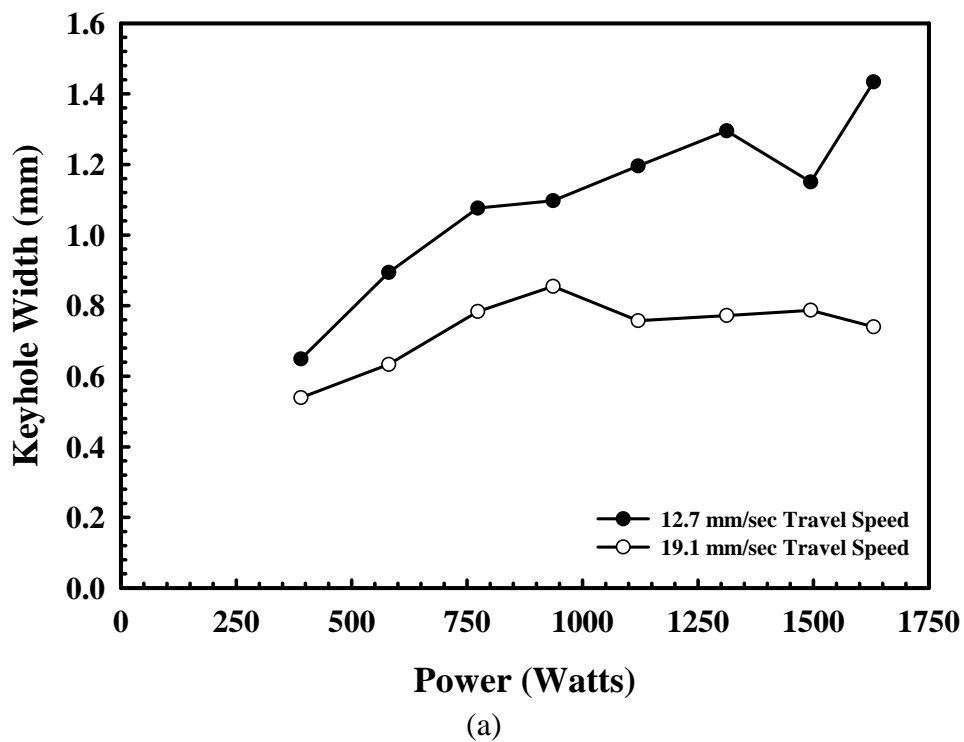


Figure 21(a&b). Plots showing variations in the (a) keyhole width and (b) overfill height with changes in the machine output power setting for travel speeds of 19.1 mm/sec and 12.7 mm/sec in 304L stainless steel welds made using the LLNL welder.

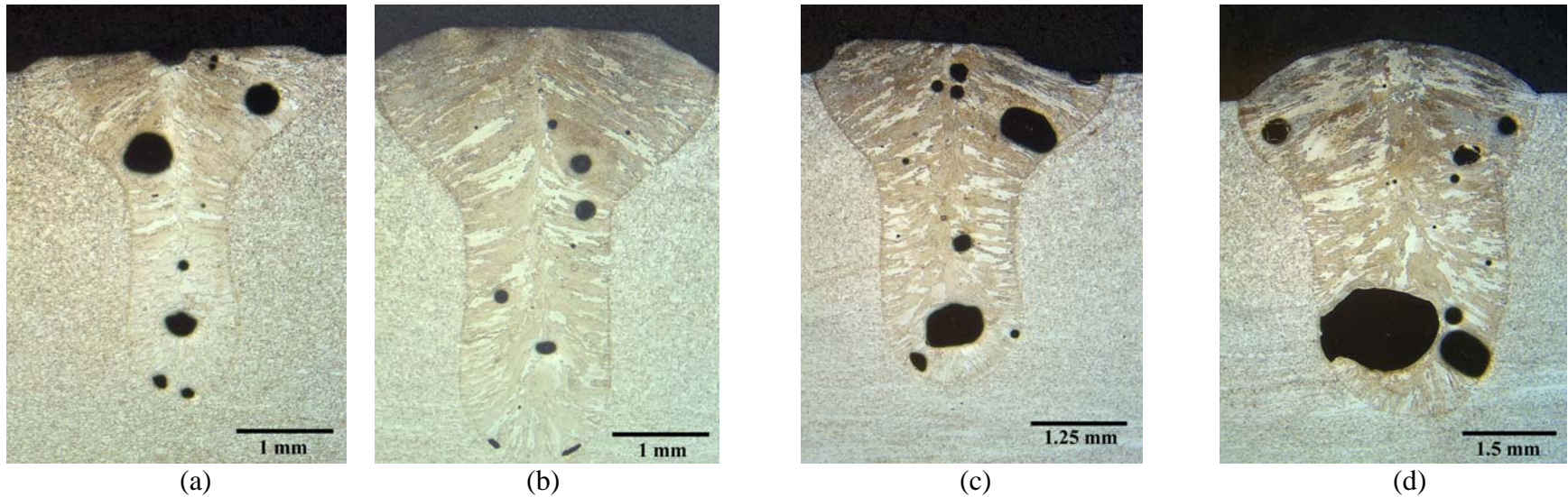


Figure 22(a-d). Micrographs of weld cross sections in 304L stainless steel welds made at travel speeds of (a) 16.9 mm/sec, (b) 10.6 mm/sec, (c) 8.5 mm/sec, and (d) 4.2 mm/sec at a constant machine power setting of 2200 W. Note changes in magnifications of micrographs in (c) and (d). These welds have been made on the LLNL laser system.

in the size and shape of the weld pool become more evident, especially in the region where the keyhole width is measured.

Measurements made on each of these welds are summarized in Table 9. The values listed in this table, including the weld width, depth, aspect ratio, and total melted area, are also plotted in Figures 23(a-d), respectively, as a function of travel speed. In general, the weld width and depth decrease with increasing travel speed, as shown in Figures 23(a) and 23(b). The largest weld width (4.79 mm) and depth (5.13 mm) are observed at the lowest travel speed (6.4 mm/sec). These changing dimensions result in a nearly constant aspect ratio, in the vicinity of 1.0, across the range of travel speeds (Figure 23(c)). The effect of changes in travel speed on the melted area of each weld shows a consistent trend. As shown in Figure 23(d), the melted area consistently decreases with an increase in travel speed. Such behavior is expected since the melted area provides a more general description of the weld pool than the weld width and depth, which are both affected by changes in the characteristics of the keyhole with changing weld parameters. The rate of change in the melted area is greatest at the lower travel speeds and becomes more constant at the higher travel speeds analyzed here.

The effects of changing travel speed on the keyhole width and reinforcement height are shown in Figures 24(a&b), respectively. In these figures, the keyhole width and reinforcement height decrease with increasing travel speeds, albeit with differing trends. This behavior is expected, given the general connection between increasing keyhole width and decreasing travel speed observed in the power variation studies and the rather significant porosity observed in the weld cross sections produced at the lower travel speeds.

Effects of Energy Input per Unit Length of Weld

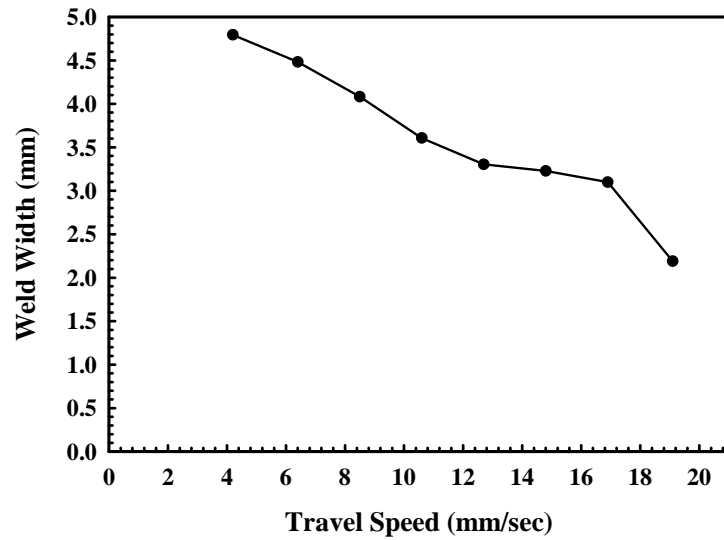
Comparisons between the measured weld width, depth, aspect ratio, and melted area are plotted in Figures 25(a-d) as a function of energy input per unit length of weld. In these plots, the results from both the power variation and travel speed studies can be directly compared. A preliminary glance at these plots shows that there can be little difference in the measurements taken from the different studies. For example, the results from the two power variation studies show little difference and fall along the same trend line, as shown in Figure 25(a). This trend line continues at the higher energy inputs corresponding with the results from the travel speed variation study. Taken together, the three studies produce a single trend in weld width, which is defined by a general increase in value with increasing energy input.

In the case of the weld depth, which is shown in Figure 25(b), differences in the power variation studies are observed at the lower energy inputs. The power variation study performed at a travel speed of 19.1 mm/sec produces slightly higher weld depths than those measured at a travel speed of 12.7 mm/sec, for a given energy input. As the energy input per unit length of weld is increased, and the weld travel speed decreases, the weld depths continue to increase, albeit at a lower rate.

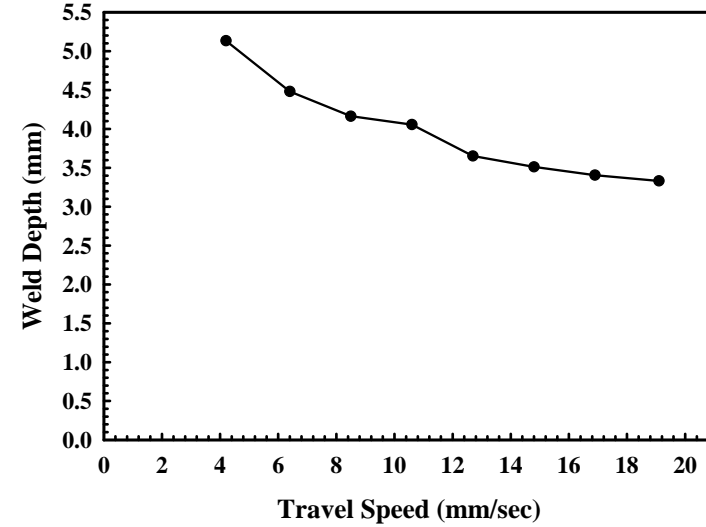
This difference in weld depth at lower energy inputs is translated into welds with higher aspect ratios as a function of energy input, as shown in Figure 25(c). In fact, the aspect ratios for the higher travel speed power variation study are significantly larger than those measured at the lower travel speeds. As shown in the plot, there appears to be a spike in the depth/width ratio at energy inputs of approximately 85 J/mm. This spike in values indicates that there is possibly a change in the keyhole characteristics or mode of welding at this energy input.

Table 9. Summary of weld measurements taken during travel speed variation studies made in 304L stainless steel at the maximum power output setting (1630 W delivered to the part).

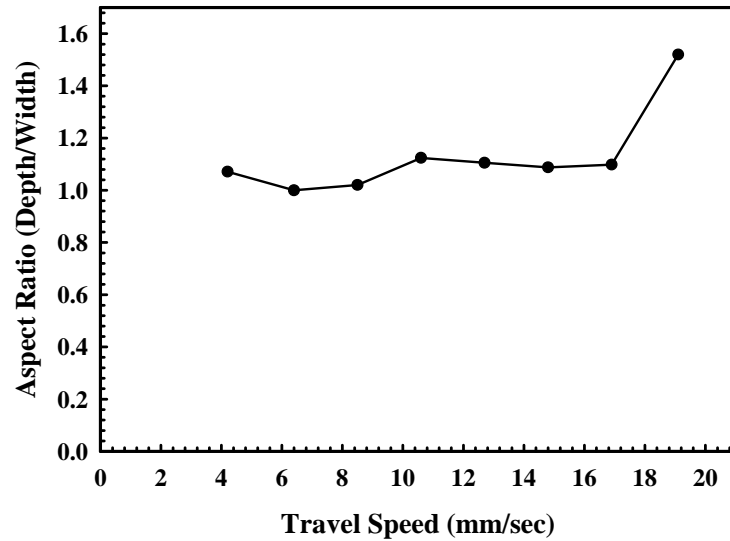
<u>Travel Speed</u> <u>(mm/sec)</u>	<u>Energy</u> <u>Input</u> <u>(J/mm)</u>	<u>Weld</u> <u>Width</u> <u>(mm)</u>	<u>Weld</u> <u>Depth</u> <u>(mm)</u>	<u>Aspect Ratio</u> <u>(Depth/Width)</u>	<u>Keyhole</u> <u>Width</u> <u>(mm)</u>	<u>Weld</u> <u>Reinforcement</u> <u>Height (mm)</u>	<u>Melted</u> <u>Area</u> <u>(mm²)</u>
19.1 (45 in/min)	85.6	2.19	3.33	1.52	0.34	0.74	4.15
16.9 (40 in/min)	96.3	3.10	3.41	1.10	1.05	0.15	5.26
14.8 (35 in/min)	110.0	3.23	3.51	1.09	1.16	0.34	6.25
12.7 (30 in/min)	128.3	3.30	3.65	1.11	1.43	0.47	6.95
10.6 (25 in/min)	154.0	3.61	4.06	1.12	1.53	0.45	9.15
8.5 (20 in/min)	192.5	4.08	4.16	1.02	1.88	0.41	10.74
6.4 (15 in/min)	256.7	4.48	4.48	1.00	2.28	0.45	13.56
4.2 (10 in/min)	385.0	4.79	5.13	1.07	3.11	0.92	20.96



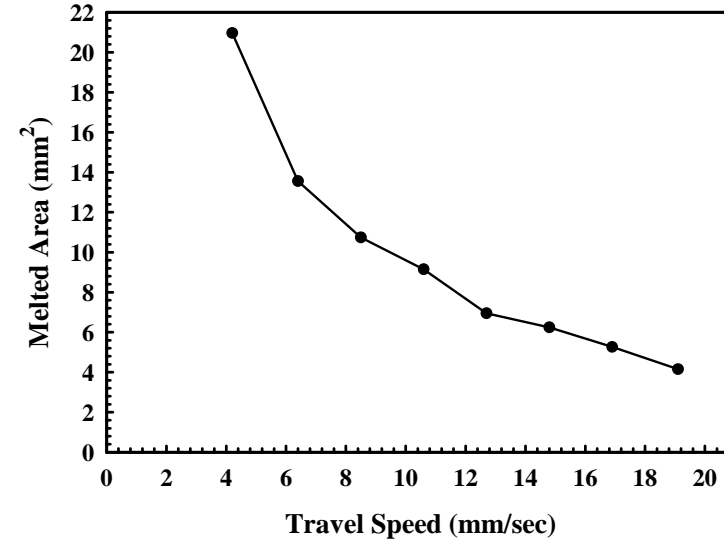
(a)



(b)

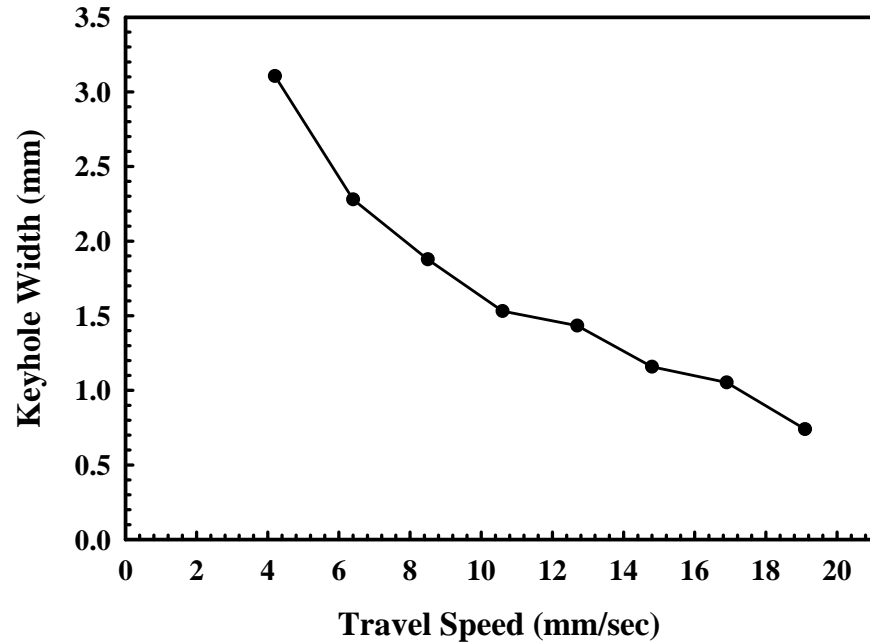


(c)

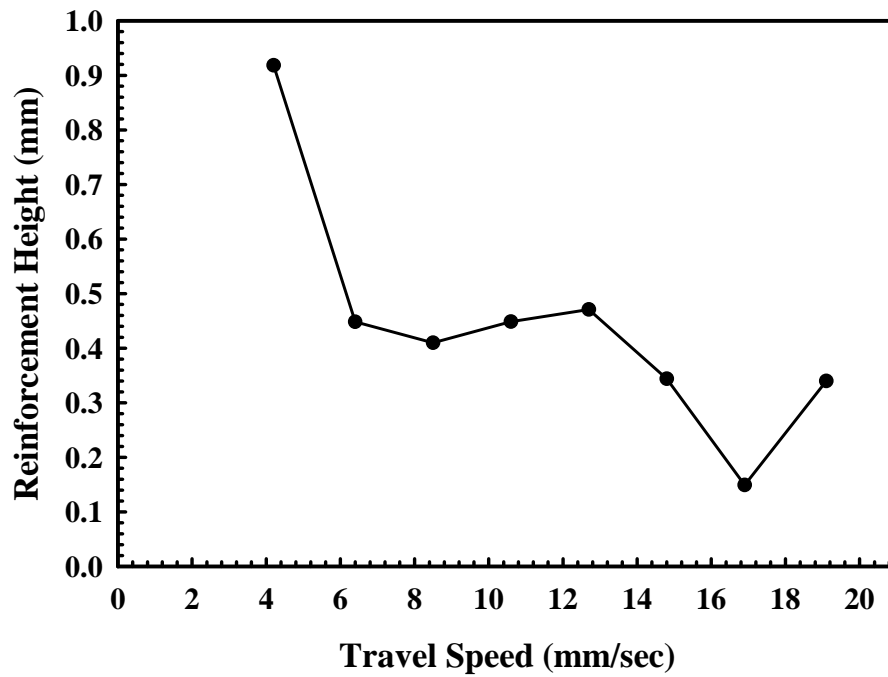


(d)

Figure 23(a-d). Plots showing variations in the (a) weld width, (b) weld depth, (c) aspect ratio, and (d) melted area with changes in the travel speed for a maximum power of 1630 W in 304L stainless steel welds made using the LLNL welder.

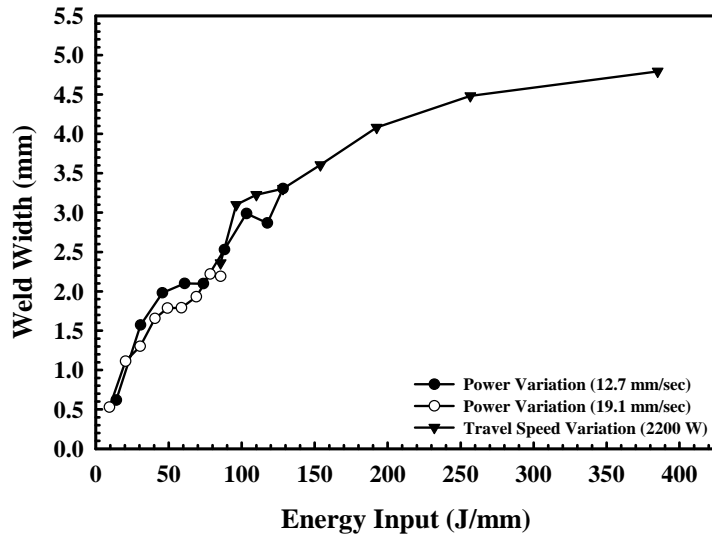


(a)

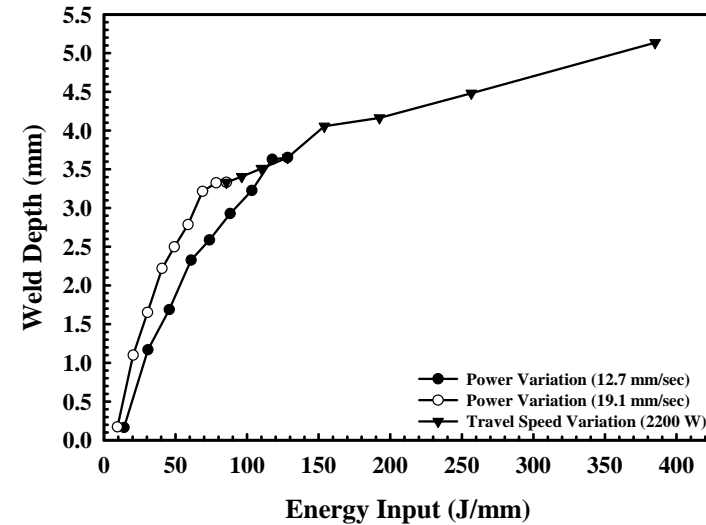


(b)

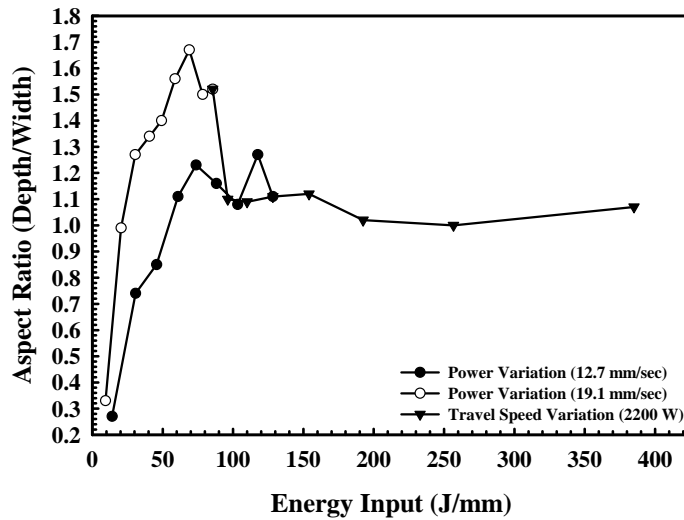
Figure 24(a&b). Plots showing variations in the (a) keyhole width and (b) overfill height with changes in travel speed at a machine output power setting of 2200 W in 304L stainless steel welds made using the LLNL welder.



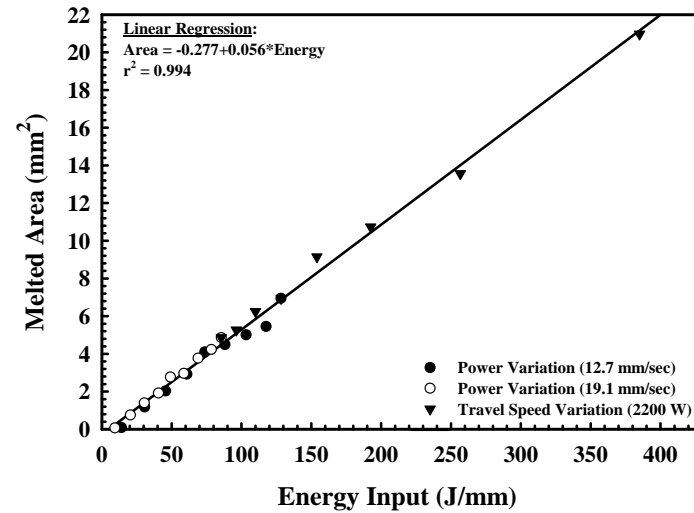
(a)



(b)



(c)



(d)

Figure 25(a-d). Plots showing variations in the (a) weld width, (b) weld depth, (c) aspect ratio, and (d) melted area of each weld cross section as a function of the energy input for the two power variation studies and the travel speed variation study performed on 304L stainless steel samples using the LLNL welder.

Unlike the other weld measurements, the melted areas, shown in Figure 25(d), display a consistent linear trend over the entire range of energy inputs. A linear regression analysis of the data in Figure 25(d) shows a slope of 0.056, which corresponds with the rate of change of the melted area as a function of the energy input per unit length of weld. This behavior is the result of the melted area not being affected by the mode of laser welding but being strictly a function of the amount of power from the laser beam interacting with the sample surface.

21-6-9 Austenitic Stainless Steel

Power Variation Studies

The effects of changes in the machine power settings from 250 W to 2200 W on the resulting weld pool cross-section shape and size are examined at travel speeds of 12.7 mm/sec, 19.1 mm/sec, and 25.4 mm/sec. Micrographs showing the weld cross sections for machine power settings between 500 and 2000 W for each travel speed are shown in Figures 26 through 28. Each of the weld cross sections shown in these figures displays a shape typical of keyhole mode laser welding. On the other hand, at a machine power setting of 250 W at each travel speed, as shown in Figures 29(a-c), the resulting weld pool cross sections display a shape more typical of conduction mode laser welding. These differences in the welding mode at machine power settings of 250 W and 500 W indicate that the transition from conduction mode to keyhole mode welding falls somewhere in between.

Unlike the significant porosity present in the 304L laser welds, these 21-6-9 stainless steel welds display little to no porosity. The conditions leading to keyhole instability are at least partially mitigated in the 21-6-9 stainless steel by the high concentration of manganese in the alloy. Unlike the 304L stainless steel, which contains only 1.71 wt.% Mn, the 21-6-9 stainless steel used in this study contains 9.14 wt.%. Manganese plays an important role in stabilizing the keyhole because of its high vapor pressure in comparison with the other alloying elements (165.1 Pa vs. 2.3 Pa for pure iron at their respective melting points, 1236°C for Mn and 1536°C for Fe).⁸ Even though this value is for a pure metal, the effects in this alloy system are similar. With such a high vapor pressure, manganese evaporates very easily, making it much easier for the keyhole to form and, in turn, be sustained during welding. As a result, the deep penetrating and porosity-free welds observed in Figures 26 through 28 are produced.

A summary of the weld measurements for the three power variation studies is given in Table 10. In addition to the width, depth, and area measurements, the aspect ratio of each weld, which is defined as the depth to width ratio, is also listed. In the welds analyzed here, the measured aspect ratios far exceed unity, easily meeting the characteristics for keyhole mode welding. Plots comparing these measurements with the power impinging on the sample surface are shown in Figures 30(a-d) for each travel speed. With increasing power, both the weld width and depth increase, albeit at different rates. For the travel speeds investigated, the slowest travel speed (12.7 mm/sec) produces both the widest and deepest weld pools with the highest melted areas. This characteristic is consistent across all of the power inputs, from 179 W to 1630 W. Even though the travel speed has a marked effect in the primary weld pool measurements, the changes in travel speed appear to have much less of an effect on the weld aspect ratio. As shown in

⁸ *Smithells Metals Reference Book*, Seventh Edition, ed. by E.A. Brandes and G.B. Brook, (Butterworth Heinemann, Oxford, 1998)

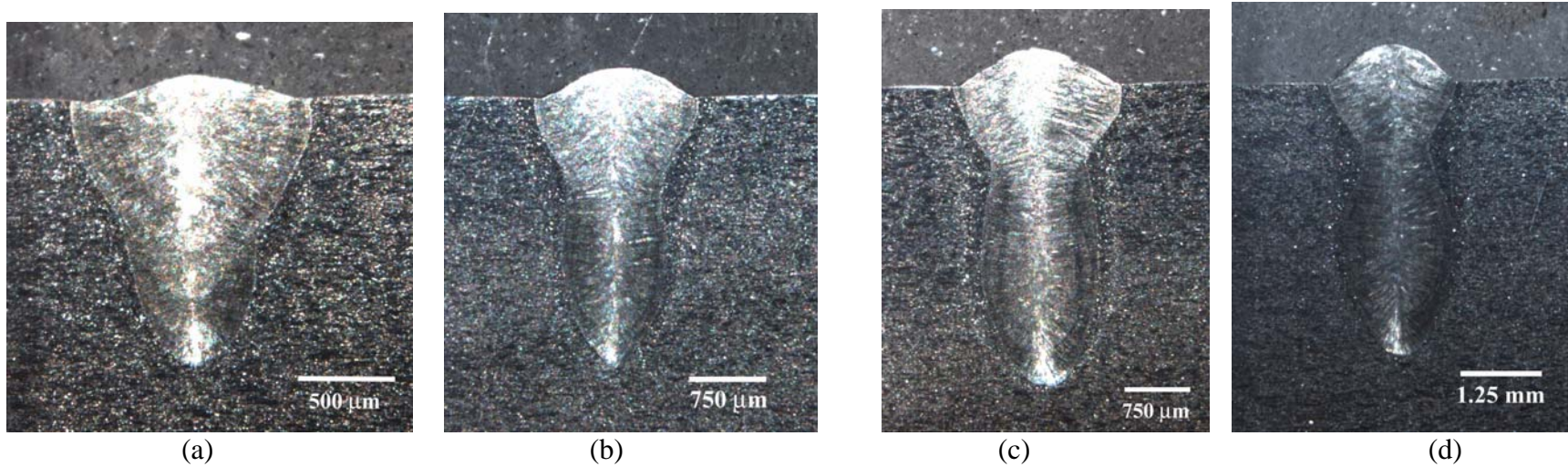


Figure 26(a-d). Micrographs of weld cross sections in 21-6-9 austenitic stainless steel samples made at machine power settings of (a) 500 W, (b) 1000 W, (c) 1500 W, and (d) 2000 W at a constant travel speed of 12.7 mm/sec using the LLNL welder. Note the different magnifications in each figure.

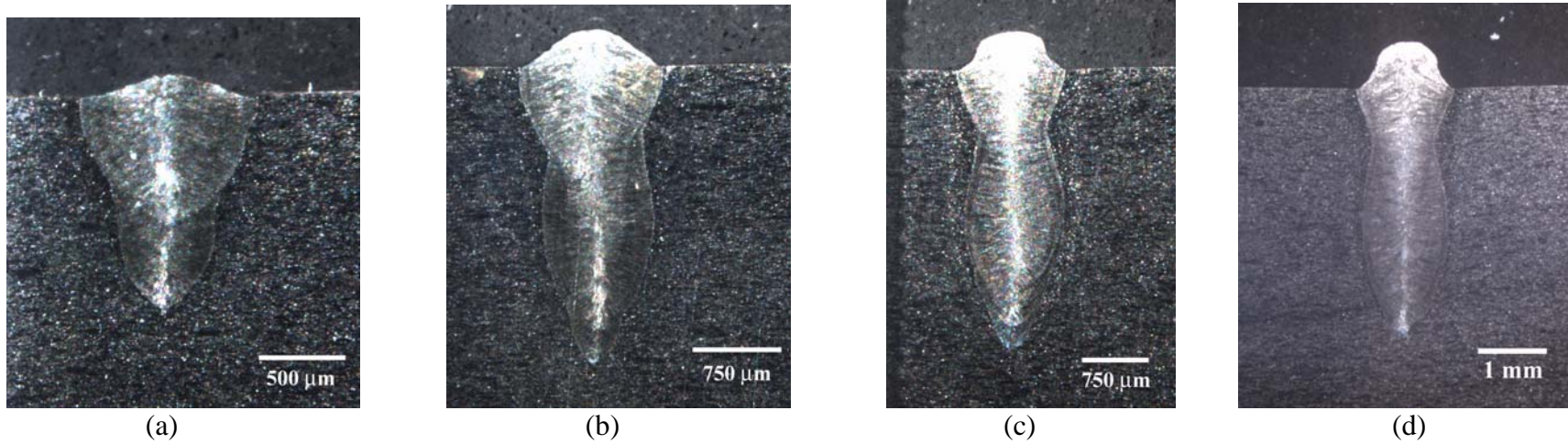


Figure 27(a-d). Micrographs of weld cross sections in 21-6-9 austenitic stainless steel samples made at machine power settings of (a) 500 W, (b) 1000 W, (c) 1500 W, and (d) 2000 W and a constant travel speed of 19.7 mm/sec using the LLNL welder.

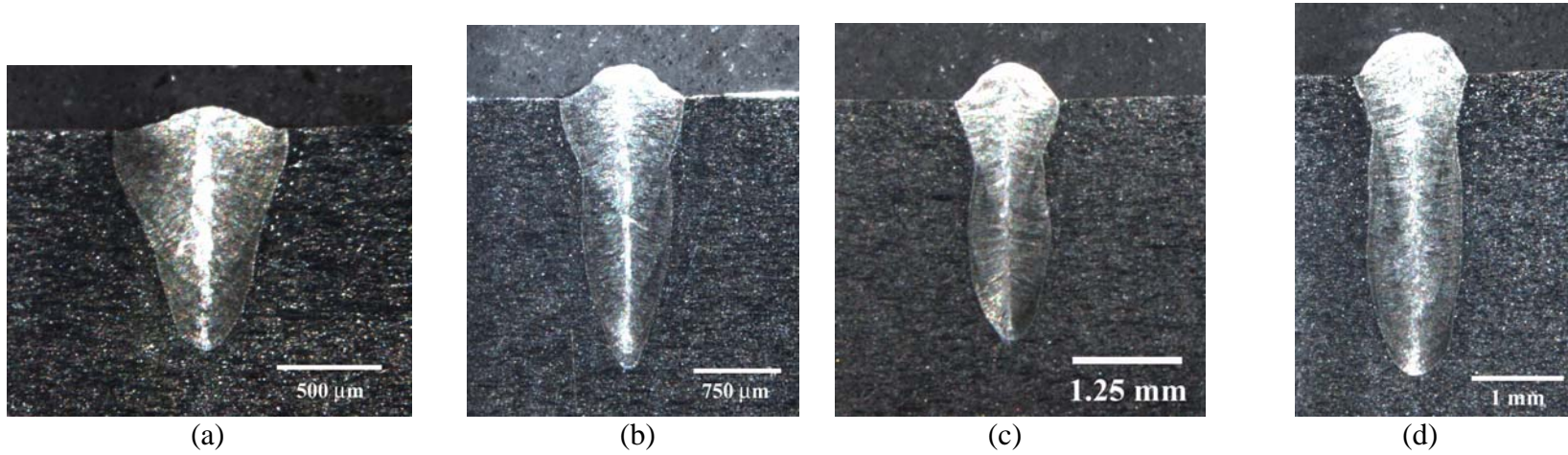


Figure 28(a-d). Micrographs of weld cross sections in 21-6-9 austenitic stainless steel samples made at machine power settings of (a) 500 W, (b) 1000 W, (c) 1500 W, and (d) 2000 W and a constant travel speed of 25.4 mm/sec using the LLNL laser system.

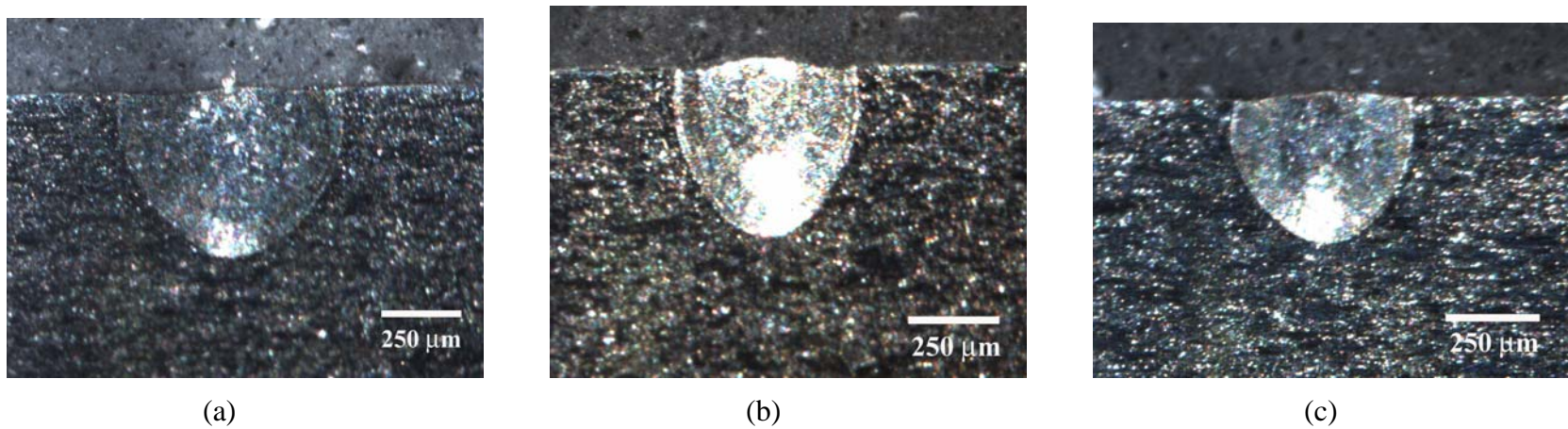


Figure 29(a-c). Micrographs of weld cross sections in 21-6-9 austenitic stainless steel samples made at a machine power setting of 250 W and travel speeds of (a) 12.7 mm/sec, (b) 19.1 mm/sec, and (c) 25.4 mm/sec using the LLNL laser system. Note the differing magnifications of each micrograph.

Table 10. Summary of measurements made on 21-6-9 austenitic stainless steel weld samples using the LLNL welding system with variations in the weld input power at travel speeds of 12.7 mm/sec, 19.1 mm/sec, and 25.4 mm/sec.

<u>Power*</u> <u>(Watts)</u>	<u>Energy Input</u> <u>(J/mm)</u>	<u>Weld Width</u> <u>(mm)</u>	<u>Weld Depth</u> <u>(mm)</u>	<u>Aspect Ratio</u> <u>(Depth/Width)</u>	<u>Keyhole Width</u> <u>(mm)</u>	<u>Reinforcement</u> <u>Height (mm)</u>	<u>Melted Area</u> <u>(mm²)</u>
<i>Travel Speed = 25.4 mm/sec</i>							
179	7.1	0.488	0.387	0.794	----	----	0.164
390	15.4	0.858	1.093	1.274	0.508	0.125	0.684
580	22.8	1.008	1.707	1.693	0.590	0.212	1.195
773	30.4	1.094	2.360	2.157	0.770	0.313	1.873
936	36.9	1.204	2.335	1.940	0.897	0.347	2.181
1120	44.1	1.220	2.806	2.301	0.970	0.461	2.974
1312	51.7	1.244	2.966	2.385	1.047	0.416	3.178
1494	58.8	1.243	3.236	2.604	1.010	0.459	3.526
1630	64.2	1.226	3.361	2.740	1.100	0.592	4.032
<i>Travel Speed = 19.1mm/sec</i>							
179	9.4	0.486	0.444	0.913	----	0.033	0.189
390	20.5	1.003	1.210	1.206	0.539	0.109	0.884
580	30.4	1.282	1.997	1.558	0.698	0.161	1.588
773	50.6	1.225	2.496	2.038	0.924	0.321	2.259
936	49.1	1.252	2.699	2.156	1.022	0.424	2.796
1120	58.8	1.253	3.135	2.502	1.131	0.447	3.127
1312	68.9	1.319	3.478	2.637	1.164	0.485	3.905
1494	78.4	1.496	3.665	2.450	1.293	0.698	4.827
1630	85.6	1.509	3.982	2.639	1.337	0.650	5.562
<i>Travel Speed = 12.7mm/sec</i>							
179	14.1	0.673	0.498	0.740	----	----	0.281
390	30.7	1.311	1.453	1.109	0.680	0.136	1.300
580	45.7	1.734	2.178	1.256	0.822	0.184	2.274
773	60.9	1.662	2.782	1.674	1.096	0.314	3.225
936	73.7	1.833	3.187	1.739	1.143	0.400	4.126
1120	88.2	1.987	3.532	1.778	1.398	0.424	5.162
1312	103.3	1.964	4.386	2.234	1.536	0.472	6.520
1494**	117.6	1.965	4.182	2.128	1.713	0.579	6.709
1630**	128.3	1.975	4.720	2.391	1.617	0.561	7.379

*Actual power delivered to the part.

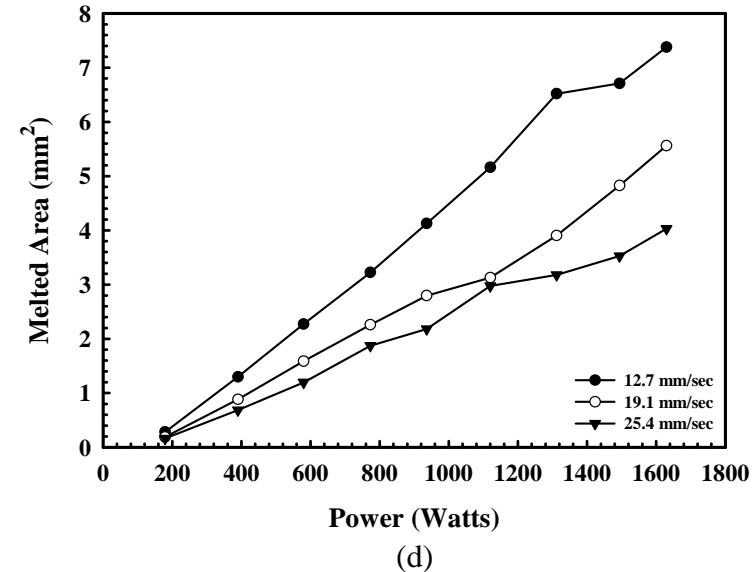
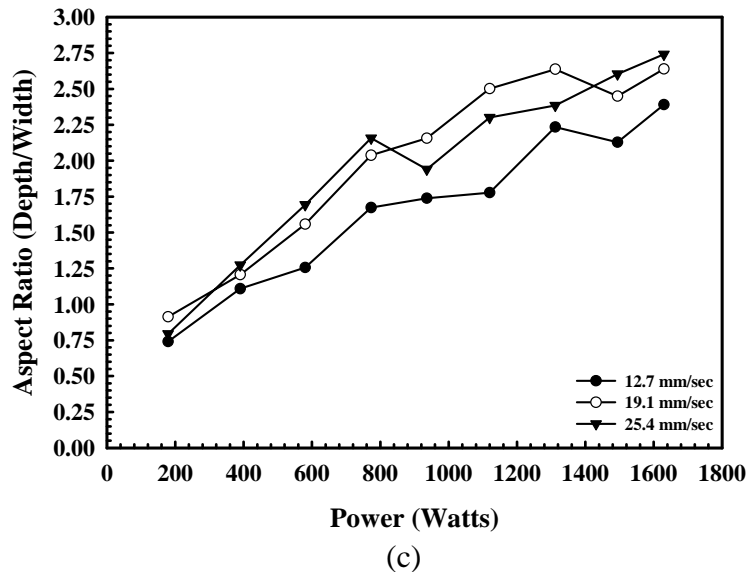
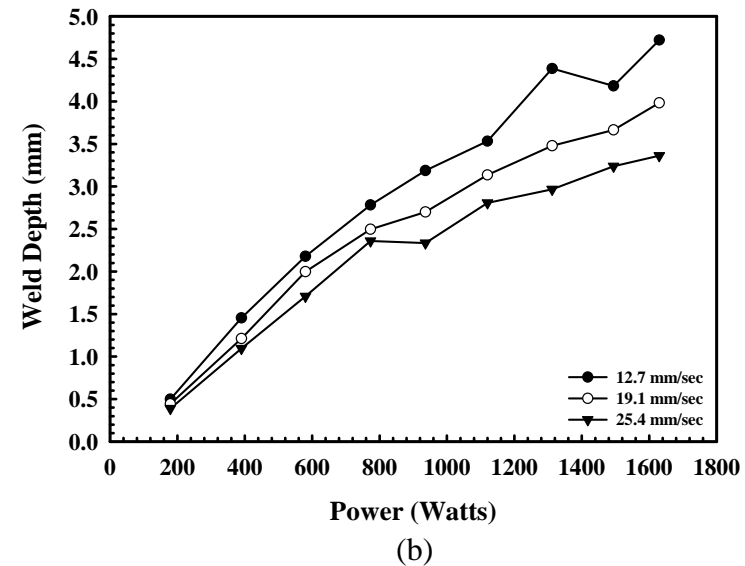
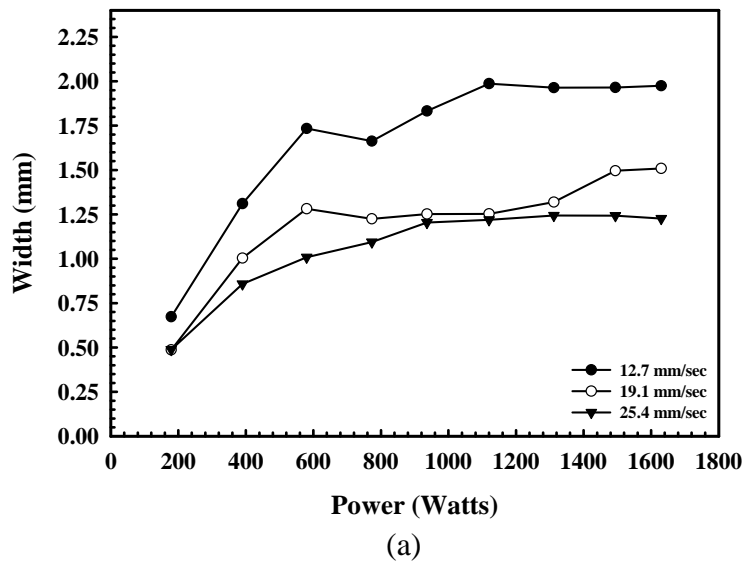


Figure 30(a-d). Plots showing variations in the weld (a) width, (b) depth, (c) aspect ratio (depth/width), and (d) melted area measured in 21-6-9 austenitic stainless steel samples with changes in the input power at travel speeds of 12.7 mm/sec, 19.1 mm/sec, and 25.4 mm/sec on the LLNL laser system.

Figure 30(c), the weld aspect ratios for each travel speed increase with increasing power. The slowest travel speed displays the smallest aspect ratio, while the two more rapid travel speeds show little difference in values. Overall, though, the aspect ratios for the three travel speeds display values greater than 2.0 at the highest input powers. Values of this magnitude are much higher than those measured in the other materials. The effects of changes in power on the keyhole width and the reinforcement height are shown in Figures 31(a&b) for the three travel speeds investigated here. In general, both values increase with increasing power input for each travel speed. Whereas the keyhole width shows a distinct relation with travel speed, in which the slower travel speeds produce wider keyholes, the weld reinforcement heights are similar for each travel speed.

Travel Speed Variation Studies

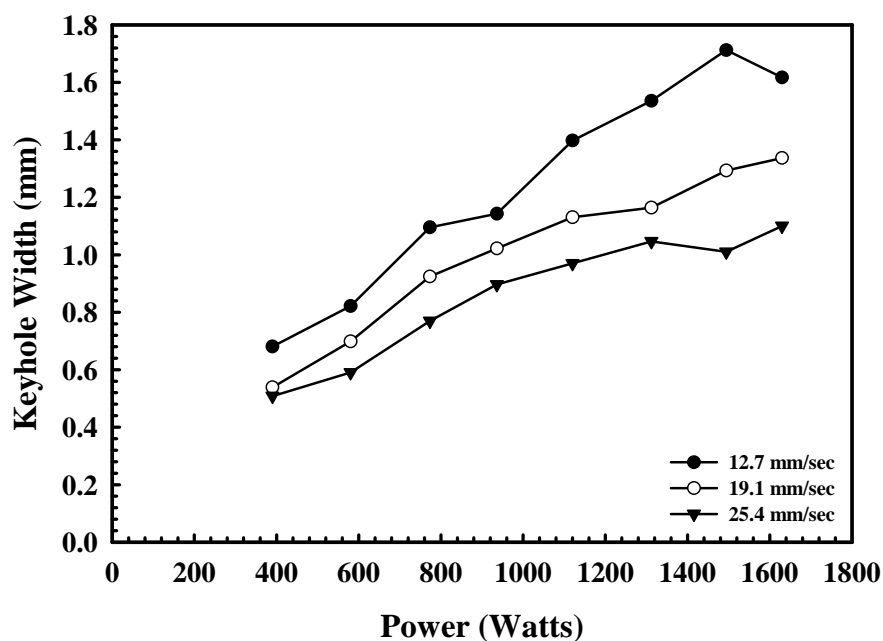
Welds are also made at a constant input power of 1630 W with travel speeds varying between 6.4 and 25.4 mm/sec. Micrographs of weld cross sections taken at travel speeds of 21.2, 14.8, 8.5 and 6.4 mm/sec are shown in Figures 32(a-d), respectively. Each cross section displays a shape consistent with a keyhole mode of welding. In addition, the size and shape of each weld, especially the keyhole width, change with the decrease in travel speed.

The measurements made on these weld cross sections are summarized in Table 11, while the weld width, depth, aspect ratio, and total melted area are plotted in Figures 33(a-d), respectively, as a function of the travel speed. In general, the weld width, depth, and melted area decrease, albeit at different rates, with increasing travel speed, as shown in Figures 33(a), 33(b), and 33(d), respectively. In each case, the largest weld width (3.26 mm), depth (5.42 mm), and melted area (12.71 mm^2) are observed at the lowest travel speed (6.4 mm/sec). On the other hand, the aspect ratios display the highest values at the highest travel speeds. For example, a comparison between the highest and lowest travel speeds studied here shows that an aspect ratio of approximately 2.8 is achieved at a travel speed of 25.4 mm/sec, while one of only 1.7 is achieved at a travel speed of 6.4 mm/sec.

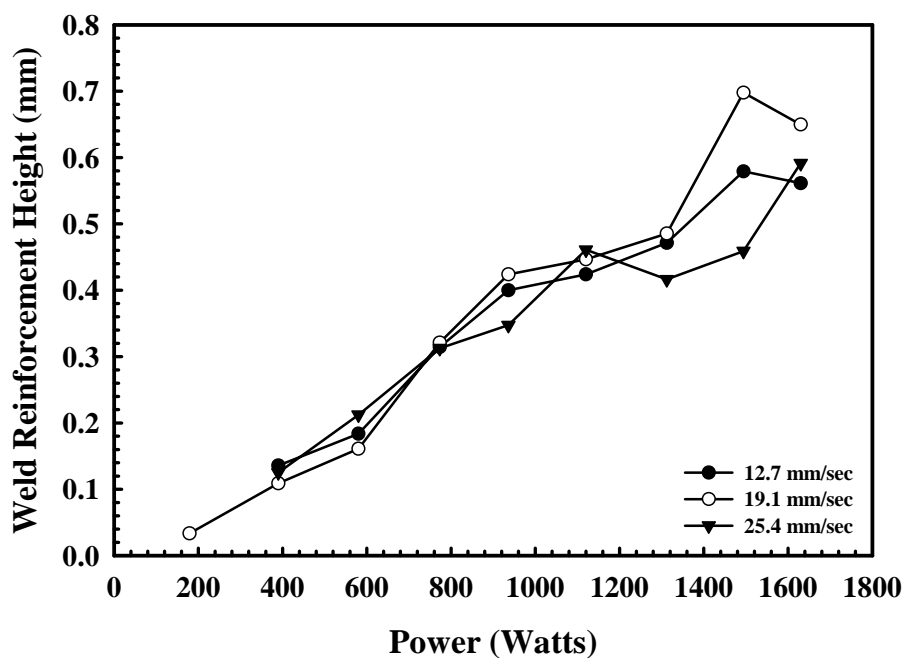
The effects of changing travel speed on the keyhole width and reinforcement height are shown in Figures 34(a&b), respectively. In these figures, the keyhole width and reinforcement height show differing trends. For example, the keyhole width, shown in Figure 34(a) decreases with increasing travel speed. This behavior is consistent with that observed in the power variation studies, where the keyhole widths produced at the slower travel speeds are the largest. On the other hand, the reinforcement height remains constant over the range of travel speeds, matching that behavior observed in the power variation studies, where the different travel speeds displayed a uniform increase in weld reinforcement height with increasing power.

Effects of Energy Input per Unit Length of Weld

Comparisons between the measured weld width, depth, aspect ratio, and melted area for the results from both the power variation and travel speed studies are plotted in Figures 35(a-d) as a function of energy input per unit length of weld. These measurements generally show increasing values with increasing energy inputs. On the other hand, the rates of change for the different power variation and travel speed studies are different. Changes in the weld width as a function of energy input are shown in Figure 35(a). In this figure, the widths measured in the power



(a)



(b)

Figure 31(a&b). Plots showing variations in the (a) keyhole width and (b) weld reinforcement height in 21-6-9 austenitic stainless steel welds made over a range of input power settings and travel speeds of 12.7 mm/sec, 19.1 mm/sec, and 25.4 mm/sec using the LLNL laser system.

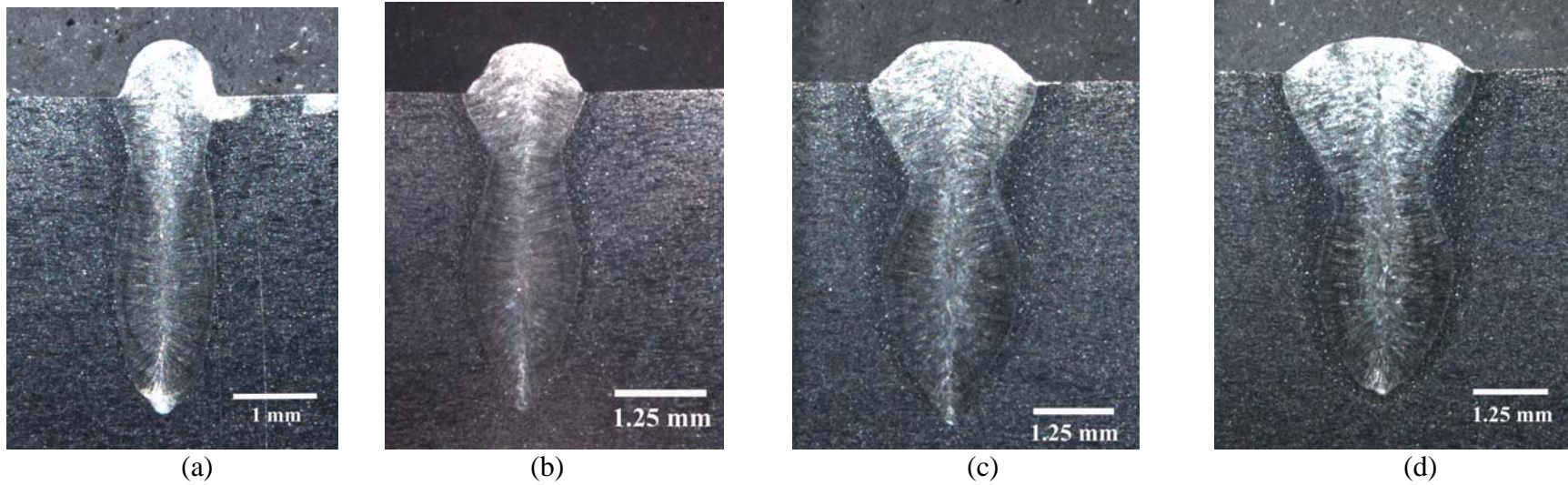
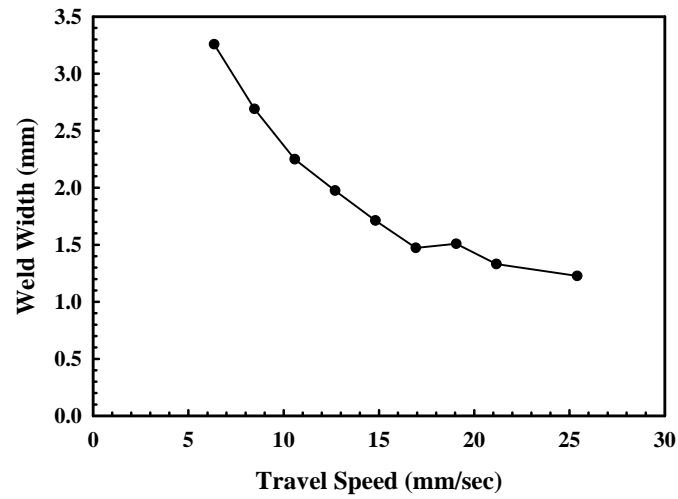


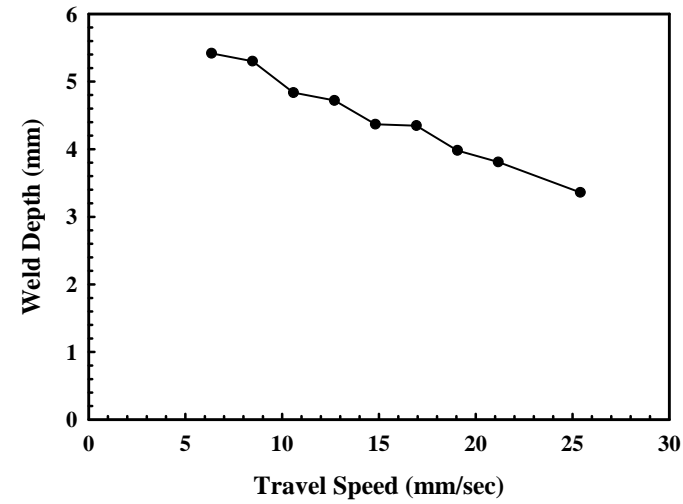
Figure 32(a-d). Micrographs of weld cross sections made on 21-6-9 austenitic stainless steel samples at travel speeds of (a) 21.2 mm/sec, (b) 14.8 mm/sec, (c) 8.5 mm/sec, and (d) 6.4 mm/sec and an input power setting of 1630 W using the LLNL laser system.

Table 11. Summary of weld measurements made on 21-6-9 austenitic stainless steel samples at various travel speeds and an input power of 1630 W using the LLNL laser system.

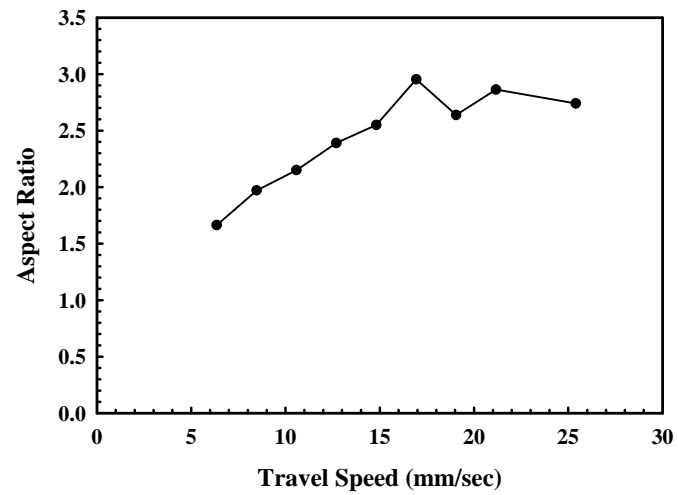
<u>Travel Speed</u> (mm/sec)	<u>Energy</u> <u>Input</u> (J/mm)	<u>Weld</u> <u>Width</u> (mm)	<u>Weld</u> <u>Depth</u> (mm)	<u>Aspect Ratio</u> (Depth/Width)	<u>Keyhole</u> <u>Width</u> (mm)	<u>Weld</u> <u>Reinforcement</u> <u>Height (mm)</u>	<u>Melted</u> <u>Area</u> (mm ²)
25.4 (60 in/min)	64.20	1.226	3.361	2.740	1.100	0.592	4.032
21.2 (50 in/min)	77.0	1.330	3.810	2.864	1.219	0.718	4.662
19.1 (45 in/min)	85.6	1.408	3.982	2.639	1.337	0.650	5.562
16.9 (40 in/min)	96.3	1.472	4.348	2.954	1.445	0.657	5.950
14.8 (35 in/min)	110.0	1.713	4.368	2.551	1.570	0.718	6.659
12.7 (30 in/min)	128.3	1.975	4.720	2.391	1.617	0.561	7.379
10.6 (25 in/min)	154.0	2.250	4.837	2.150	1.787	0.599	8.818
8.5 (20 in/min)	192.5	2.690	5.302	1.971	2.145	0.674	10.405
6.4 (15 in/min)	256.7	3.257	5.419	1.664	2.293	0.603	12.713



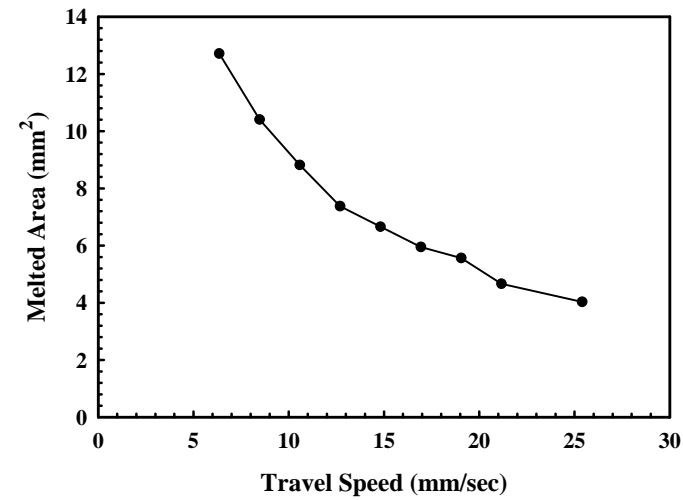
(a)



(b)



(c)



(d)

Figure 33(a-d). Plots showing measurements of the (a) weld width, (b) weld depth, (c) aspect ratio, and (d) melted area in 21-6-9 austenitic stainless steel samples with changes in the travel speed for an input power of 1630 W using the LLNL laser system.

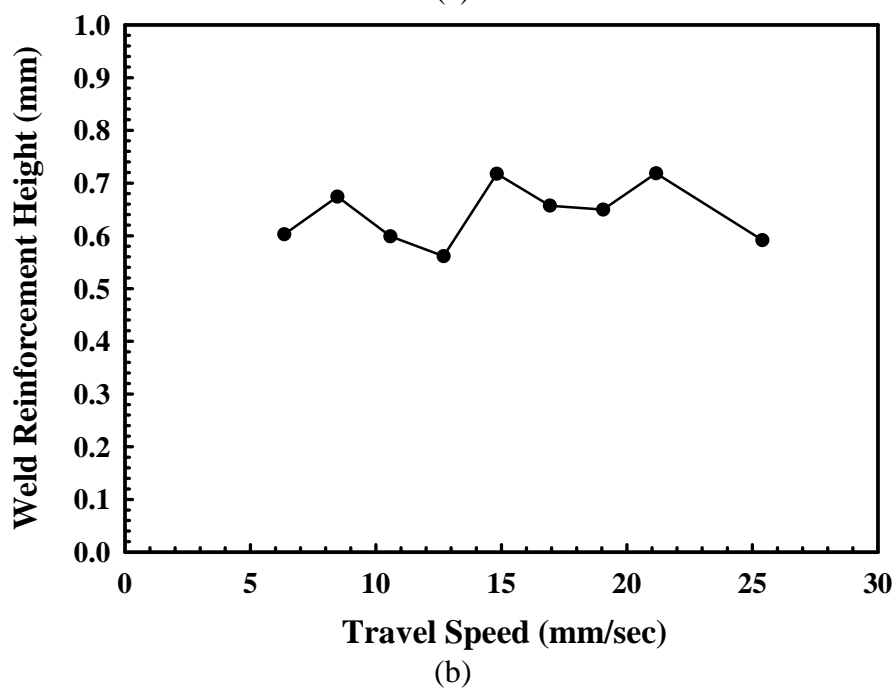
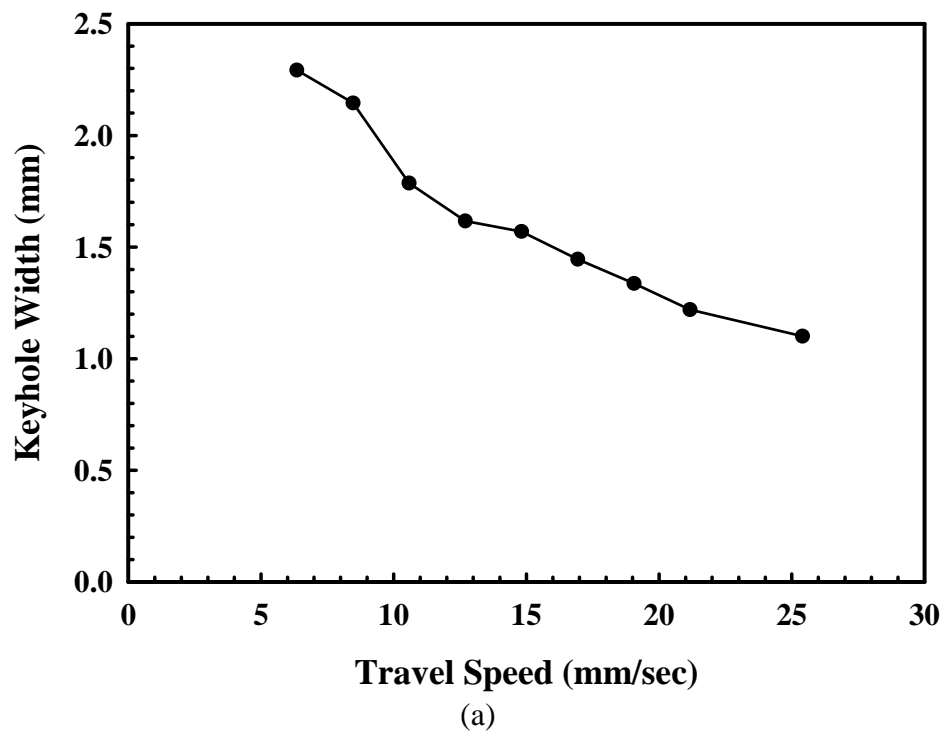


Figure 34(a&b). Plots showing variations in the (a) keyhole width and (b) overfill height measured in 21-6-9 austenitic stainless steel weld samples with changes in travel speed at an input power of 1630 W using the LLNL laser system.

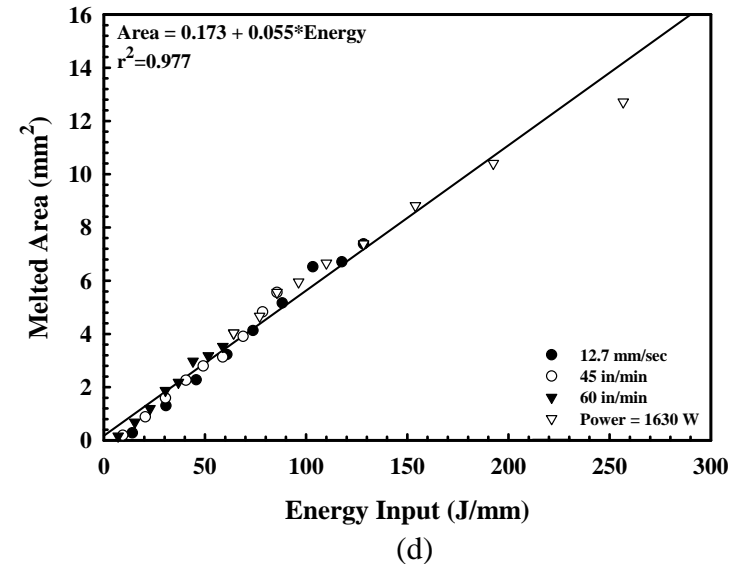
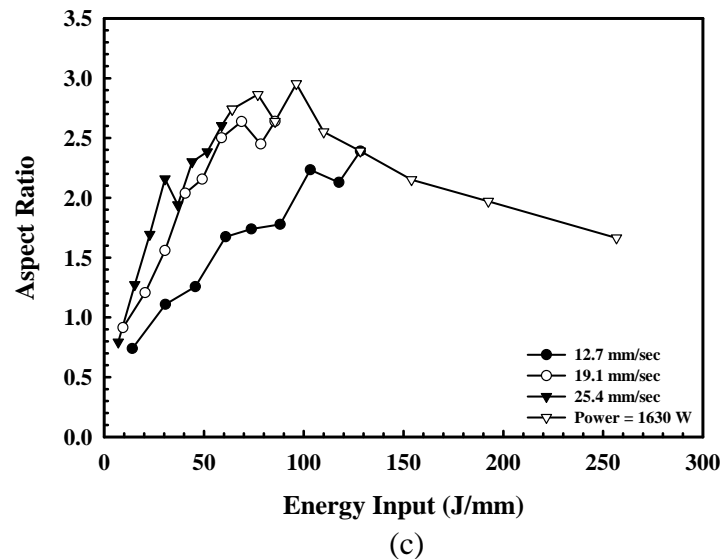
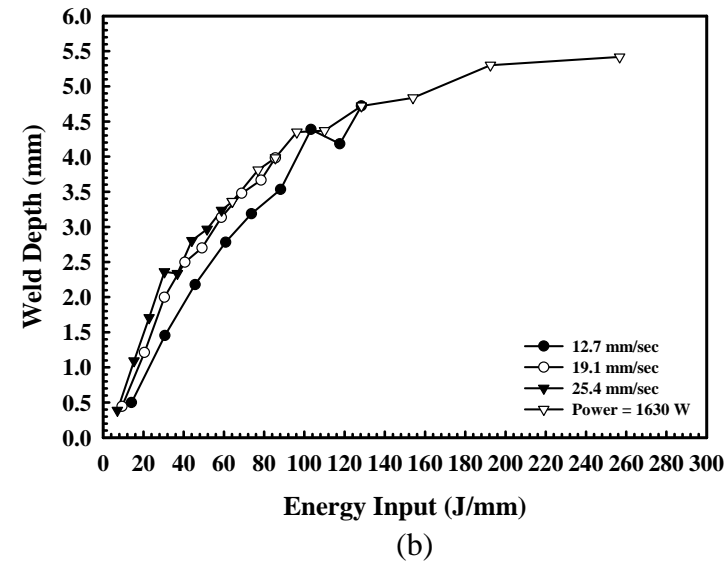
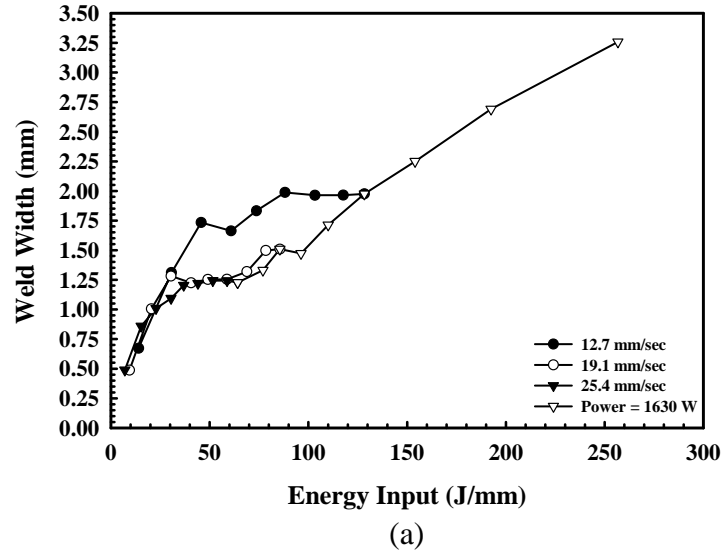


Figure 35(a-d). Plots showing variations in the weld (a) width, (b) depth, (c) aspect ratio, and (d) melted area in 21-6-9 austenitic stainless steel weld samples with changes in the energy input per unit length (J/mm) using the LLNL welding system. Results from the two power variation studies and the travel speed variation study are shown in each plot.

variation and travel speed studies take on similar values and increase at similar rates with increasing energy input, except in a range of energy inputs between approximately 50 J/mm and 100 J/mm. Over this range of energy inputs, the weld widths taken from the power variation study at 12.7 mm/sec are notably higher than those taken from the other studies. In the case of the weld depth, the three power variation studies and the travel speed variation study produce similar trends in weld depth over the entire range of energy inputs, as shown in Figure 35(b). Taken together, the three studies produce a single trend in weld depth, which is defined by a general increase in value with increasing energy input.

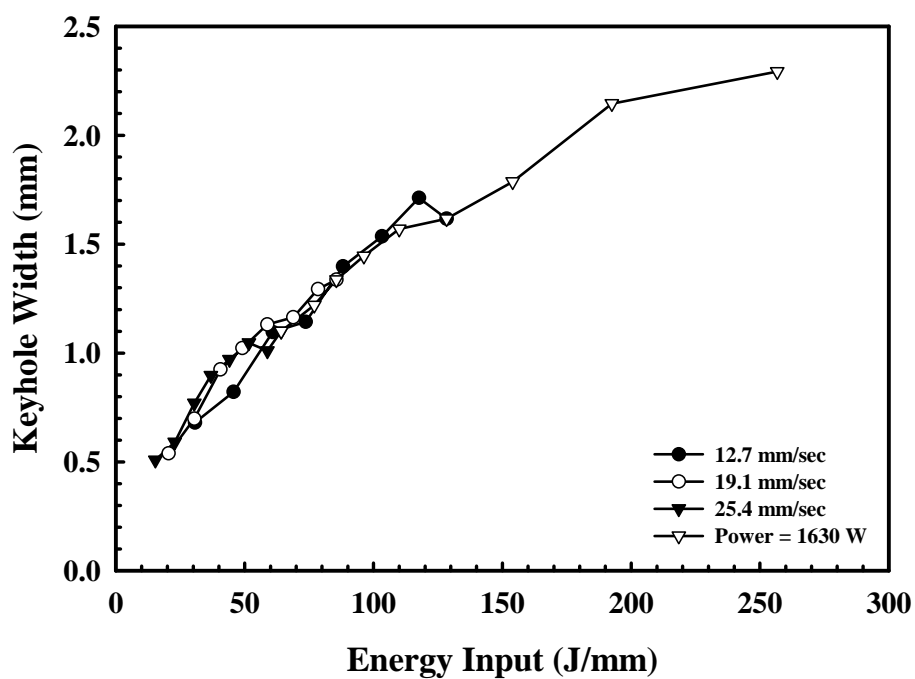
When comparing the weld aspect ratios with the energy input per unit length in Figure 35(c), a different trend from that observed in either the weld width or depth measurements becomes evident. At lower energy inputs, the aspect ratios tend to increase with increasing energy input, reaching peak values at approximately 75 J/mm. There are noticeable differences in the aspect ratios measured in each of the power variation studies, with the aspect ratios measured at a travel speed of 12.7 mm/sec displaying values much lower than those measured at the other travel speeds. As the energy input per unit length is further increased above 100 J/mm, the aspect ratios start decreasing. This decrease results from the weld widths increasing faster than the weld depths at the higher energy input levels.

The comparison between the melted area and the energy input is shown in Figure 35(d). When comparing these more generalized parameters, the four studies, taken together, display a single trend line over the range of energy inputs. A linear regression analysis of the data in Figure 35(d) shows a slope of 0.055, which corresponds with the rate of change of the melted area as a function of the energy input per unit length of weld. Since the melted area is strictly a function of the energy input, the melting efficiency is considered to be the same for the entire range of parameters investigated in this study.

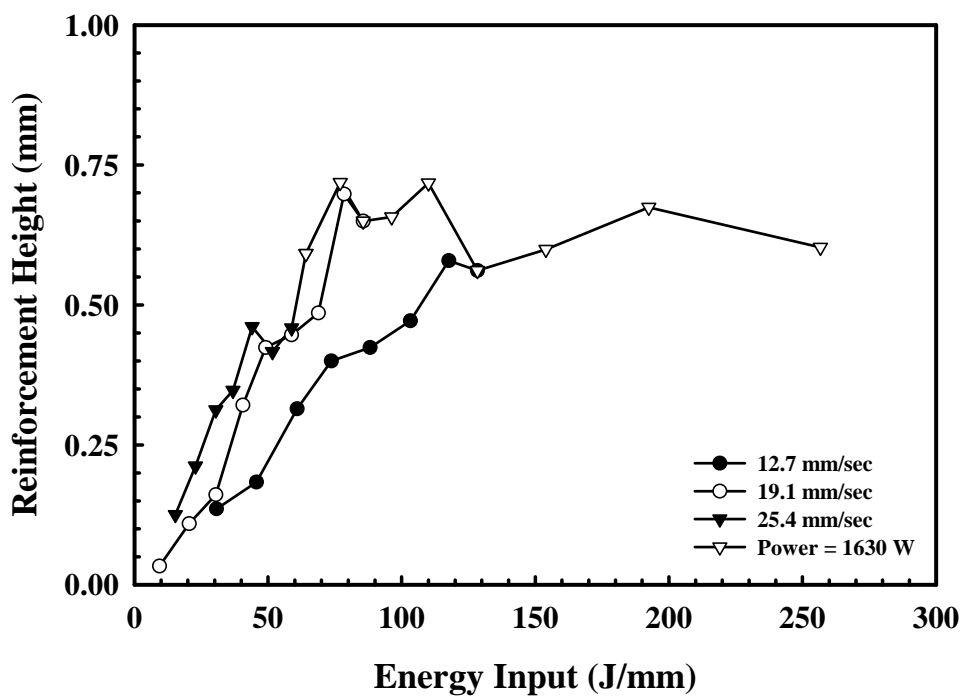
Plots showing the relationships between the keyhole width and the reinforcement height as a function of the energy input per unit length are shown in Figures 36(a&b), respectively. In the case of the keyhole width in Figure 36(a), the results from the four studies display a single trend, in which the keyhole widths increase with increasing energy input. Little to no difference in the keyhole widths measured in the different studies at equivalent energy inputs is observed. On the other hand, rather significant differences are observed in the reinforcement heights measured in each power variation study. The reinforcement height values measured in the power variation study at a travel speed of 12.7 mm/sec are the lowest observed in this energy input range. In general, though, the reinforcement heights increase with increasing energy input up to an energy input value of approximately 100 J/mm. Above this level, the measured reinforcement heights take on a constant value of slightly more than 0.50 mm.

304L Austenitic Stainless Steel vs. 21-6-9 Austenitic Stainless Steel

Since similar studies have been performed on both the 304L and 21-6-9 austenitic stainless steels using the LLNL laser system, a direct comparison can be made between the characteristics of the welds. Even though both materials are austenitic stainless steels, they display markedly different chemistries, especially in terms of their nickel, manganese, and nitrogen concentrations. In particular, the manganese content of the 21-6-9 is over four times higher than that in the 304L stainless steel (9.14 vs. 1.71 wt.%) and the nitrogen content is nearly three times higher (0.23 vs.



(a)



(b)

Figure 36(a&b). Plots showing variations in the (a) keyhole width and (b) overfill height in 21-6-9 austenitic stainless steel weld samples with changes in the energy input per unit length (J/mm). Results for the two power variation studies and the travel speed variation study are shown.

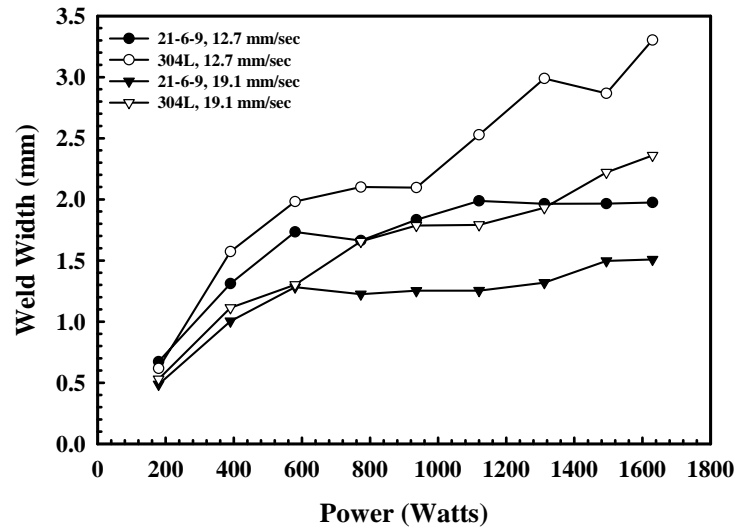
0.082). It can therefore be assumed that any differences in behavior between these two stainless steels are attributable, at least in part, to these differences in chemistry.

Comparisons between the resulting weld pool cross sections of these two materials show both similarities and differences. For example, the weld cross sections from both stainless steels display keyhole mode welding characteristics at machine power settings above 500 W. On the other hand, there is a major difference when it comes to the presence of weld porosity. The 304L stainless steel welds display significant porosity, while the 21-6-9 stainless steel welds display little to none. As noted previously, this lack of porosity results from the enhancement of keyhole stability in this weld, most likely due to the high manganese content in the weld.

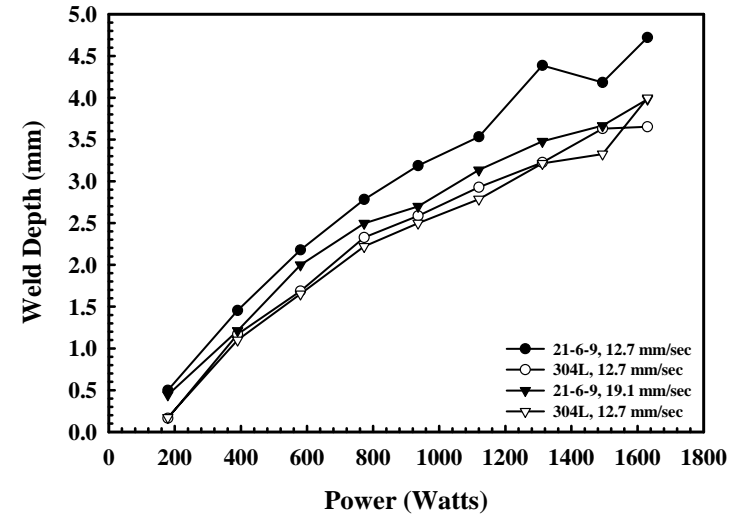
The weld cross section dimensions, including the weld width, depth, aspect ratio, and melted area, are plotted as a function of power input for travel speeds of 12.7 mm/sec and 19.1 mm/sec in Figures 37(a-d) for each stainless steel. In general, the widths of the 304L stainless steel welds display higher values than those achieved by the 21-6-9 welds and increase at higher rates with increasing power than the 21-6-9 welds. At these higher powers, the 21-6-9 welds display nearly constant widths. On the other hand, the 21-6-9 welds display higher depths than the 304L welds across the range of power inputs. In fact, the depths of the 21-6-9 welds made at a travel speed of 19.1 mm/sec exceed those measured in the 304L welds at a travel speed of 12.7 mm/sec. Based on these two sets of measurements, the resulting aspect ratios display significantly higher values for the 21-6-9 welds over the range of power inputs, illustrating the deep and narrow shaped laser welds formed in this material. In addition to the weld width and depth comparisons, the melted areas measured in the two stainless steels are plotted in Figure 37(d) as a function of the power input. In contrast to the results for the weld widths and depths, the melted areas for the two stainless steels are similar when compared at the same power input and travel speed.

Comparisons between the measured keyhole widths and reinforcement heights for these two stainless steels as a function of power variation are shown in Figures 38(a&b), respectively. In general, the keyhole widths of the 21-6-9 welds are larger than those observed in the 304L welds. This difference in keyhole widths is a result of the differences observed in the general weld shape. For example, in the 21-6-9 welds, the side walls of the weld cross sections are rather straight, displaying little difference between the width of the top surface and that in the middle portion of the keyhole. On the other hand, the 304L welds display a more finger-like protrusion of the keyhole from a semi-hemispherical shaped top portion in the weld cross-section. As a result, the keyhole widths in the 304L stainless steel are narrower than the width measured at the top surface of the weld. A comparison of the measured reinforcement heights as a function of power input for these two stainless steels is shown in Figure 38(b). In this case, the 21-6-9 welds display consistently higher reinforcement heights than the 304L stainless steels and little variation between the two travel speeds. On the other hand, the 304L laser welds display a good deal of scatter over the range of power inputs.

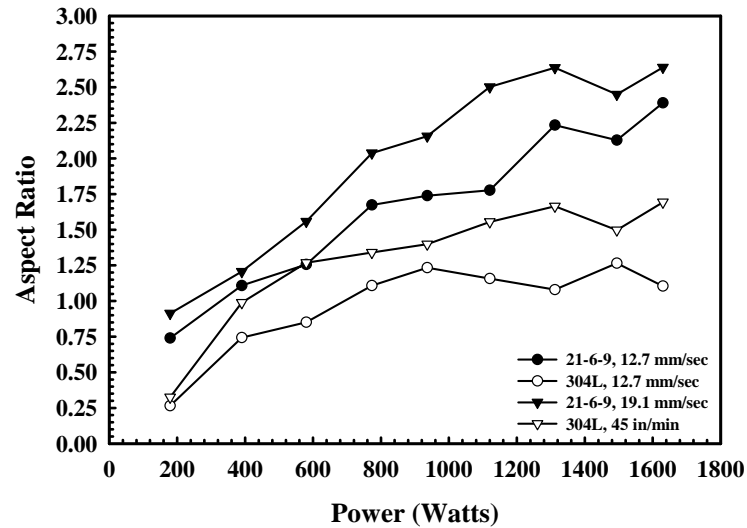
Similar behavior as that observed in the power variation studies also appears when comparing the weld dimensions accompanying variations in travel speed at a constant input power of 1630 W. Figures 39(a-d) display comparisons between measured weld widths, depths, aspect ratios, and melted area for these two stainless steels as a function of travel speed. In general, the same trends observed in Figures 37(a-d) as a function of input power are observed, albeit in an opposite direction. For example, the 304L welds display larger weld widths and smaller depths than the 21-6-9 welds. As a result, the 21-6-9 welds display much higher aspect



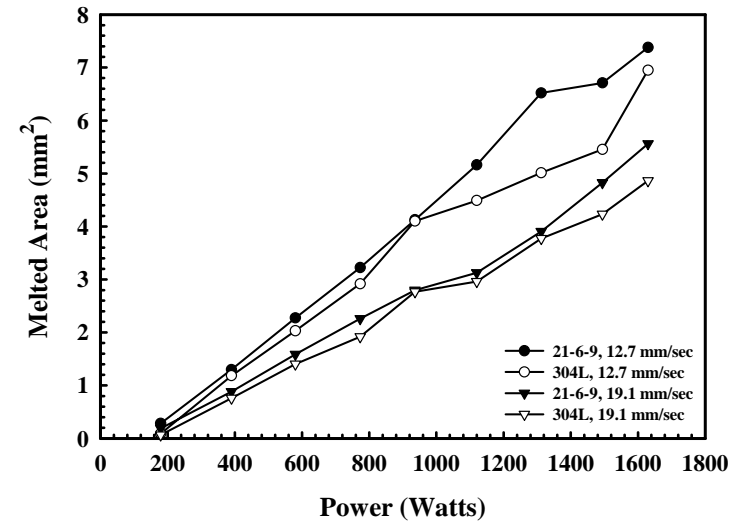
(a)



(b)

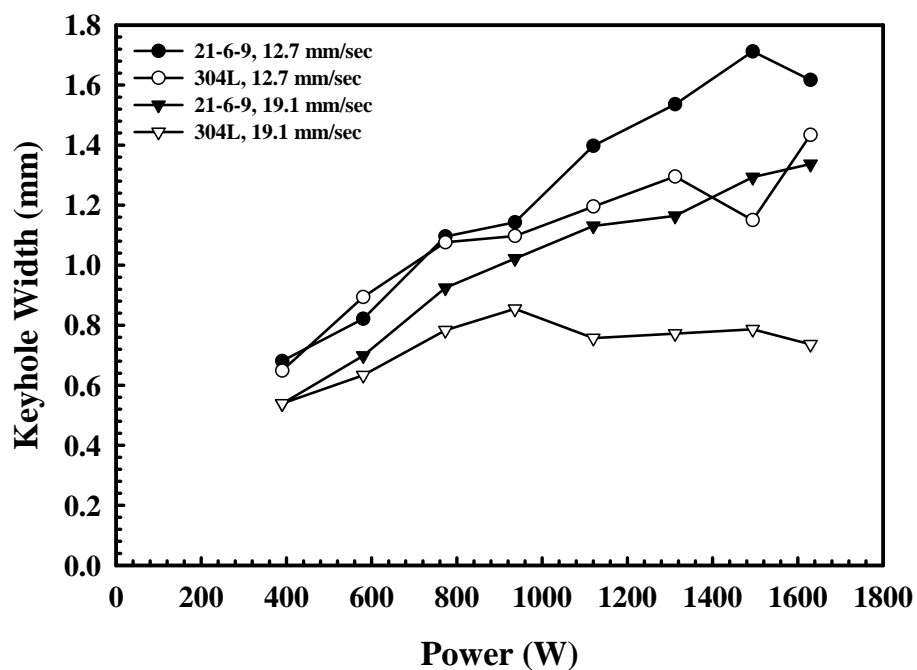


(c)

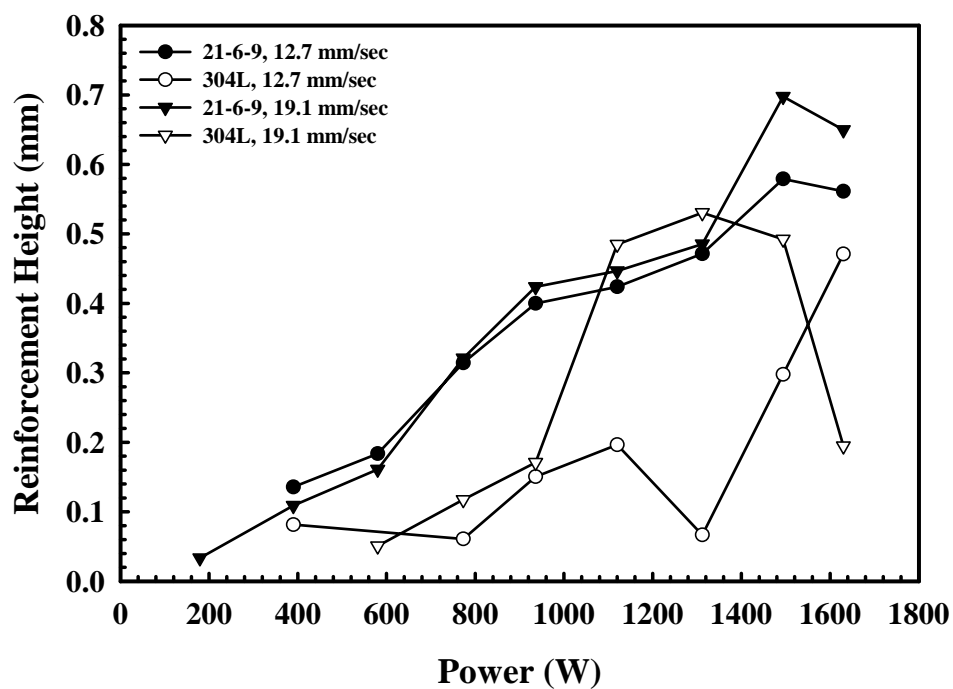


(d)

Figure 37(a-d). Comparison between the measured weld (a) width, (b) depth, (c) aspect ratio, and (d) melted area in both 304L and 21-6-9 austenitic stainless steels with changes in the input power at travel speeds of 12.7 mm/sec and 19.1 mm/sec using the LLNL laser system.

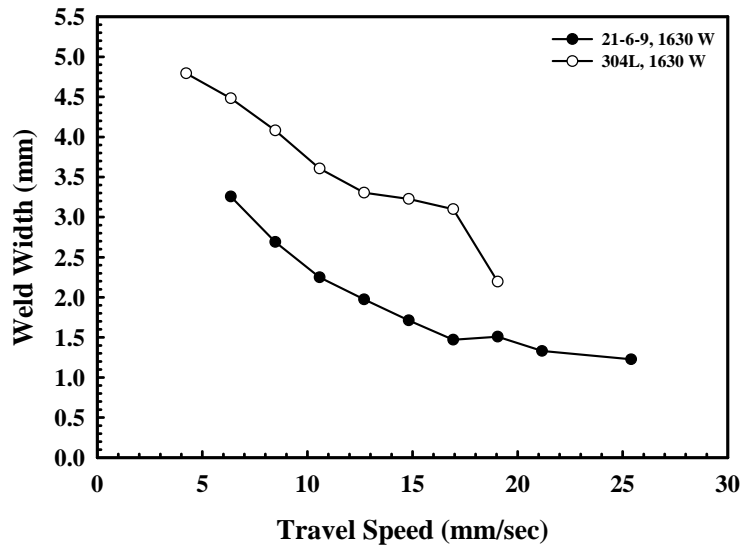


(a)

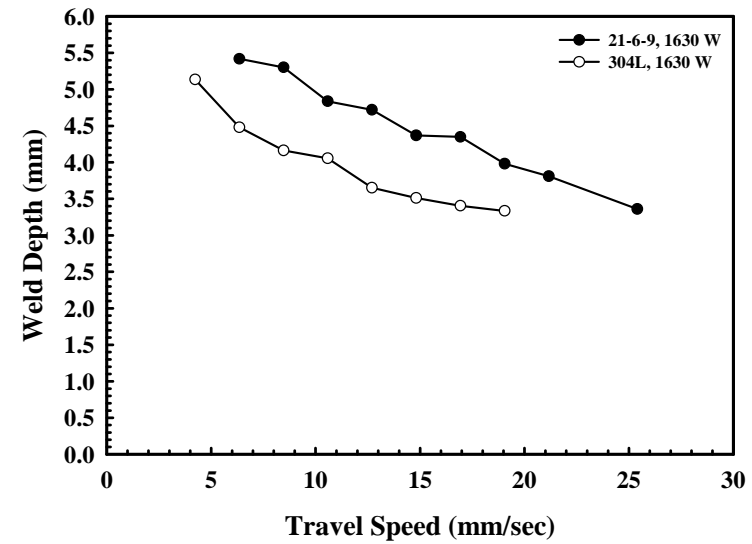


(b)

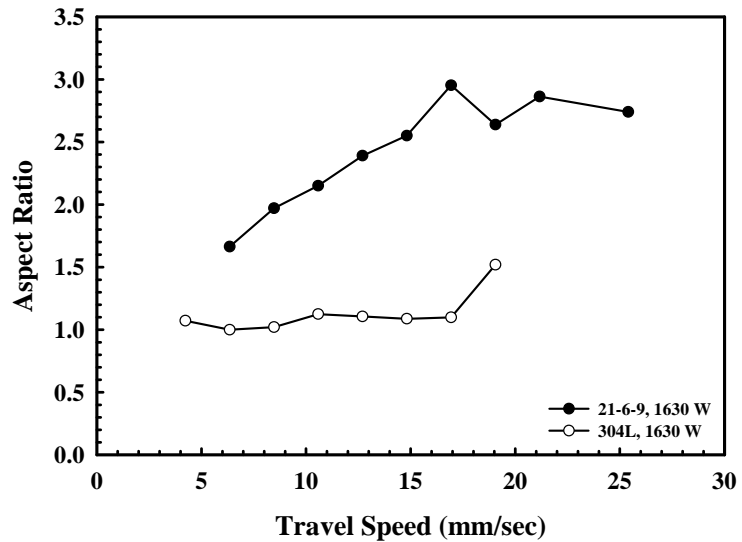
Figure 38(a&b). Plots showing variations in the (a) keyhole width and (b) overfill height in 304L and 21-6-9 austenitic stainless steel samples with changes in the input power at travel speeds of 12.7 mm/sec and 19.1 mm/sec using the LLNL laser system.



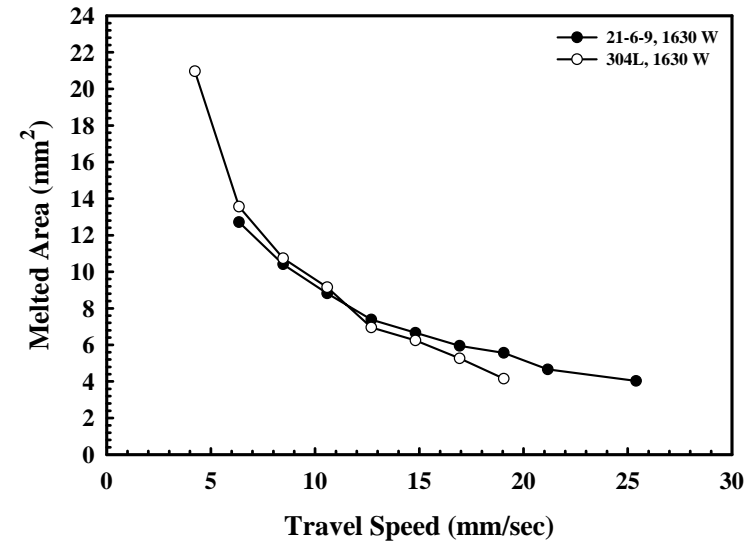
(a)



(b)



(c)



(d)

Figure 39(a-d). Comparison between the measured weld (a) width, (b) depth, (c) aspect ratio, and (d) melted area in 304L and 21-6-9 austenitic stainless steel weld samples with changes in travel speed at a constant input power of 1630 W using the LLNL laser system.

ratios than the 304L laser welds. Once again, though, the melted areas for the two sets of stainless steel welds display little difference in magnitude at each travel speed and similar trends over the range of travel speeds.

Comparisons between the measured weld keyhole widths and the reinforcement heights as a function of travel speed at a constant power input of 1630 W for the 21-6-9 and 304L stainless steel laser welds are shown in Figures 40(a&b), respectively. The measured keyhole widths for the 21-6-9 welds are larger than those measured in the 304L laser welds over a wide range of travel speeds. These higher keyhole widths for the 21-6-9 welds are extensions of the basic weld pool shape, much like that discussed earlier. In the case of the reinforcement heights, shown in Figure 40(b), the values measured on the 21-6-9 welds show similar values across the range of travel speeds and tend to be higher than those for the 304L laser welds.

The above studies of the effects of variations in power and travel speed are combined into plots showing the effects of changes in the energy input per unit length on the primary weld measurements. These plots are shown in Figures 41(a-d). In the weld width and depth plots in Figures 41(a) and 41(b), respectively, the 304L laser welds display larger weld widths, and the 21-6-9 welds display greater weld depths over the range of energy inputs. When converted into the aspect ratio in Figure 41(c), the values for the 21-6-9 welds display higher values than the 304L welds over the range of energy inputs. The aspect ratios for the 21-6-9 welds display a peak value at an energy input per unit length of approximately 75 J/mm. The 304L laser welds also reach a maximum value at nearly the same energy input. As the energy input is further increased, the aspect ratios for the 21-6-9 welds decrease in value, but still remain higher than the 304L laser welds. When the melted areas of the 21-6-9 and 304L laser welds are plotted together as a function of the energy input in Figure 41(d), the differences noted between the two materials in the previous plots disappear. As shown in this plot, the melted areas fall along basically the same linear trend, with only a minimal difference noted in the slopes of the two linear regressions shown (0.056 for 304L vs. 0.055 for the 21-6-9). Based on these various comparisons, it can therefore be determined that in the laser welds made on the 21-6-9 and 304L stainless steels, the same amount of material is melted but the resulting weld shapes are different.

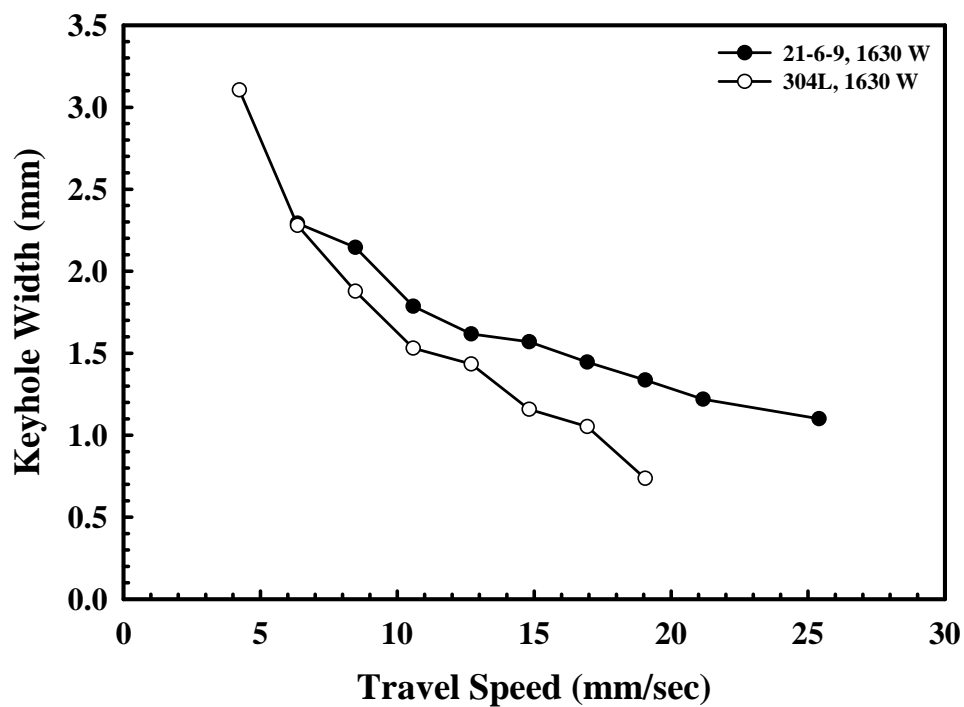
Comparison with Previous Studies

304L Stainless Steel

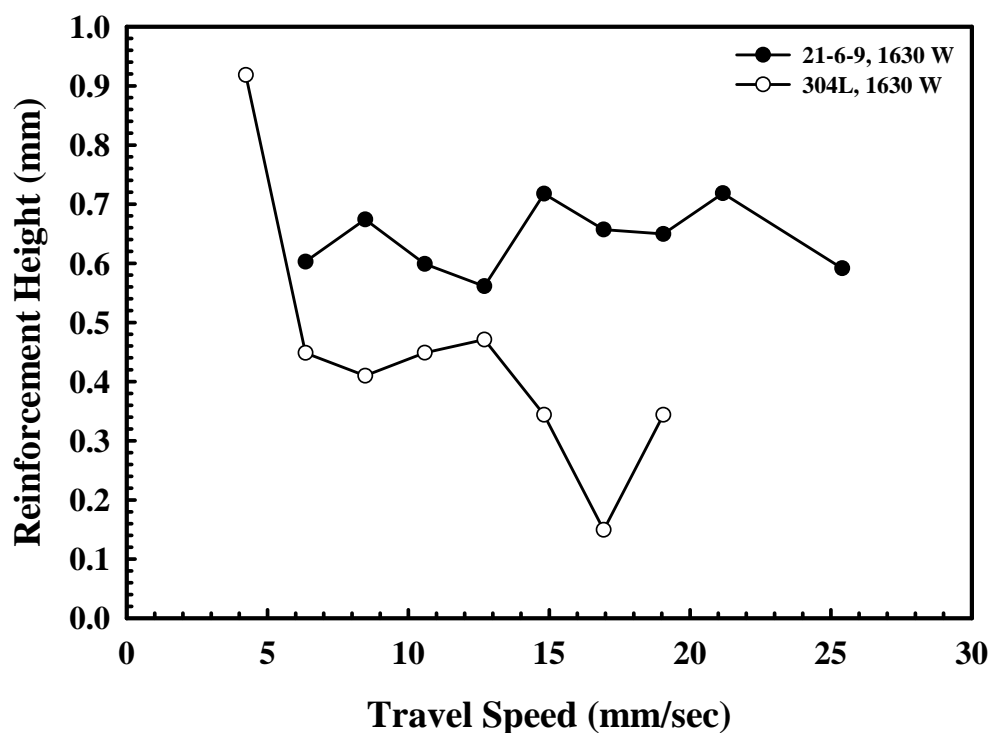
Results from the studies performed on the LLNL laser system with 304L austenitic stainless steel samples are compared with results obtained on comparable laser welding systems at the Rofin Sinar Development Lab⁹ and at Los Alamos National Laboratory (LANL). Of the two systems, the results from the welder at the Rofin Sinar Development Lab provide the closest comparison to those obtained on the LLNL system, since both sets of welds are made on the same material and even used the same optics system. Because of these similarities, the results from the Rofin Sinar welds are primarily discussed below.

Cross sections from several welds made using the Rofin Sinar laser welder are shown in Figures 42(a-d) and 43(a-c). In Figures 42(a-d), cross sections, taken from welds made at machine power settings ranging from 500 W to 2000 W at a travel speed of 19.1 mm/sec, are

⁹ This study was performed as part of the laser workstation procurement acceptance on August 21, 2002 in Detroit Michigan.



(a)



(b)

Figure 40(a&b). Plots showing variations in the (a) keyhole width and (b) overfill height in 304L and 21-6-9 austenitic stainless steel weld samples with changes in travel speed of at a constant input power of 1630 W using the LLNL laser system.

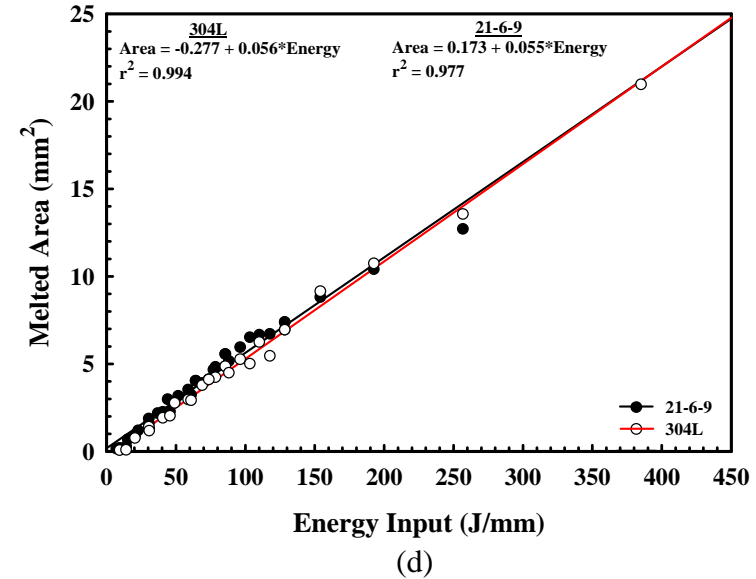
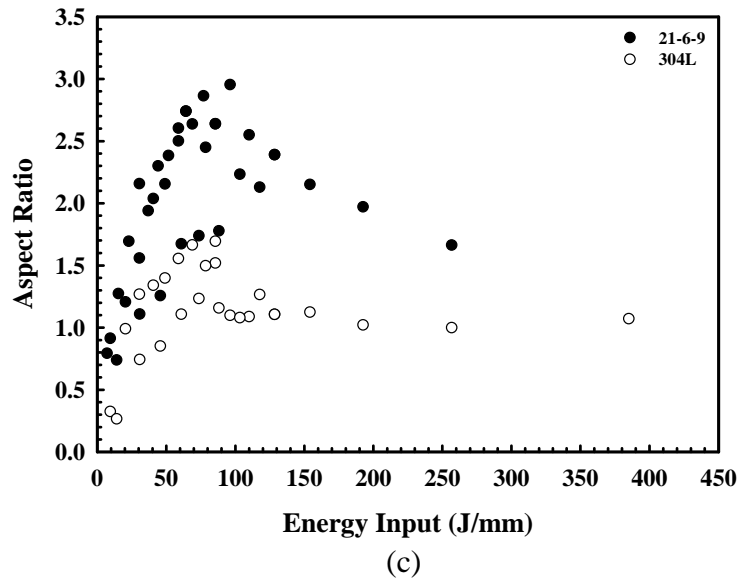
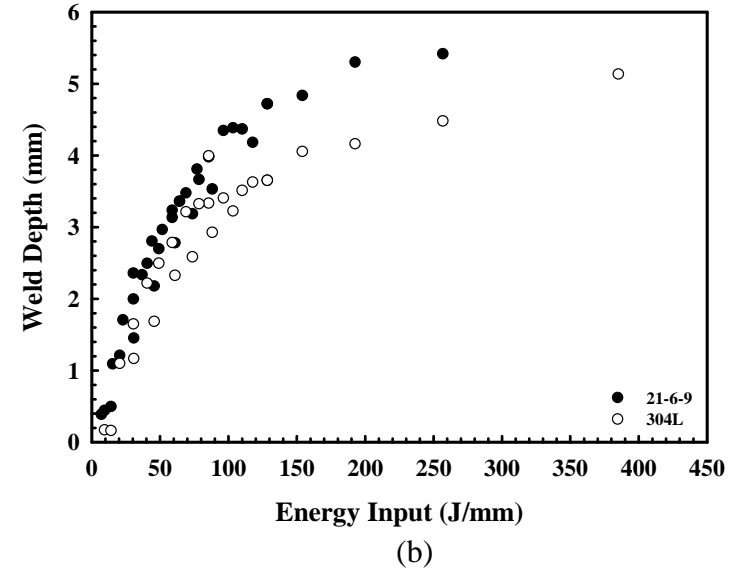
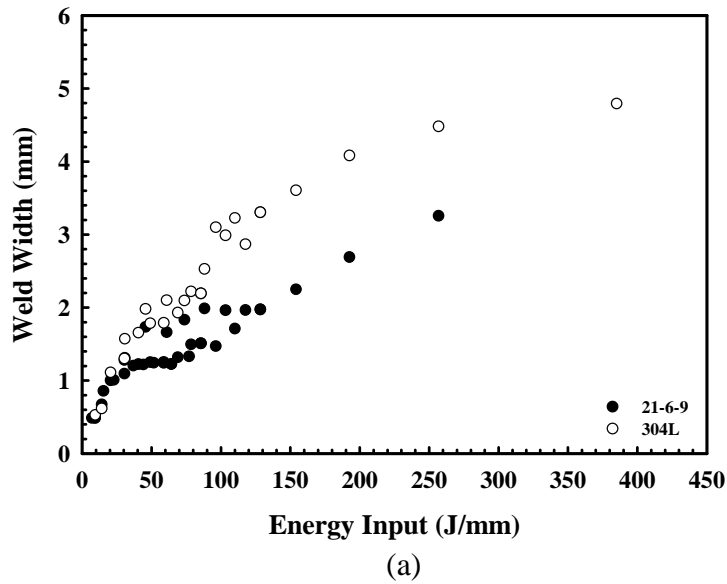


Figure 41(a-d). Comparison between the measured weld (a) width, (b) depth, (c) aspect ratio, and (d) melted area in 304L and 21-6-9 austenitic stainless steel weld samples as a function of energy input per unit length using the LLNL laser system.

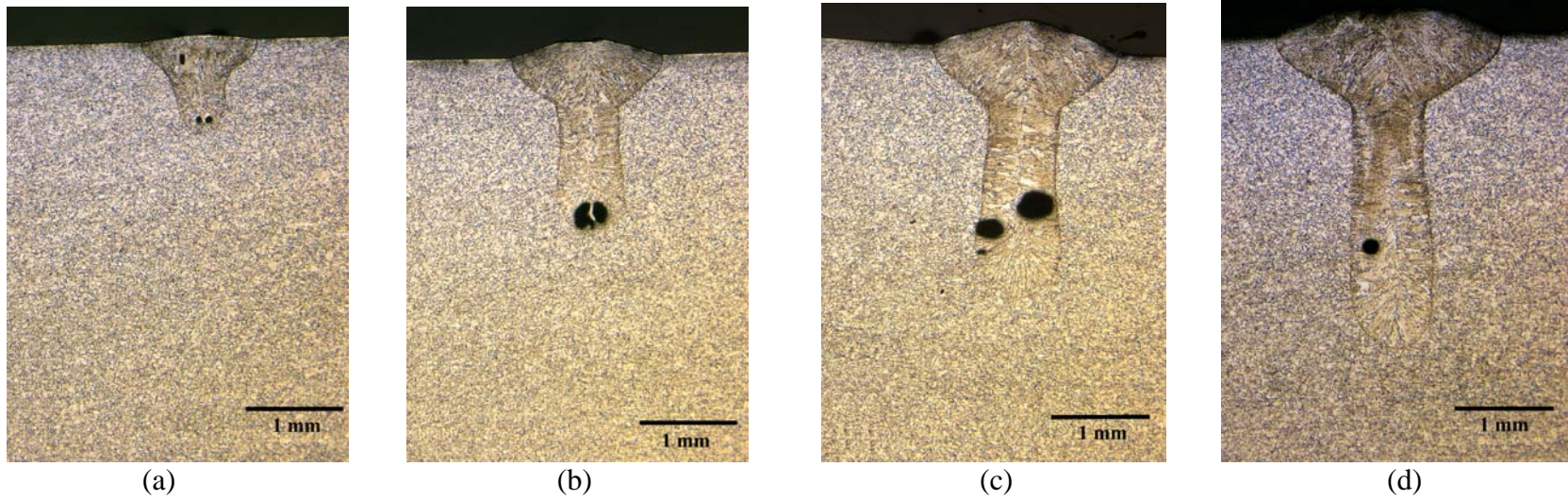


Figure 42(a-d). Micrographs of weld cross sections in 304L stainless steel welds made at machine power settings of (a) 500 W, (b) 1000 W, (c) 1500 W, and (d) 2000 W at a travel speed of 19.1 mm/sec made at the Rofin Sinar Development Labs.

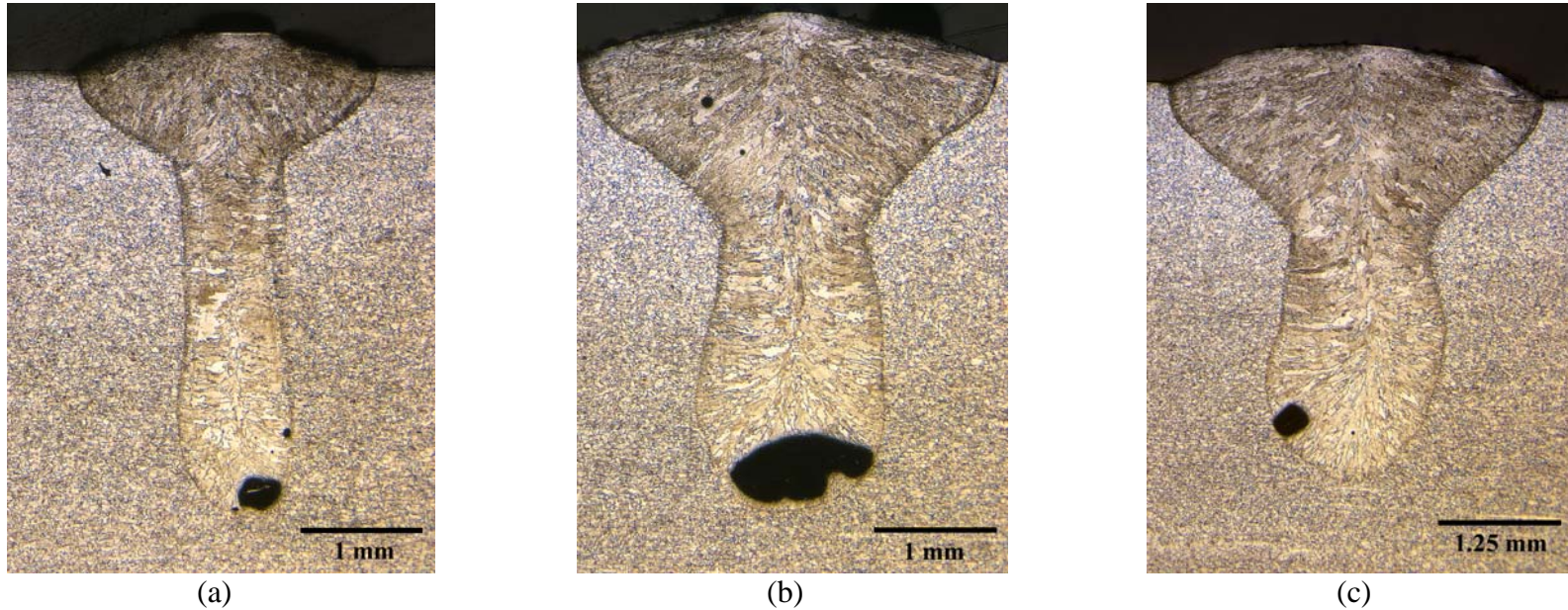


Figure 43(a-d). Micrographs of weld cross sections in 304L stainless steel welds made at travel speeds of (a) 16.9 mm/sec, (b) 10.6 mm/sec, and (c) 8.5 mm/sec at a constant machine power setting of 2200 W made at the Rofin Sinar Development Labs. Note change in magnification of micrograph in (c).

shown. Figures 43(a-c) show weld cross sections taken from welds made at a constant machine power setting of 2200 W and travel speeds ranging from 4.2 to 16.9 mm/sec. The weld cross sections shown in these two figures are produced using nominally the same welding conditions as those used to produce the weld cross sections in Figures 18 and 22, respectively. The two sets of welds are very similar in appearance, with both displaying shapes indicative of a keyhole welding mode and the presence of porosity.

Measurements of several of the important weld dimensions are then made on each weld cross section. Results from welds made at varying machine power setting and a travel speed of 19.1 mm/sec using the laser system at the Rofin Sinar Developmental Lab are listed in Table 12. Corresponding results from the LANL tests are not tabulated here but are plotted along with the LLNL and Rofin Sinar results in Figures 44(a-d) for comparison purposes. In these figures, the measured weld widths, depths, aspect ratios, and melted areas for these three systems are plotted as a function of the machine power setting. Even though different laser power supplies are used, the measured weld widths, depths, and melted areas follow the same general trends and display similar values across the range of machine power settings. A closer examination of the plots shows that the LLNL results typically display a slightly smaller width and a larger depth and melted area than the results from the other systems. As a result, the aspect ratios of the LLNL welds display higher values than the Rofin Sinar and LANL results. Comparisons of the measured keyhole width and reinforcement height for the LLNL and Rofin Sinar welds are shown in Figures 45(a&b), respectively. Overall, these values follow the same general trends for each laser welding system, with both values increasing with increasing machine power setting. Neither set of results shows a consistently higher set of values than the other.

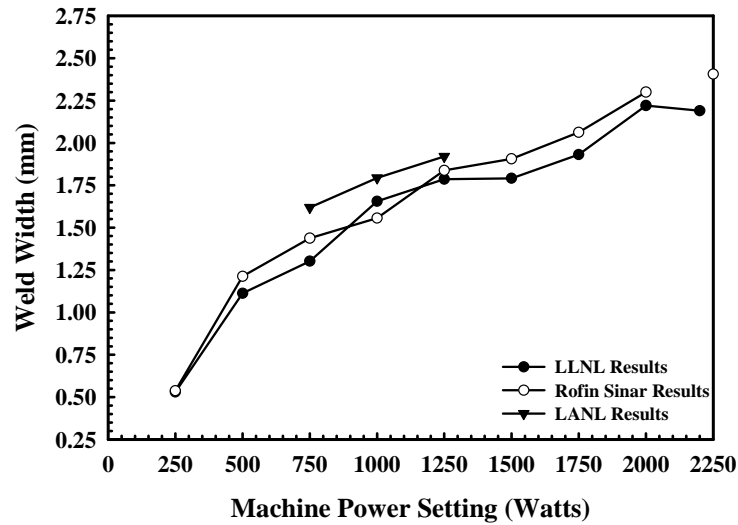
Table 13 lists the results of measurements from welds made at travel speeds between 6.4 and 19.1 mm/sec using the laser welding system at the Rofin Sinar Development Lab. Comparisons between the measured weld widths, depths, aspect ratios, and melted areas, respectively, for the Rofin Sinar and LLNL welding systems are shown in Figures 46(a-d). As in the case of the power variation study, the results from both the Rofin Sinar and the LLNL weld studies display similar trends across the range of travel speeds. In this study, though, the widths, depths, and aspect ratios of the LLNL studies are not consistently more optimal (smaller width, larger depth) than the Rofin Sinar results. Rather, the results show no clear trend in this regard, with the two sets of results being more or less equivalent. The melted areas of the LLNL welds, though, are consistently higher than those for the Rofin Sinar system across the range of travel speeds. Figures 47(a&b) display the comparisons between the keyhole widths and reinforcement heights, respectively. Both sets of results display the expected trends, with an increasing keyhole width and reinforcement height with decreasing travel speed. In the case of the keyhole widths, the LLNL results are consistently higher than the Rofin Sinar results, while neither set of results shows a consistent trend in the case of the reinforcement heights.

21-6-9 Austenitic Stainless Steel

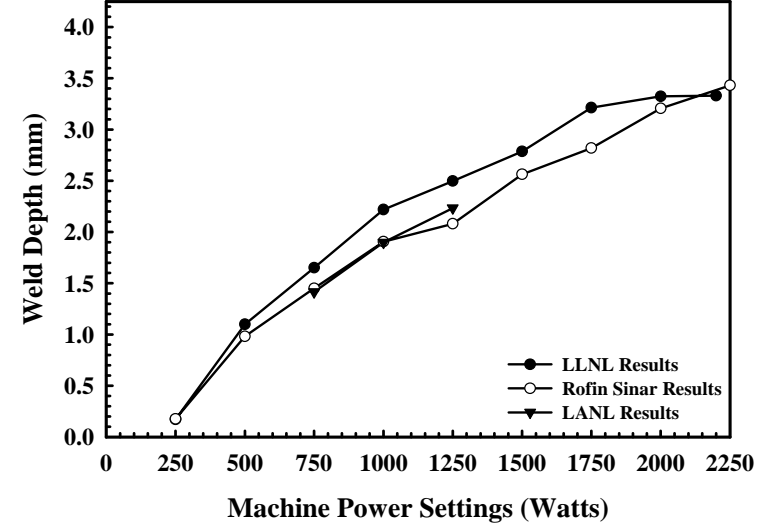
A comparable series of welds on 21-6-9 austenitic stainless steel samples have also been made using the LANL laser system. A summary of these results is given in Table 14. There are some differences in the characteristics of the LLNL and LANL laser systems and the sample geometry. These differences have been addressed in previous sections. Even though the chemistries of the two materials also differ, the differences are rather minor, and both materials

Table 12. Summary of measurements taken on welds made on 304L stainless steel samples with varying machine power settings at a constant travel speed of 19.1 mm/sec using a DY-044 laser welder located at the Rofin Sinar Developmental Lab on the LLNL work station.

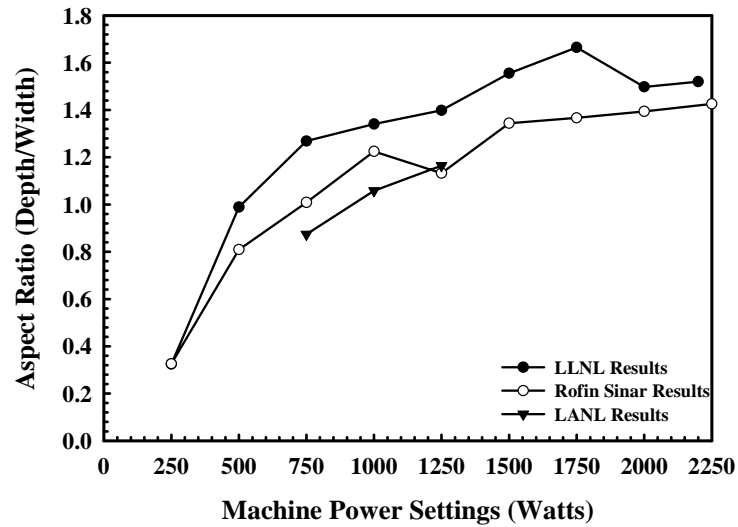
<u>Machine Power Setting (Watts)</u>	<u>Weld Width (mm)</u>	<u>Weld Depth (mm)</u>	<u>Aspect Ratio (Depth/Width)</u>	<u>Keyhole Width (mm)</u>	<u>Weld Reinforcement Height (mm)</u>	<u>Melted Area (mm²)</u>
250	0.54	0.18	0.33	N/A	N/A	0.06
500	1.21	0.98	0.81	0.06	0.50	0.70
750	1.44	1.45	1.01	0.12	0.62	1.26
1000	1.56	1.91	1.22	0.16	0.65	1.75
1250	1.84	2.08	1.13	0.21	0.76	2.14
1500	1.91	2.56	1.34	0.29	0.74	2.80
1750	2.06	2.82	1.37	0.24	0.81	3.24
2000	2.30	3.21	1.39	0.28	0.80	3.70
2200	2.41	3.43	1.43	0.35	0.76	4.15



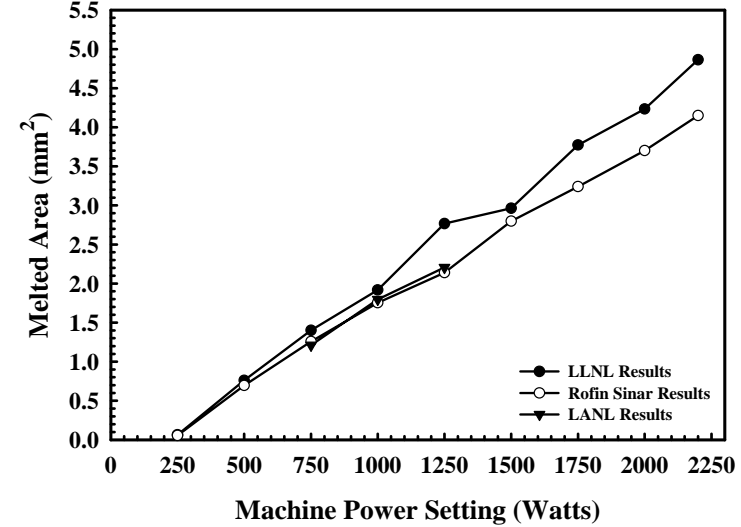
(a)



(b)

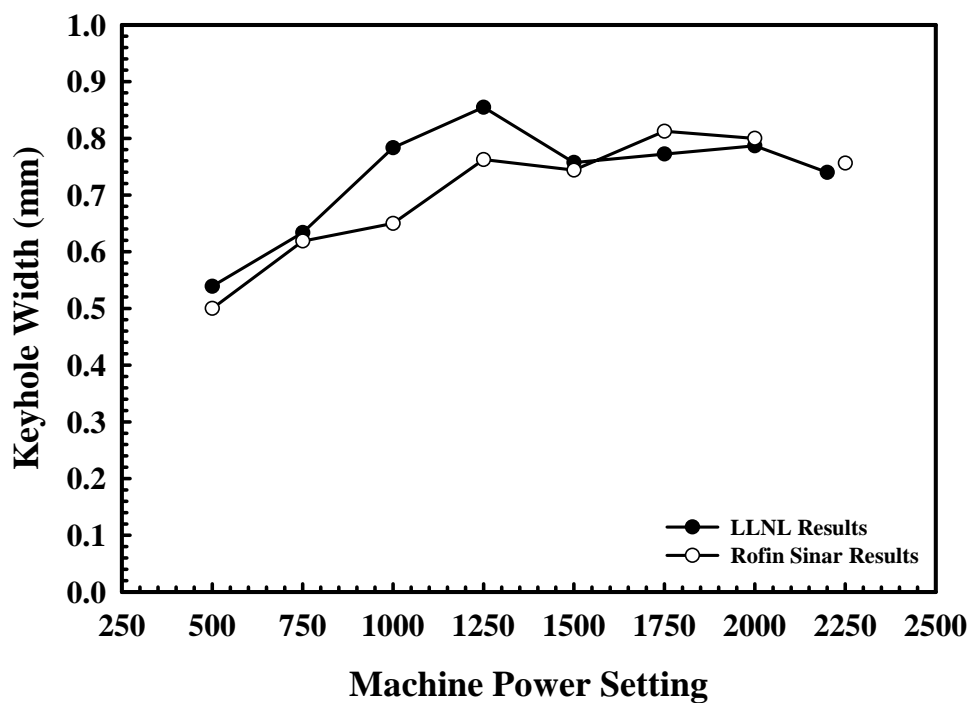


(c)

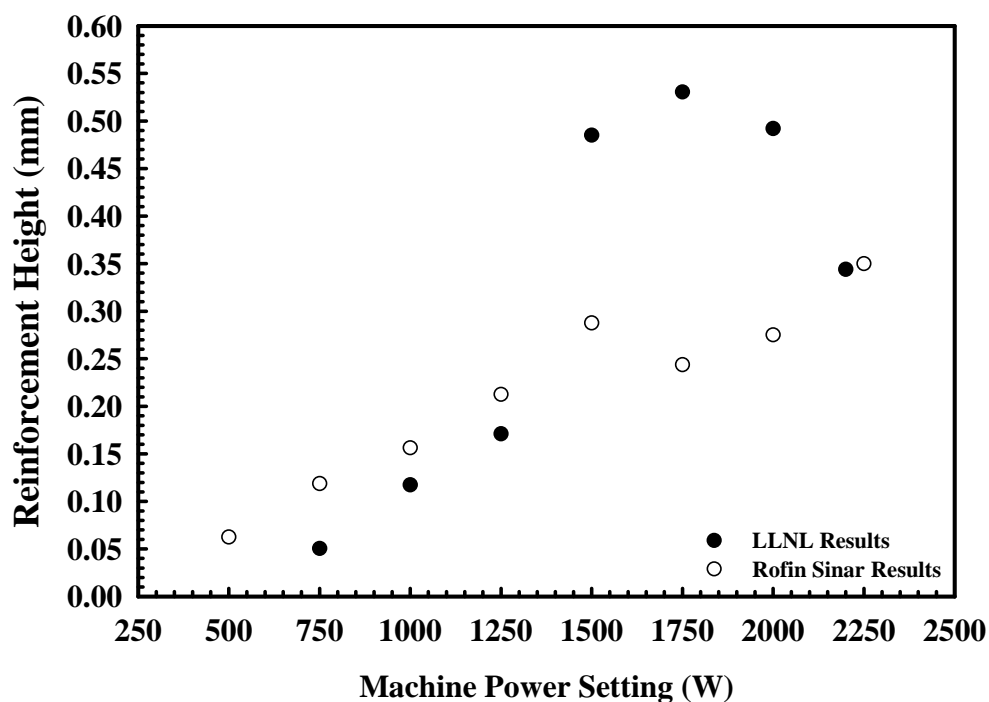


(d)

Figure 44(a-d). Comparison between (a) weld width, (b) depth, (c) aspect ratio, and (d) melted area with changes in weld power at a travel speed of 19.1 mm/sec in 304L stainless steel welds made using the LLNL, Rofin Sinar, and LANL systems.



(a)

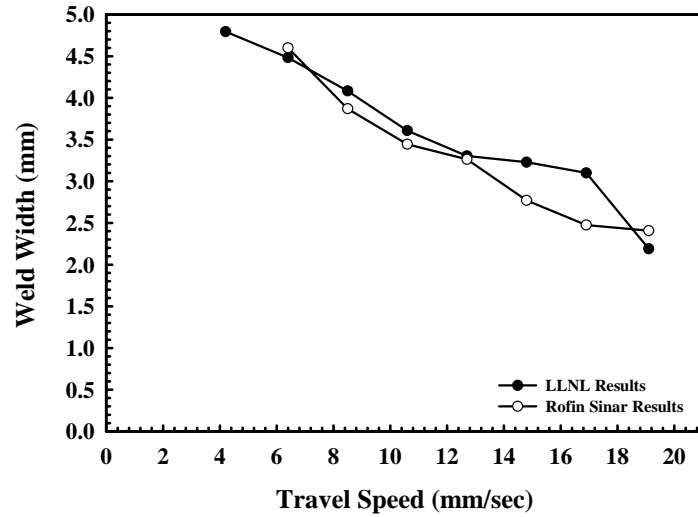


(b)

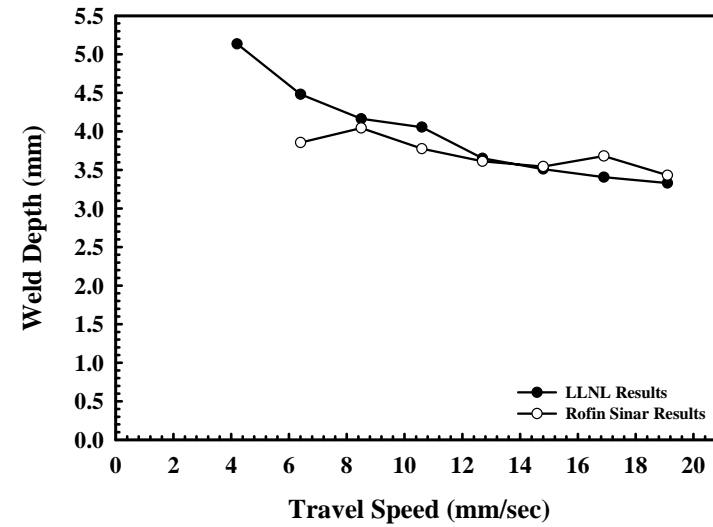
Figure 45(a&b). Plots comparing the (a) keyhole width and (b) overfill height measured on the LLNL and Rofin Sinar laser systems with changes in weld power at a travel speed of 19.1 mm/sec on 304L stainless steel samples.

Table 13. Summary of weld measurements made on 304L stainless steel samples with variations in the weld travel speed using the DY-044 laser welder and LLNL work station at the Rofin Sinar Developmental Lab at a constant machine power setting (2200 W).

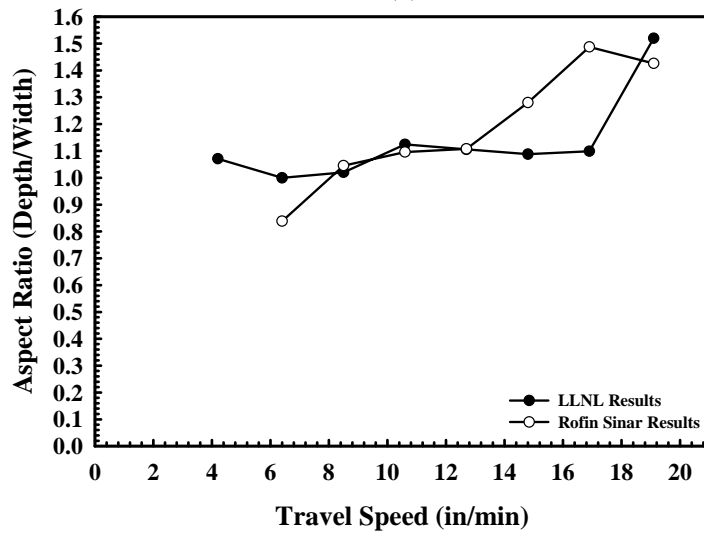
<u>Travel Speed</u> <u>(mm/sec)</u>	<u>Weld</u> <u>Width</u> <u>(mm)</u>	<u>Weld</u> <u>Depth</u> <u>(mm)</u>	<u>Aspect Ratio</u> <u>(Depth/Width)</u>	<u>Keyhole</u> <u>Width</u> <u>(mm)</u>	<u>Weld</u> <u>Reinforcement</u> <u>Height (mm)</u>	<u>Melted</u> <u>Area</u> <u>(mm²)</u>
19.1 (45 in/min)	2.41	3.43	1.43	0.76	0.35	4.15
16.9 (40 in/min)	2.48	3.68	1.49	0.84	0.32	5.58
14.8 (35 in/min)	2.77	3.54	1.28	1.04	0.36	5.16
12.7 (30 in/min)	3.26	3.61	1.11	1.16	0.45	6.42
10.6 (25 in/min)	3.44	3.78	1.10	1.47	0.40	7.57
8.5 (20 in/min)	3.87	4.04	1.05	1.73	0.48	9.69
6.4 (15 in/min)	4.60	3.86	0.84	1.99	0.59	11.62



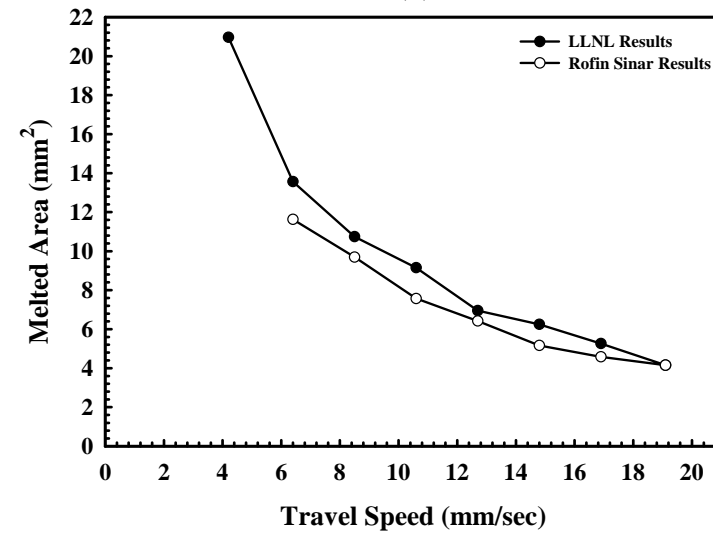
(a)



(b)



(c)



(d)

Figure 46(a-d). Comparison between (a) weld width, (b) depth, (c) aspect ratio, and (d) melted area measured on 304L stainless steel welds with changes in travel speed using the LLNL and Rofin Sinar welders at a constant machine power setting of 2200 W.

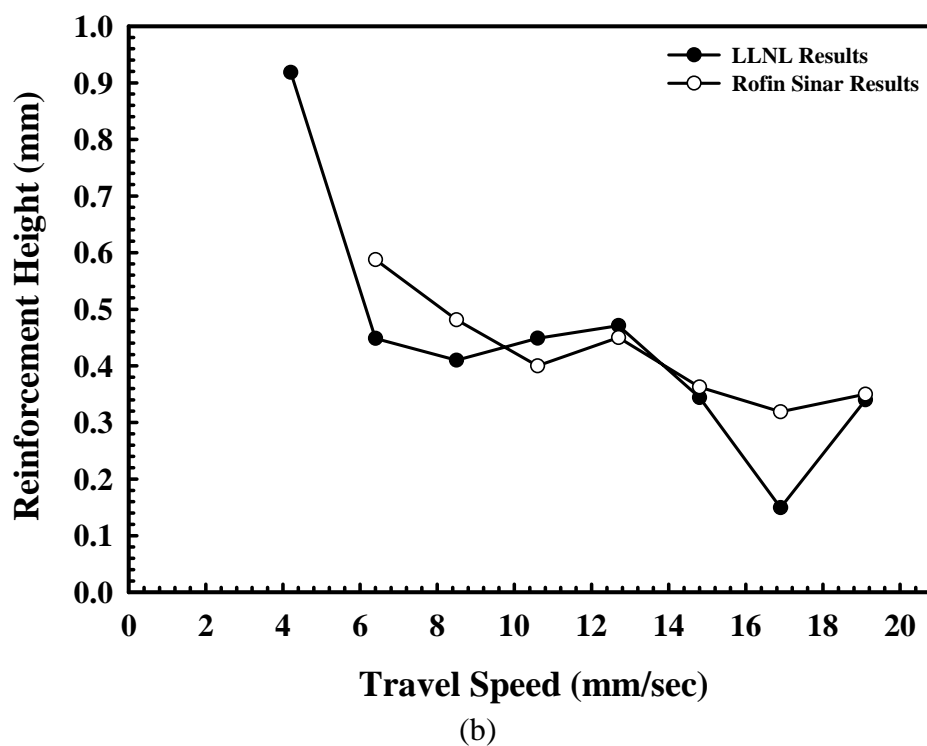
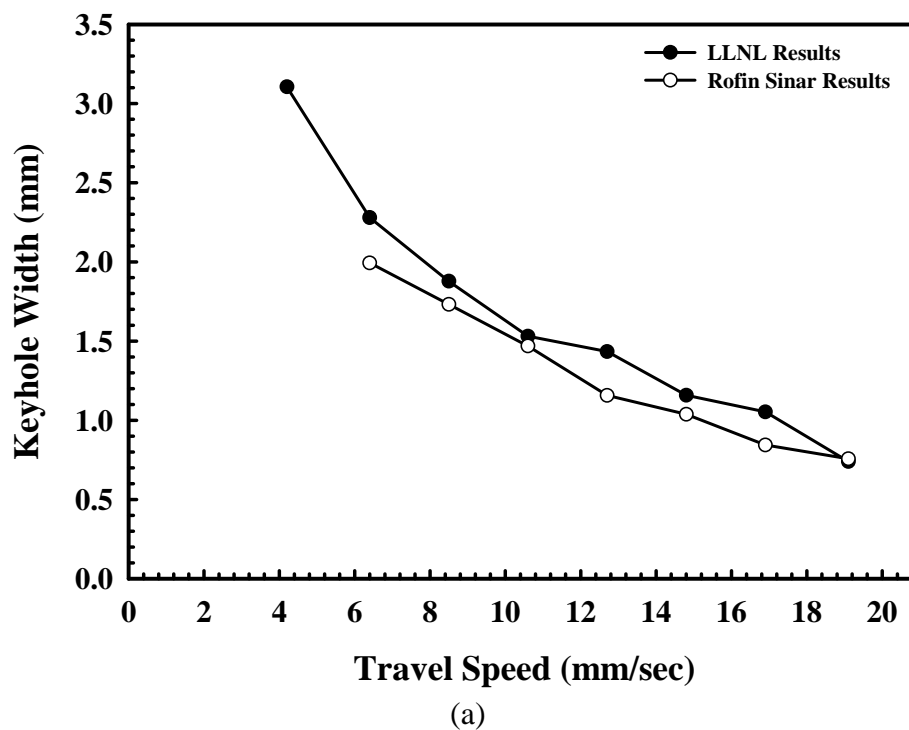


Figure 47(a&b). Plots comparing the (a) keyhole width and (b) overfill height on 304L stainless steel welds made at different travel speeds using the LLNL and Rofin Sinar welders at a constant machine power setting of 2200 W.

Table 14. Summary of measurements made on 21-6-9 austenitic stainless steel weld samples with changes in the input power and shielding gas using the LANL welding system at a travel speed of 19.1 mm/sec.

<u>Machine Power Setting (Watts)</u>	<u>Weld Width (mm)</u>	<u>Weld Depth (mm)</u>	<u>Aspect Ratio (Depth/Width)</u>	<u>Reinforcement Height (mm)</u>	<u>Melted Area (mm²)</u>
<i>Helium Shielding Gas</i>					
250	0.578	0.138	0.239	----	0.057
500	1.210	1.004	0.829	0.029	0.603
750	1.406	1.924	1.368	0.150	1.337
1000	1.484	2.663	1.795	0.210	2.078
1250	1.489	2.933	1.969	0.227	2.653
1500	1.383	2.950	2.133	0.089	2.805
<i>Argon Shielding Gas</i>					
750	1.340	2.001	1.493	0.037	1.355
1000	1.363	2.427	1.781	0.095	2.016
1250	1.455	2.945	2.024	0.069	2.421

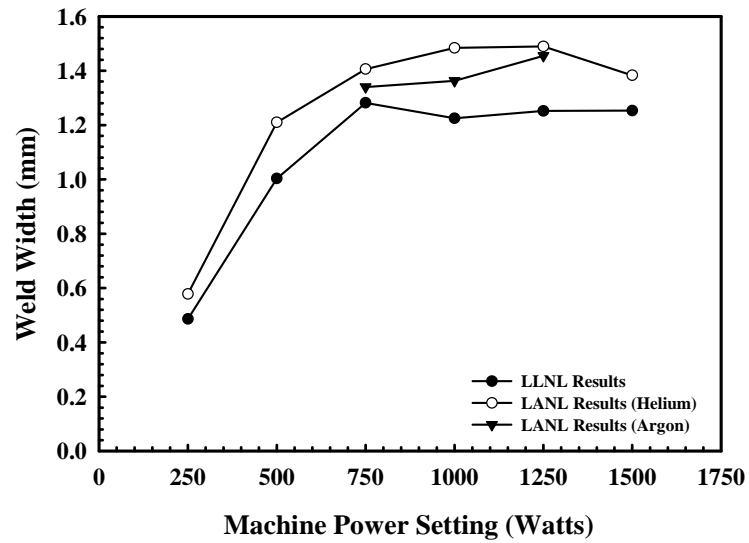
generally fall within the desired composition range for this steel. A comparison between the results from the two systems is therefore useful.

In Figures 48(a-d), results from the power variation study performed on the LLNL laser system at a travel speed of 19.1 mm/sec are compared with similar results from the LANL laser system. Results from the LANL study also include measurements taken on welds made with argon and helium shielding gases and are indicated on each plot. In general, the results from the two laser systems display similar trends, in which the various weld measurements increase with increasing machine power setting. On the other hand, the LLNL results display lower weld widths and higher aspect ratios and melted areas than the LANL results. The measured weld depths for the two systems are very similar, but the LLNL results tend to be slightly higher at most power settings. These results can be correlated with the smaller theoretical beam spot size in the LLNL system (300 μm vs 530 μm).

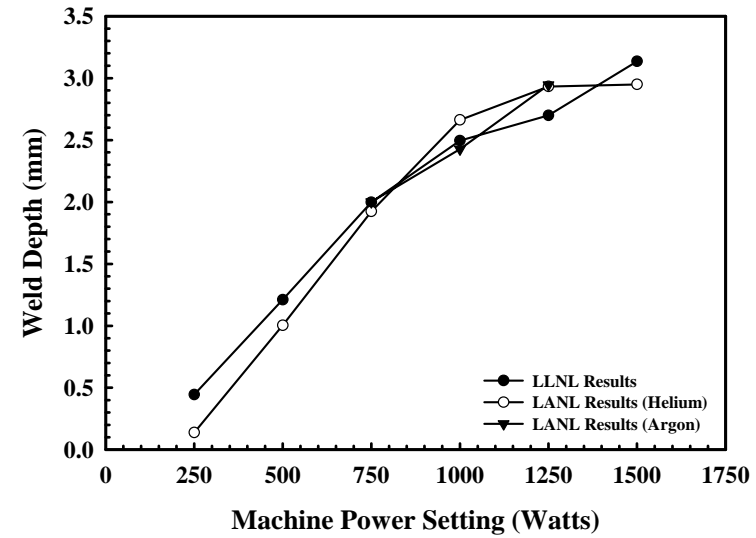
Stainless Steel Welding Overview

A series of welds at various power levels and travel speeds have been made on two grades of austenitic stainless steels using the LLNL welding system. Both grades of stainless steel display a keyhole mode of welding at powers above 500 W for all travel speeds. In general, though, the 21-6-9 welds are narrower, deeper, and exhibit a higher aspect ratio than the 304L laser welds. A maximum depth of slightly more than 5 mm is obtained in 304L stainless steel at the maximum machine power and a travel speed of 4.2 mm/sec. This value is lower than the maximum depth obtained in the 21-6-9 austenitic stainless steel, which displays a depth of more than 5.5 mm with an aspect ratio of 2.7 at the maximum machine power and a travel speed of 6.4 mm/sec. The difference in maximum depths is attributed to the presence of large amounts of manganese in the 21-6-9 stainless steel. The addition of the manganese allows the keyhole formed during welding to remain stable, as demonstrated by the lack of porosity in the 21-6-9 welds, and thus allows deeper and less wide welds to be formed. Even though the aspect ratios of the welds made in the two materials vary significantly, the melted areas for the two welds are nearly identical for equivalent energy inputs.

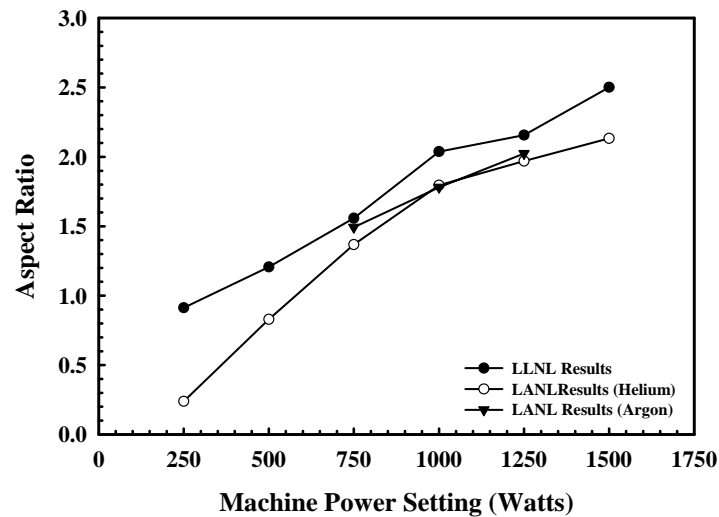
The welds made on the LLNL laser system are also compared to welds made on comparable systems at LANL and the Rofin-Sinar Development Lab. The welds made using each system are comparable in size and shape and display similar trends with changes in the machine power setting and travel speed. Although, welds made using the LLNL system tend to display slightly greater weld depths and melted areas than those made using the other systems with similar welding parameters. In the case of 21-6-9 stainless steel, the results show that the welds made using the LLNL system produce narrower and deeper welds with a higher melted area than those produced using the LANL system.



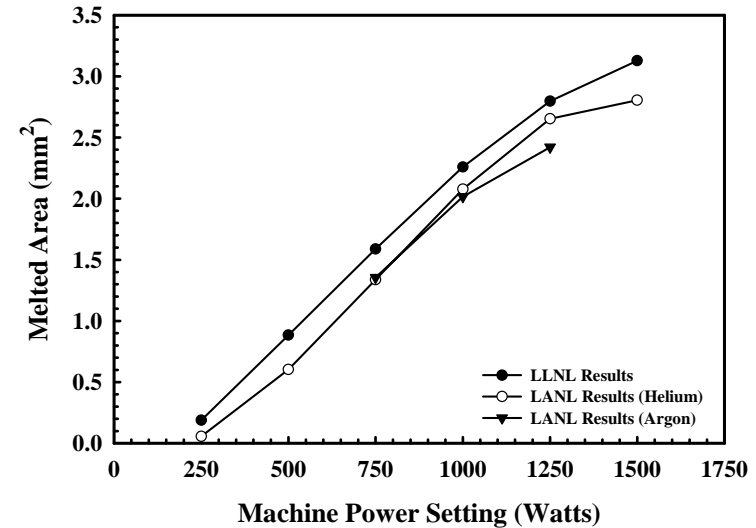
(a)



(b)



(c)



(d)

Figure 48(a-d). Comparison between the measured weld (a) width, (b) depth, (c) aspect ratio, and (d) melted area in 21-6-9 austenitic stainless steel samples with changes in the machine power settings at a travel speed of 19.1 mm/sec using both the LLNL and LANL laser systems.

General Findings and Concluding Remarks

A series of laser welds have been made on refractory metal and stainless steel samples using a Rofin Sinar DY-022 diode pumped CW Nd:YAG laser welder. The effects of variations in the machine power setting at multiple travel speeds on the size and shape of the resulting weld pool cross sections in the various materials have been examined. Measurements of the weld width, depth, melted area, keyhole width, and weld reinforcement height have been made on each weld cross section. Comparisons with results from an equivalent laser system located at Los Alamos National Laboratory for each material have also been made.

Further work is required in order to improve the quality of the laser welds made on these materials using the LLNL laser welding system. This future work will concentrate primarily on removing the unwanted porosity from the keyhole welds in the refractory metals and in the 304L austenitic stainless steel. Such porosity in high power and deep penetration continuous wave laser welds has been linked to the collapse of the unstable keyhole during welding. The complexity involved in the dynamic behavior and stability of the keyhole requires a thorough approach to characterizing the laser welding parameters responsible for the formation of porosity in deep penetration welds.

Future efforts will concentrate first on understanding the stability of the laser plume, which exists above the weld pool surface during laser welding and consists of both ionized shielding gas and evaporated metal from the weld pool. High-speed photography may aid in understanding these laser/plasma interactions and their effects on keyhole stability. Therefore, the stability of the laser plume will be examined using high-speed cameras and thermal imaging in order to monitor the laser plume for instabilities and to attempt to correlate these instabilities with porosity formation in the weld pool. As a result, the interactions between the laser beam, shielding gas, and metal surface, all of which act in concert to form the laser plume, will be better understood, and differences between the laser plumes produced in vanadium and stainless steel laser welds will also be illustrated.

Another area requiring further study involves the absorption of the laser beam by the plasma phase in the laser plume, thus decreasing the laser energy available to weld the material. It therefore becomes necessary to attempt to either remove this laser plume from above the weld pool or to decrease its size. There are several areas that contribute to the size of the laser plume that will receive attention:

- *Shielding gas choices and enhanced plume extraction techniques.*

This work will involve primarily efforts to remove as much of the plasma as possible from above the melt surface. Variations in the shielding gas, primarily investigating the use of helium, will be attempted, as will changes in the direction, flow rate, and nozzle geometry of the shielding gas.

- *Changes in the laser focus condition using advanced laser focus diagnostics.*

The current results show only the effects of the laser focus on the surface of the sample. Changes in the focus position with respect to the sample surface, either below or above, may have a positive or negative impact on the presence of weld porosity.

- *Changes in the offset angle in the laser with respect to the sample surface.*

Currently, the laser head is positioned in a direction normal to the sample surface. Changes in this orientation may also positively or negatively impact the condition of the laser plume and the resulting presence or absence of porosity in the weld pool.

References

- J.Y. Lee, S.H. Ko, D.F. Farson, and C.D. Yoo, "Mechanism of Keyhole Formation and Stability in Stationary Laser Welding," *J. Phys. D: Appl Phys.* **35** (2002) 1570-1576.
- A. Matsunawa, "Problems and Solutions in Deep Penetration Laser Welding," *Science and Technology of Welding and Joining*, **6(6)** (2001) 351-354.
- Document No. 3-03-3.1-001, "Diode-Pumped Continuous Wave NDYAG Laser Welding of Commercially Pure Tantalum"
- T.A. Palmer, J.W. Elmer, R. Pong, and M.D. Gauthier, Document No. 3-03.1-002, "Diode-Pumped Continuous Wave Nd:YAG Laser Welding Of 304L Stainless Steel".
- T.A. Palmer, J.W. Elmer, R. Pong, and M.D. Gauthier, Document No. 3-03.1-003, "Diode-Pumped Continuous Wave Nd:Yag Laser Welding Of Commercially Pure Vanadium"
- T.A. Palmer, J.W. Elmer, R. Pong, and M.D. Gauthier, Document No. 3-03.1-004, "Diode-Pumped Continuous Wave Nd:Yag Laser Welding Of 21-6-9 Austenitic Stainless Steel"
- T. A. Palmer et al. "Characterization of Stainless Steel and Refractory Metal Welds Made Using a Diode-Pumped, Continuous Wave Nd:YAG Laser," Lawrence Livermore National Laboratory, UCRL-ID-146005, 39 pages, November, 2001.
- Smithells Metals Reference Book*, Seventh Edition, ed. by E.A. Brandes and G.B. Brook, (Butterworth Heinemann, Oxford, 1998)